

ARISTOTLE UNIVERSITY OF THESSALONIKI
FACULTY OF ENGINEERING
DEPARTMENT OF MECHANICAL ENGINEERING
LABORATORY OF FLUID MECHANICS AND TURBOMACHINERY

FLIGHT SIMULATION AND DETAILED
AERODYNAMIC STUDIES OF A BLENDED WING
BODY UNMANNED AERIAL VEHICLE

Vasileios Christou

Supervisors:

Prof. Kyros Yakinthos

Dr. Pericles Panagiotou

Diploma Thesis
Thessaloniki, July 2020

ACKNOWLEDGEMENTS

First of all, I would like to sincerely thank my thesis supervisor, Prof. Kyros Yakinthos, the Director of the Laboratory of Fluid Mechanics and Turbomachinery, for providing me with the opportunity to work on such a meaningful project. Moreover, it was him who firstly turned my interest to the direction of fluid mechanics and aerodynamics. His way of teaching the subject was a motivation for me to choose the sector of aeronautics for the last year of my studies, a decision I did not regret making.

Secondly, I would like to thank Prof. Anestis Kalfas, who was always willing to share his knowledge on turbomachines and aviation in general. He would always find the right words to keep his lectures interesting and would always share his various personal experiences on the field.

Furthermore, I feel the need to express my gratitude to my co-supervisor, Dr. Pericles Panagiotou. His never-ending enthusiasm on aeronautics and his great skills in guiding and organizing the whole project, inspired me to work harder on my thesis and studies in general. I would also like to acknowledge Pavlos Kaparos, for his valuable advice whenever an obstacle appeared during my research.

My appreciation also extends to my colleagues of the DELAER research project. More specifically, Thomas Dimopoulos, Dimitrios Mitridis and Thanos Martsopoulos for their assistance throughout the project, and of course my partner in crime and a great friend, Dimitrios Paliaikos, with whom I shared duties on the second part of this thesis. Our cooperation was great and their knowledge on different aspects of the subject fitted perfectly into expanding my own knowledge, in order to achieve my goals.

Last but not least, I would like to thank my family – my parents, Thodoris and Maria, and my sister Mirka – for always supporting my decisions and helping me throughout my university studies and my life in general. Also, I am grateful for the support of all my friends throughout these years and for all the great memories I am taking with me.

Vasileios Christou
Thessaloniki, Greece
July 3, 2020

NOMENCLATURE

AR	Aspect Ratio
AC	Aerodynamic Center, m
b	Wingspan, m
\bar{c}	Wing mean chord, m
c_v	Landing gear's damping constant
CG	Center of Gravity, m
C_D	Drag coefficient
C_m	Pitching moment coefficient
C_L	Lift coefficient
C_I	Roll moment coefficient
C_n	Yaw moment coefficient
C_Y	Side force coefficient
C_{xy}	dC_x/dy
D	Drag, N
F	Force, N
F_μ	Landing gear longitudinal force, N
F_V	Landing gear vertical force, N
F_X	X axis force, N
F_Y	Y axis force, N
F_Z	Z axis force, N
g	Gravitational acceleration, m/s^2
h	Altitude, m
I_{xx}	Moment of inertia on xx plane, kgm^2
I_{xy}	Moment of inertia on xy plane, kgm^2
I_{xz}	Moment of inertia on xz plane, kgm^2
I_{yy}	Moment of inertia on yy plane, kgm^2
I_{yz}	Moment of inertia on yz plane, kgm^2
I_{zx}	Moment of inertia on zx plane, kgm^2
I_{zy}	Moment of inertia on zy plane, kgm^2
I_{zz}	Moment of inertia on zz plane, kgm^2
K	Static margin
k	Turbulence kinetic energy, m^2/s^2
L	Lift, N
L	Rolling moment, Nm
L/D	Lift to Drag ratio
M	Mach number
M	Moment, Nm
M	Pitching moment, Nm
m	Mass, kg

m_f	Fuel mass, kg
m_s	Aircraft solid mass, kg
MAC	Mean Aerodynamic Chord, m
N	Yawing moment, Nm
NP	Neutral Point
P	Power, W
P	Landing gear strut preload, N
p	Pressure, Pa
\dot{p}	Roll rate, rad/s
q	Pitch rate, rad/s
\bar{q}	Dynamic pressure, Pa
R	Total aerodynamic force, N
R	Gas constant, J/molK
Re	Reynolds Number
r	Yaw rate, rad/s
S	Wing planform area, m ²
T	Thrust, N
T	Transformation matrix
T	Temperature, K
u	X axis velocity, m/s
V	Airspeed, m/s
V_g	Ground velocity, m/s
V_w	Wind velocity, m/s
V_{w_s}	Constant part of wind velocity, m/s
V_{w_g}	Stochastic (gusts and turbulence) part of wind velocity, m/s
v	Y axis velocity, m/s
w	Z axis velocity, m/s
X	X body axis force, N
x	X axis
Y	Side force, N
y	Y axis
Z	Z body axis force, N
z	Z axis

Greek Symbols

α	Angle of attack, deg
β	Sideslip angle, deg
γ	Flight path angle, deg
δ_{bp}	Brake pedal deflection
δ_{ee}	Elevon deflection as elevator, deg
δ_{er}	Elevon deflection as aileron, deg

δ_g	Landing gear deflection
δ_l	Deflection in roll axis, deg
δ_m	Deflection in pitch axis, deg
δ_n	Deflection in yaw axis, deg
δ_{re}	Ruddervator deflection as elevator, deg
δ_{rr}	Ruddervator deflection as rudder, deg
δ_s	Strut deflection
δ_t	Tyre deflection
ε_t	Propeller's shaft angle from X axis, deg
η_p	Propeller efficiency
θ	Pitch angle, deg
λ	Latitude, deg
μ	Dynamic viscosity, Ns/m ²
μ	Longitude, deg
μ	Total friction coefficient
μ_B	Braking friction coefficient
μ_{roll}	Rolling friction coefficient
ν	Kinematic viscosity, m ² /s
ρ	Density, kg/m ³
τ	Shear stress, N/m ²
ϕ	Yaw angle, deg
ψ	Roll angle, deg
ω	Angular velocity, rad/s

Subscripts

aero	Aerodynamic
B	Body-fixed reference frame
E	Earth-fixed reference frame
g	Gear
H	Local-horizontal reference frame
LG	Landing Gear
prop	Propulsive
W	Wind-axis reference frame
X	X axis
Y	Y axis
Z	Z axis

ABBREVIATIONS

ATM	Air Traffic Management
AUTH	Aristotle University of Thessaloniki
BWB	Blended Wing Body
CAD	Computer-Aided Design
CFD	Computational Fluid Dynamics
DES	Detached Eddy Simulation
DNS	Direct Numerical Simulation
DoD	United States Department of Defense
EVM	Eddy Viscosity Model
FAA	Federal Aviation Administration
FEM	Finite Element Method
FFS	Full Flight Simulator
GCS	Ground Control Station
ICAO	International Civil Aviation Organization
ISA	International Standard Atmosphere
LDA	Laser Doppler Anemometry
LES	Large Eddy Simulation
LEV	Leading-Edge Vortices
LFMT	Laboratory of Fluid Mechanics and Turbomachinery
MALE	Medium-Altitude Long-Endurance
NASA	National Aeronautics and Space Administration
RANS	Reynolds Averaged Navier-Stokes
RPAS	Remotely Piloted Aircraft System
RPAV	Remotely Piloted Aerial Vehicle
RSM	Reynolds Stress Model
SARC	Spalart Allmaras with Rotation Correction
SST	Shear Stress Transport
UAS	Unmanned Aircraft System
UAV	Unmanned Aerial Vehicle
UCAV	Unmanned Combat Aerial Vehicle

ABSTRACT

The field of unmanned aerial vehicles is an active research area with the potential for development and enhancement in various perspectives. This thesis consists of two parts, which investigate crucial issues, regarding the preliminary design phase of a blended wing body (BWB) medium-altitude long-endurance (MALE) UAV. The first part discusses a method of flight simulation for an Unmanned Aerial Vehicle. A dynamic flight simulation model has been constructed, including take-off, cruise, payload drop and landing, using Matlab and Simulink software. The model's purpose is to get a better understanding on the aircraft's behavior during the different phases of its mission. The simulator operates by solving the airplane's equations of motion. The aerodynamic forces and moments acting on the aircraft are determined using polynomial modeling, where each force and moment coefficient is expressed as a polynomial function, extracted from CFD results. The simulator also calculates forces and moments produced by the engine and the landing gear. Moreover, the model is able to take into account the effect of wind, in case of hazardous weather conditions. In each loop, the simulator takes throttle and control surfaces' deflections as inputs, calculates the state at the next time step, and finally outputs the results to Flightgear, an open source flight simulator software, for a real-time visualization of the aircraft's mission.

The second part of this thesis focuses on the phenomenon of leading-edge vortices, which usually appears on BWB or delta wing-shaped air vehicles. This phenomenon occurs at higher angles of attack and is governed by very complicated flow structures, which lead to non-linear aerodynamic characteristics, such as unstable pitching moment. The unstable pitching moment phenomenon is called 'pitch-break' or 'pitch-up' and is associated with flow separation around the outboard wing region and inboard vortex breakdown, which causes loss of lift, and this loss of lift generates rapidly increasing nose-up moment. A BWB configuration similar to the DELAER RX-3 had already been investigated experimentally at the Aristotle University of Thessaloniki (AUTH). The outputs of this study, concerning the leading-edge and tip vortices were used to evaluate which turbulence model predicts with higher accuracy the vortical structure over the BWB configuration. Four different turbulence models were examined, with the CFD post-processing disclosing that the Transition SST (γ - $Re\theta$) model gives the most accurate results. Hence, this model was used to simulate the vortical flow over the DELAER RX-3, for angles of attack ranging from -4° to 16° , while investigating the LEV phenomenon.

Keywords: UAV, BWB, Flight Simulation Model, Aerodynamics, Leading – Edge Vortices, CFD

ABSTRACT in Greek

Ο τομέας των μη επανδρωμένων αεροχημάτων είναι ένας ενεργός τομέας έρευνας με υψηλές προοπτικές βελτίωσης και ανάπτυξης. Η παρούσα διπλωματική εργασία αποτελείται από δύο μέρη, τα οποία διερευνούν κρίσιμα ζητήματα που αφορούν την προκαταρκτική φάση σχεδιασμού ενός UAV μέσου υψηλέτρου και υψηλής αυτονομίας. Το πρώτο αφορά μια μέθοδο προσομοίωσης πτήσης ενός μη επανδρωμένου αεροχήματος. Αναπτύχθηκε ένα δυναμικό μοντέλο προσομοίωσης πτήσης, το οποίο περιλαμβάνει την απογείωση, την πλεύση, την απελευθέρωση φορτίου και την προσγείωση, χρησιμοποιώντας τα λογισμικά Matlab και Simulink. Ο σκοπός του μοντέλου είναι η καλύτερη κατανόηση της συμπεριφοράς του αεροσκάφους κατά τη διάρκεια των διάφορων φάσεων της αποστολής του. Ο προσομοιωτής λειτουργεί επιλύοντας τις εξισώσεις κίνησης του αεροσκάφους. Οι αεροδυναμικές δυνάμεις και ροπές που δρουν στο αεροσκάφος προσδιορίζονται χρησιμοποιώντας πολυωνυμική μοντελοποίηση, με κάθε συντελεστή δύναμης και ροπής να εκφράζεται ως πολυωνυμική συνάρτηση που εξήχθη από αποτελέσματα CFD. Ο προσομοιωτής υπολογίζει επίσης τις δυνάμεις και τις ροπές που παράγονται από τον κινητήρα και το σύστημα προσγείωσης. Επιπλέον, το μοντέλο μπορεί να λάβει υπόψη την επίδραση του ανέμου, σε περίπτωση επικίνδυνων καιρικών συνθηκών. Σε κάθε βρόχο, ο προσομοιωτής δέχεται ως μεταβλητές εισόδου τις μεταβολές του γκαζιού και των επιφανειών ελέγχου, υπολογίζει τις μεταβλητές κατάστασης του αεροσκάφους στο επόμενο βήμα και τελικά εξάγει τα αποτελέσματα στο Flightgear, ένα λογισμικό προσομοιωτή πτήσης ανοιχτού κώδικα, για οπτικοποίηση της αποστολής του αεροσκάφους σε πραγματικό χρόνο.

Το δεύτερο μέρος επικεντρώνεται στο φαινόμενο των Δινών Ακμής Προσβολής, το οποίο εμφανίζεται συνήθως σε BWB ή δελταπτέρυγα αεροχήματα. Συνήθως αναπτύσσονται σε υψηλές γωνίες προσβολής και προκαλούν πολύ περίπλοκες ροϊκές δομές, οι οποίες οδηγούν σε μη γραμμικά αεροδυναμικά χαρακτηριστικά, όπως η ασταθής ροπή πρόνευσης. Το φαινόμενο αυτό ονομάζεται «pitch-break» ή «pitch-up» και σχετίζεται με την αποκόλληση της ροής στο εξωτερικό τμήμα της πτέρυγας και τη διάσπαση των δινών στο εσωτερικό τμήμα, προκαλώντας απώλεια άντωσης και απότομη αύξηση της ροπής πρόνευσης, η οποία τείνει να στρέψει το ρύγχος του αεροσκάφους προς τα πάνω. Μια BWB διαμόρφωση παρόμοια με αυτή του DELAER RX-3 είχε ήδη διερευνηθεί πειραματικά στο Αριστοτέλειο Πανεπιστήμιο Θεσσαλονίκης (ΑΠΘ). Τα αποτελέσματα αυτής της μελέτης χρησιμοποιήθηκαν για την εύρεση του ακριβέστερου μοντέλου τύρβης όσον αφορά το προαναφερθέν αεροδυναμικό φαινόμενο. Εξετάστηκαν τέσσερα διαφορετικά μοντέλα, ενώ το πιο ακριβές αποδείχθηκε το Transition SST ($\gamma - Re_\theta$). Ως εκ τούτου, αυτό το μοντέλο χρησιμοποιήθηκε για την προσομοίωση της ροής πάνω από το DELAER RX-3, για γωνίες προσβολής από -4° έως 16° .

Λέξεις Κλειδιά: UAV, BWB, Μοντέλο Προσομοίωσης Πτήσης, Αεροδυναμική, Δίνες Ακμής Προσβολής, Υπολογιστική Ρευστοδυναμική

CONTENTS

ACKNOWLEDGEMENTS	I
NOMENCLATURE	III
ABBREVIATIONS	VI
ABSTRACT	VII
ABSTRACT in Greek	VIII
CONTENTS	IX
FIGURES AND TABLES	XII
List of Figures	XII
List of Tables	XVI
The DELAER RX-3 Project	1
INTRODUCTION	3
Overview	3
The DELAER RX-3 Platform	3
Flight Simulator	5
Leading Edge Vortices	7
Objectives	8
Flight Simulator	8
Leading-Edge Vortices	8
THEORETICAL BACKGROUND	9
Coordinate Systems	9
Earth-Fixed Coordinate System	9
Local-Horizontal Coordinate System	9
Body-Fixed Coordinate System	10
Wind-Axis Coordinate System	11
Latitude and Longitude	12
Coordinate System Transformations	13
Aircraft State	18
Stability and Control	19
Mathematical Modeling for Simulation	25

Equations of Motion	25
Aerodynamic Forces and Moments.....	28
Propulsion Forces and Moments.....	32
Landing Gear Forces and Moments.....	33
Atmosphere and Wind Effect	36
Turbulence Theory	41
Turbulence Modeling.....	43
Two-equation eddy viscosity models (EVM).....	44
The k-ϵ model.....	44
The Wilcox k-ω model.....	45
The Baseline (BSL) k-ω model.....	45
The Shear Stress Transport (SST) Model	47
Blending Functions.....	47
The Reynolds Stress Turbulence Model (RSM)	47
The Transition SST Model	48
The Spalart Allmaras Model (SA).....	49
Curvature Correction for the Spalart-Allmaras and Two-Equation Models	50
Leading-Edge Vortices.....	50
TOOLS AND METHODS.....	55
Flight Simulator	55
Flight Model	55
Control Inputs Model.....	57
Aerodynamic Model	58
Flight Dynamics Model	59
Propulsion Model.....	60
Landing Gear Model.....	60
Atmosphere and Wind Model	61
Auxiliary Blocks	62
Flight Visualization	64
Leading-Edge Vortices.....	67

Experimental Results	67
CFD Analysis	70
Mesh and Computational Setup.....	70
Grid Sensitivity Study.....	72
RESULTS.....	79
Flight Simulator.....	79
Cruise.....	79
Take-off	83
Payload Drop.....	85
Landing	88
Wind Effect.....	91
Leading-Edge Vortices.....	95
Comparison of the Experimental and Computational Outputs	95
The DELAER RX-3 geometry	103
LEVs in Flight Simulator	111
CONCLUSIONS	113
REFERENCES	115

FIGURES AND TABLES

List of Figures

Figure I. The DELAER RX-3	1
Figure II. Thesis Flowchart.....	2
Figure 1.1. Rotary Wing (left) [7] and Fixed Wing (right) [8] UAV Configurations	3
Figure 1.2. Basic Layout of the BWB Configuration [15]	4
Figure 1.3. The Antoinette Trainer [18].....	6
Figure 2.1. Earth-Fixed Coordinate System [22]	10
Figure 2.2. Body-Fixed Coordinate System [23].....	11
Figure 2.3. Wind-Axis Coordinate System (v_c : velocity relative to the air mass) [22]	11
Figure 2.4. Sideslip (left) and Angle of Attack (right) [22]	12
Figure 2.5. a) v represented on F_1 and F_2 , b) v in component form in F_1 , c) one component in x_1 and x_2 [22]	14
Figure 2.6. Rotations through θ_z , θ_y and θ_x [22].....	15
Figure 2.7. Aircraft Static Stability Cases [26]	19
Figure 2.8. Pitching Moment versus Angle of Attack Curves [27].....	20
Figure 2.9. $Cn\beta$ for Static Directional Stability [25]	21
Figure 2.10. Aircraft Dynamic Stability Cases [26]	23
Figure 2.11. DELAER RX-3's Control Surfaces.....	24
Figure 2.12. Pressure and shear stress on an airfoil and the Resultant Aerodynamic Force and Moment [12].....	28
Figure 2.13. Aerodynamic Forces on an Airfoil [12].....	29
Figure 2.14. Flow Field inside (right) and outside (left) of the Ground Effect Regime [32]	32
Figure 2.15. Computation of δ_g [28].....	34
Figure 2.16. The Gaussian and a possible non-Gaussian Distribution Function [28]	37
Figure 2.17. Representation of the Wind Turbulence Field [28].....	38
Figure 2.18. The Generation of "Patchy" Atmospheric Turbulence for Real-Time Simulation [28].....	39
Figure 2.19. Superposition of the Wind Profile and Turbulence [28]	41
Figure 2.20. $Cm - \alpha$ and $CL - Cm$ curves for Boeing's BWB-450-1L configuration [52]	51
Figure 2.21. RANS Calculation of the Complex Vortex Topology around a Delta Wing with Sharp (left) and Round (right) Leading Edges [64]	52
Figure 2.22. Vortex Generator (left) [60] and Deployable Serrated Flaps (right) [67]	53
Figure 3.1. Flight Model in Simulink.....	56
Figure 3.2. Trimmed Flight Control Subsystem	57
Figure 3.3. Atmosphere and Wind Model.....	62
Figure 3.4. Flight Instruments and Drop Switch.....	63
Figure 3.5. The DELAER RX-3 in FlightGear	64
Figure 3.6. FlightGear "Cockpit" Display	65

Figure 3.7. The DELAER RX-3 in Blender.....	66
Figure 3.8. Surface Flow Visualization on the 40° Sweep Angle BWB Configuration [20]	67
Figure 3.9. Annotated Smoke Wire/Laser Sheet Visualization over the Center Body at $\alpha = 10^\circ$ ($\Lambda_{c/4} = 40^\circ$) [20]	68
Figure 3.10. Topology of the LDA Measurement Grids [20]	68
Figure 3.11. Line Plots of Time-Averaged Axial (left) and Normal (right) Velocity and Axial Vorticity inside the Vortex, at $X/C = 1$ and Various Angles of Attack [20].....	69
Figure 3.12. Time-Averaged Streamwise (left) and Normal (right) Velocity at $X/C_{\text{root}} = 0.5$ [20]	69
Figure 3.13. Time-Averaged Streamwise (left) and Normal (right) Velocity at the Tip Vortex Plane [20].....	70
Figure 3.14. Yplus on the BWB Configuration	70
Figure 3.15. Computational Domain around the Experimental BWB Configuration (Top View)	71
Figure 3.16. Computational Domain around the Experimental BWB Configuration (Side View).....	71
Figure 3.17. Detail View of the Generated Inflation Layers of the Computational Grid around the DELAER RX-3	72
Figure 3.18. Comparison of the Examined Computation Grids (Nose Region).....	73
Figure 3.19. Computational Domain around the DELAER RX-3 (Top View)	74
Figure 3.20. Computational Domain around the DELAER RX-3 (Side View)	74
Figure 3.21. Lift as a Function of Grid Nodes	76
Figure 3.22. Drag as a Function of Grid Nodes.....	76
Figure 3.23. Pitching Moment (at 1900 mm) as a Function of Grid Nodes.....	77
Figure 3.24. Pitching Moment (at 2008 mm) as a Function of Grid Nodes.....	77
Figure 4.1. Throttle and Elevon Deflection as Elevator for Pre-Drop Cruise.....	79
Figure 4.2. Trim Conditions for Pre-Drop Cruise	80
Figure 4.3. Pitch Angle for Cruise	80
Figure 4.4. Spiral Mode Characteristic Variables	81
Figure 4.5. Roll Angle Doubling Time	81
Figure 4.6. Spiral Descent (graph Y-axis is opposite to the simulation Y-axis).....	82
Figure 4.7. Throttle and Elevon Deflection as Elevator for Post-Drop Cruise	82
Figure 4.8. Trim Conditions for Post-Drop Cruise	83
Figure 4.9. Throttle and Elevon Deflection as Elevator for Take-off, Climb and the Start of Cruise	83
Figure 4.10. The DELAER RX-3 Taking-off.....	84
Figure 4.11. Take-off Characteristic Variables	84
Figure 4.12. Trim Conditions for Climb and the Start of Cruise	85
Figure 4.13. Pitch Angle for Take-off, Climb and the Start of Cruise	85
Figure 4.14. Throttle and Elevon Deflection as Elevator for Payload Drop Case	86

Figure 4.15. Trim Conditions for Payload Drop Case	86
Figure 4.16. Throttle and Elevon Deflection as Elevator Before and After Drop	87
Figure 4.17. Trim Conditions Before and After Drop	88
Figure 4.18. Throttle, Elevon Deflection and Brake Pedal Deflection for Descent and Landing	88
Figure 4.19. Position, Velocity and Angle of Attack for Descent and Landing	89
Figure 4.20. Figure 4.19 from Touchdown to Immobilization.....	89
Figure 4.21. Ground Effect	90
Figure 4.22. The DELAER RX-3 Approaching the Landing Runway.....	90
Figure 4.23. Spiral Descent due to Side Wind Gust (graph Y-axis is opposite to the simulation Y-axis).....	91
Figure 4.24. The Effect of Wind on Cruise.....	92
Figure 4.25. The Effect of Wind on Aircraft Orientation	92
Figure 4.26. The Effect of Wind on Aircraft Body Velocity Components	93
Figure 4.27. The Effect of a Headwind Gust.....	94
Figure 4.28. The Effect of a Tailwind Gust.....	94
Figure 4.29. Line Plot of Streamwise Velocity Component at the Tip Vortex Plane	95
Figure 4.30. Line Plot of the Normal Velocity Component at the Tip Vortex Plane.....	96
Figure 4.31. Line Plot of the Axial Vorticity Component at the Tip Vortex Plane	96
Figure 4.32. Comparison between the Contour Plots of the Streamwise Velocity Component at the Tip Vortex Plane	98
Figure 4.33. Comparison between the Contour Plots of the Normal Velocity Component at the Tip Vortex Plane	99
Figure 4.34. Comparison between the Contour Plots of the Streamwise Velocity Component at the LEV Plane	100
Figure 4.35. Comparison between the Contour Plots of the Normal Velocity Component at the LEV Plane	101
Figure 4.36. Surface Flow Visualization Comparison	102
Figure 4.37. Lift Coefficient as a Function of Angle of Attack	103
Figure 4.38. Drag Coefficient as a Function of Angle of Attack	103
Figure 4.39. Pitching Moment Coefficient as a Function of Angle of Attack	104
Figure 4.40. Drag Polar.....	104
Figure 4.41. Lift Coefficient as a Function of Pitching Moment Coefficient	105
Figure 4.42. Axial Vorticity at various x/c Planes	105
Figure 4.43. Dual vortex structure (Detailed view)	106
Figure 4.44. Streamlines over the Aircraft, colored by Turbulence Intensity	107
Figure 4.45. Surface Flow Visualization along with Pressure Coefficient	108
Figure 4.46. Contour Plots of the Vorticity Distribution at $y/s = 0.3$ (Kink Region)	109
Figure 4.47. Contour Plots of the Pressure Distribution at $y/s = 0.3$ (Kink Region)	109

Figure 4.48. Contour Plots of the Streamwise Velocity Component (u/U_{∞}) at $x/C_{root} = 0.5$	110
Figure 4.49. Contour Plots of the Normal Velocity Component (w/U_{∞}) at $x/C_{root} = 0.5$	111
Figure 4.50. Take-off and Climb using the γ - $Re\theta$ Curves.....	112
Figure 4.51. Aircraft Stall.....	112

List of Tables

Table 2.1. Coordinate Systems Definition	13
Table 2.2. Frequent Transformation Angles.....	17
Table 2.3. Aircraft State Vector	18
Table 3.1. Grid Statistics at $\alpha = 8^\circ$	72
Table 3.2. Forces and Moments at $\alpha = 8^\circ$	75
Table 3.3. Absolute Relative Errors at $\alpha = 8^\circ$	75
Table 4.1. Pre-Drop Cruise Trim Conditions.....	79
Table 4.2. Post-Drop Cruise Trim Conditions	82
Table 4.3. Aircraft Changes due to Payload Drop	87
Table 4.4. Pre-Drop and Post-Drop Trim Conditions.....	87
Table 4.5. Wind Characteristics.....	91
Table 4.6. Wind Characteristics.....	93
Table 4.7. Percentage Errors of the Velocity Components Compared to the Experimental Results	97

The DELAER RX-3 Project

This thesis contributes with its results to some crucial aspects of the DELAER research project, which is co-financed by the European Union and Greek national funds [1]. The main goal of the DELAER research project is the design, development, manufacture and flight testing of a prototype UAS, under the designation RX-3, which will provide direct support to Greek isolated territories and islands, via aerial delivery of lifesaving supplies and dedicated equipment. The system will be based on a large-scale, autonomous, fixed-wing, novel BWB UAV configuration, as well as a portable GCS. Its mission involves cruising to the point of interest for up to 65km, payload delivery, and cruising back to the base of operations. RX-3 payload has been selected to support a wide range of humanitarian missions (life rafts, medical equipment, provisions etc.). The design was based on well-established aircraft design textbooks and methodologies. In-house sizing tools and routines were used to facilitate the layout, aerodynamics, and stability calculations. These tools were adjusted to the needs of UAVs and finetuned to incorporate the unique characteristics of the novel BWB platform. They have also been validated through the design of the HCUAV RX-1, the first large-scale Hellenic Civil UAV for surveillance missions, which has successfully undergone several flight tests [2], [3]. The layout design and sizing procedure is compatible with FAA pt. 23 regulations and supported by high-fidelity aerodynamic analysis (CFD) and structural analysis (FEM) tools. The geometry used for the analyses was generated with the use of existing parametric 3D CAD tools, which allow the changes at the aerial vehicle configuration to be executed with speed and accuracy. The results were imported in a dedicated flight simulator software, for the evaluation of the key performance, aerodynamic and stability specifications of the RX-3. This thesis consists of two project related topics: construction of the flight simulator used to validate the aircraft's performance, and research and analysis of the phenomenon of the Leading-Edge Vortices on the UAV.



Figure I. The DELAER RX-3

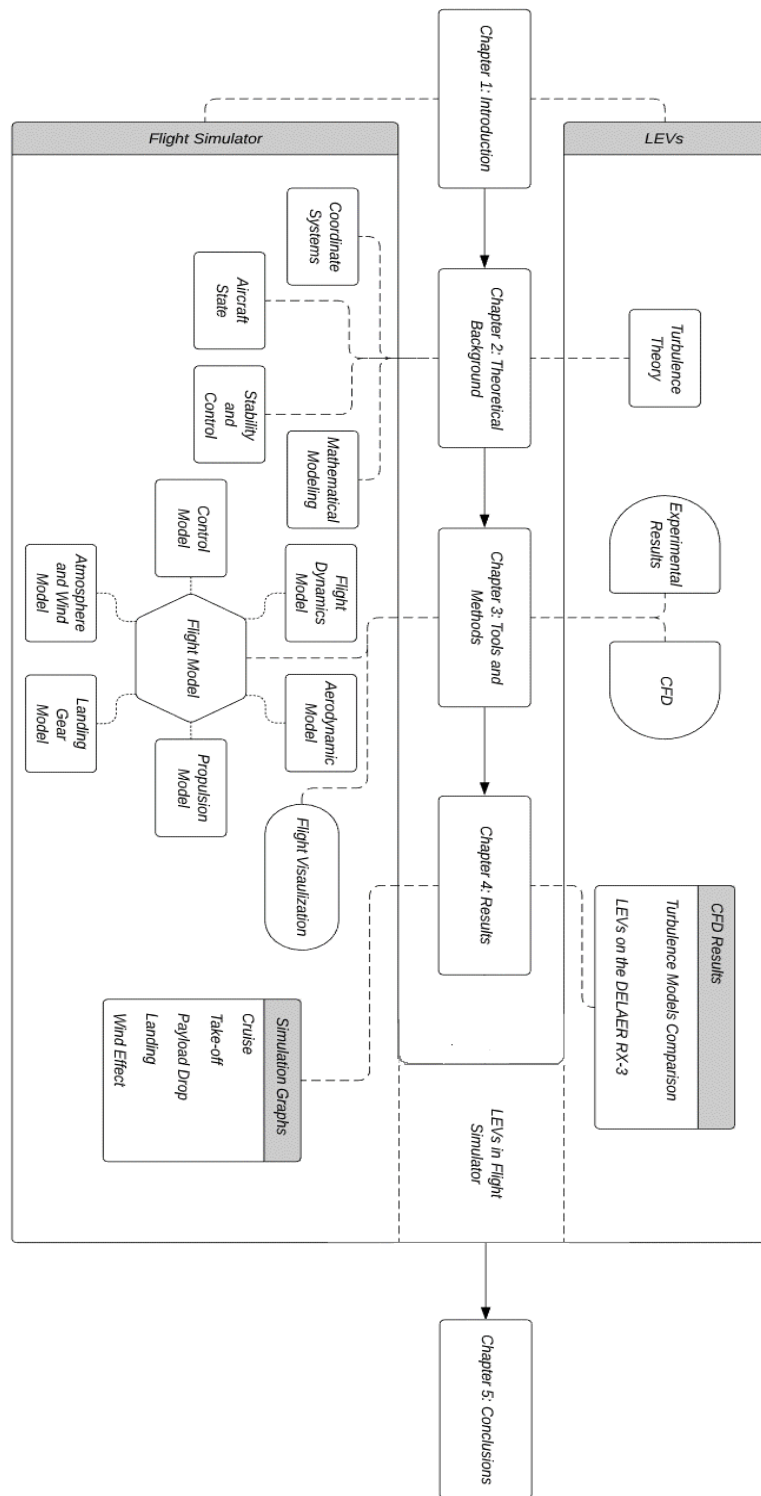


Figure II. Thesis Flowchart

CHAPTER 1

INTRODUCTION

Overview

The DELAER RX-3 Platform

The platform studied is a Blended Wing Body (BWB) Unmanned Aerial Vehicle (UAV), named the DELAER RX-3. A UAV is a powered aerial vehicle that does not carry a human operator, uses aerodynamic forces to provide vehicle lift, can fly autonomously or be piloted remotely, can be expendable or recoverable, and can carry a payload [4]. The term Unmanned Aircraft System (UAS) was adopted by the United States Department of Defense (DoD) and the United States Federal Aviation Administration in 2005 according to their Unmanned Aircraft System Roadmap 2005–2030. The International Civil Aviation Organization (ICAO) and the British Civil Aviation Authority adopted this term, also used in the European Union's Single-European-Sky (SES) Air Traffic Management (ATM) Research (SESAR Joint Undertaking) roadmap for 2020. This term emphasizes the importance of elements other than the aircraft, including elements such as ground control stations, data links and other support equipment. Similar terms are an Unmanned Aircraft Vehicle System (UAVS), Remotely Piloted Aerial Vehicle (RPAV), and Remotely Piloted Aircraft System (RPAS) [5]. The complete Unmanned Aircraft System (UAS) consists of the UAV, a ground-based controller and a system of communications between the two. The flight of UAVs may operate with various degrees of autonomy, either under remote control by a human operator or autonomously by onboard computers. Compared to crewed aircraft, UAVs were originally used for missions too “dull, dirty or dangerous” for humans [6]. While they originated mostly in military applications, their use rapidly expanded to



Figure 1.1. Rotary Wing (left) [7] and Fixed Wing (right) [8] UAV Configurations

commercial, scientific, recreational, agricultural, entertainment and other applications [9]. Civilian UAVs now vastly outnumber military ones. The UAV market is estimated at USD 19.3 billion in 2019 and is projected to reach 45.8 billion USD by 2025, at a compound annual growth rate (CAGR) of 15.5% from 2019 to 2025 [10]. UAV aircrafts currently boil down to two categories, rotary wing and fixed wing, based on their fundamental lifting mechanism. Rotary wing UAVs are relatively cheap and maneuverable, but they are limited to small-scale surveillance purposes and entertainment for the time being, due to their considerable limitations in payload capacity and flight endurance [11]. As for the fixed-wing UAVs, they are ideal solutions for a wide range of operations, such as fire detection, search and rescue, coastline and sea-lane monitoring and security surveillance. Moreover, they are capable of carrying lifesaving supplies payload, such as life rafts, medical equipment, provisions etc., to distant, inaccessible by other means, areas. The fixed wing platform features several advantages, such as low operational cost, the ability to operate under adverse or hazardous conditions, and increased flight endurance, which is one of the most important characteristics when it comes to the abovementioned missions.

As far as the BWB geometry is concerned, it has been of great interest in recent years. The BWB concept has been developed in order to serve as a novel platform for high-speed subsonic commercial airliners and was the outcome of a challenge issued by Dennis Bushnell to the aircraft industry in 1988. Bushnell, the chief scientist of the NASA Langley Research Center, asked if new, innovative thinking could result in a commercial jet transport that would provide a quantum leap in efficiency and performance in comparison to the standard tube-fuselage, swept-wing airplane with jet engines pod-mounted under the wings [12]. The BWB platform is a tailless design that integrates the wing and the fuselage into a continuous structure [13], [14]. In the general case, it consists of a middle section (fuselage) and an outer section (wing), whereas the part in between is the blending area, where the fuselage

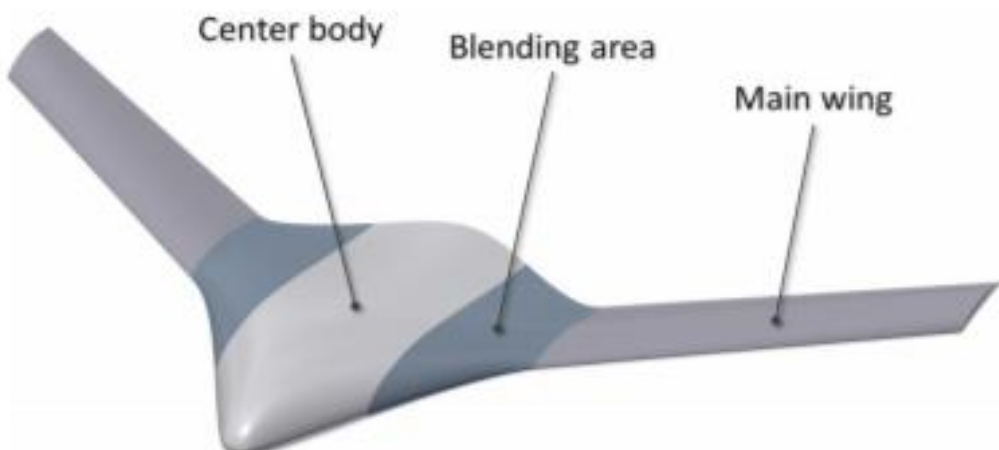


Figure 1.2. Basic Layout of the BWB Configuration [15]

smoothly connects (blends) into the wing geometry (**Figure 1.2**). It features a number of advantages, such as low wetted area to internal volume ratio, potential for elliptic lift distribution, smooth varying cross-section distribution, and adequate space for engine installation on the top of the airframe. Therefore, it represents “a potential breakthrough in subsonic transport efficiency” and is a much promising candidate in fulfilling the targets of the aeronautical industry for low noise emissions, weight reduction, etc. [16]. The maximum lift-to-drag ratio depends on the ratio of the aircraft span to the square root of the product of the induced drag factor and the zero-lift drag, which is proportional to the wetted area of the aircraft. From this relation, one can see that larger wingspan, smaller wetted area, lower skin friction, or less induced drag can all provide potentially substantial improvement in aerodynamic performance [17]. With these advantages it can improve the performance and the operational specifications of aircraft that operate in low subsonic speeds as well, and more specifically in the incompressible flow regime, as is the case of most UAVs.

Flight Simulator

The importance of training has been recognized since the beginning of manned flight. The mythical story of Icarus and Daedalus is usually related to a warning about flying too high, because the heat of the sun would melt the glue used to hold together the feathers of the wings - probably not a correct interpretation of the warning. The more probable warning was about the danger of flying too high without having undergone the necessary training and becoming more acquainted with the controls and performance of the flying machine [18]. A flight simulator is an extremely useful tool which recreates the whole flight, or parts thereof, and the environment around the aircraft, in order for pilots to acquire the aforementioned essential experience. It contains all the equations and tools needed to visualize the airplane's dynamics and its reaction to external factors, such as pilot control, air density changes due to different altitudes, weather conditions etc. The pilot can achieve, test and maintain proficiency in airplane operation and handling, being able to experience the flight environment and learn from mistakes without any risks. It relieves instructors from safety considerations and flight duties and constitutes a cost-effective training solution as it saves crew time, fuel and maintenance of the real aircraft. The flight simulation does not depend on any environmental conditions, while also permitting repeated practice of a particular phase of flight. Accurate replication of numerous environmental and flight conditions is possible through a complete simulation model. Flight simulators utilize different types of software and hardware, depending on the mission they are referring to and the detail needed to achieve their goal. A flight simulator system may consist of multiple displays, control devices, an audio system for communications and a computer system to process control inputs and record flight data. The lower-end, non-professional models are usually based on a personal computer for the recreation of a UAV mission, while the high-end, more realistic and complex ones are based on a grounded copy of a real cockpit, used for complete pilot training.

The highest level of flight simulation on the commercial flights sector is known as Full Flight Simulator (FFS). The history of flight simulators starts back in 1910 when the first ground training airplane was built, known as the Antoinette Trainer, consisted of two half-sections of a barrel. The device was moved manually by instructors to present the pitch and roll motion of an airplane. The prospective pilot, sitting in the top section, was required to line up a reference bar with the horizon, using his controls, as shown in **Figure 1.3**. Since then, flight simulation has become essential in commercial and military applications, thanks to it being the safest way for pilot training. Furthermore, it is now used for many more applications, such as testing new aircrafts and general research on performance optimization. The current thesis falls in the last category, since the model was constructed in order to get a better understanding of the behavior and performance of a new platform. In order to avoid mistakes that could negatively affect the mission, the aircraft's performance and behavior need to be tested before the actual flight. This can be achieved via the flight simulator, making it a major part of the whole aircraft design and performance optimization process. With an accurate dynamic simulation model, every part of the mission can be visualized, from take-off to landing. This way, any unnecessary accidents can be prevented beforehand, saving money and time. In other words, flight simulation can provide a suitable, and less expensive, early stage to real airplane flight [19]. The first part of this thesis is dedicated to creating a realistic flight simulator for a UAV in the low-velocity subsonic regime. The general equations describing the aerodynamics and motion of any normal aircraft are used, with specific modifications in order to match the needs of the BWB geometry and its specific mission circumstances.

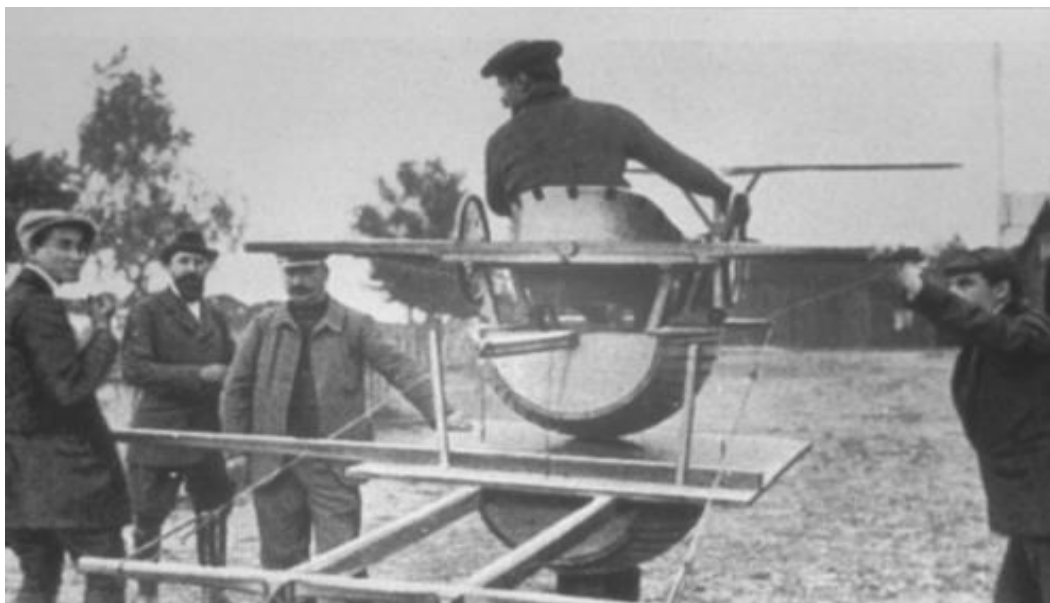


Figure 1.3. The Antoinette Trainer [18]

Leading Edge Vortices

The BWB geometry has plenty of advantages, as mentioned above. However, there is a major drawback related to its stability. Literature research regarding the aerodynamic phenomena over BWB and Delta Wing platforms has been conducted. The research showed that the flow over a non-slender BWB platform is governed by complicated flow structures, the so-called Leading-Edge Vortices, which lead to nonlinear aerodynamic characteristics, such as unstable pitching moment, at high angles of attack. The unstable pitching moment characteristic is associated with flow separation around outboard wing region and inboard vortex breakdown, which causes loss of lift, and this loss of lift generates rapidly increasing nose-up moment at a specific range of angles of attack. This phenomenon is called ‘pitch-break’ or ‘pitch-up’. On the other side, these vortices are capable of providing an increase in lift, under specific circumstances, a fact that makes their presence useful for the aircraft’s performance. Taking into consideration both sides of the phenomenon, it makes it a subject worthy of further research, in order to decide if the vortical structure needs to be totally avoided or it can be exploited in the case at hand. This leads to the second part of the current thesis, where detailed study and analysis of the Leading-Edge Vortices phenomenon takes place. A BWB configuration similar to the DELAER RX-3 had already been investigated experimentally [20] at the Aristotle University of Thessaloniki. The outputs of this study, concerning the leading-edge and tip vortices were used as a reference in the comparison of different CFD results, in order to evaluate which turbulence model predicts with higher accuracy the vortical structure over the BWB configuration. Four different turbulence models, namely Menter’s SST, Transition SST (or γ - Re_θ), Spalart Allmaras with rotation/curvature correction (SA-RC) and Reynolds Stress Model (RSM), were examined. CFD post-processing showed that Transition SST is the most accurate between these turbulence models. The model has also been deemed appropriate for the case of BWB UCAV in Ref. [21]. Consequently, this model was employed to simulate the vortical flow over the DELAER RX-3, for angles of attack ranging from 0° to 16°, in order to examine the leading-edge vortices phenomenon.

Objectives

Flight Simulator

- Construction of the basic flight model, accepting control inputs and including the computation of gravity, aerodynamic and propulsive forces and moments, and then the aircraft's state, by solving the complete set of Equations of Motion, so that that flight can be simulated.
- Implementation of a landing gear model, in order for the forces and moments to be added to the total forces and moments, for the purposes of take-off and landing simulation.
- Implementation of an atmosphere and wind model, including wind turbulence and discrete gusts, in order to simulate flight in hazardous conditions.
- Connection between the flight model and FlightGear simulator software, for real-time visualization of the flight.

Leading-Edge Vortices

- Evaluation of the accuracy of four different turbulence models, concerning the leading-edge and tip vortices over a 40° sweep BWB configuration
- Investigation of the leading-edge vortices phenomenon, by performing CFD simulations on the DELAER RX-3

CHAPTER 2

THEORETICAL BACKGROUND

Coordinate Systems

The various motions, forces, and moments all have coordinate systems or alternatively reference frames in which they are most naturally characterized. For example, in a suitably defined coordinate system, gravity always points downwards. Furthermore, lift is perpendicular to the mean airflow and drag is parallel to it, suggesting a coordinate system in which some axis points in the direction of the relative wind. Therefore, several coordinate systems must be defined. The description of the orientation of one system with respect to another, and determining how the orientation varies with time, are also of great importance [22]. All coordinate systems will be right-handed and orthogonal. For each coordinate system, a specific subscript will be applied to its axes, in order to know which one is used each time.

Earth-Fixed Coordinate System

The first coordinate system found in every simulator is the earth-fixed coordinate system. This system's origin is fixed on a specific spot on the earth surface. The x_E axis points north, y_E points east and z_E points toward the center of the earth (**Figure 2.1**). The E subscript is used for the Earth-fixed coordinate system. In flight simulations in the subsonic regime and low altitude, earth curvature is not important and can be neglected.

Local-Horizontal Coordinate System

Humans tend to think of an airplane's orientation relative to the horizontal, and instruments such as the artificial horizon follow that convention. In addition, many calculations require the airplane's orientation relative to the local horizontal plane. Therefore, the simulator specifies the aircraft's orientation relative to an intermediate axis system. This coordinate system has its origin fixed to any arbitrary point that may be free to move relative to the Earth. For example, the origin may be fixed to the center of gravity (CG) or the aerodynamic center (AC) of the aircraft and move with it. In our case this point will be the AC. The subscript H denotes the local-horizontal reference frame. x_H points due north, y_H points due east and z_H points toward the center of the Earth.

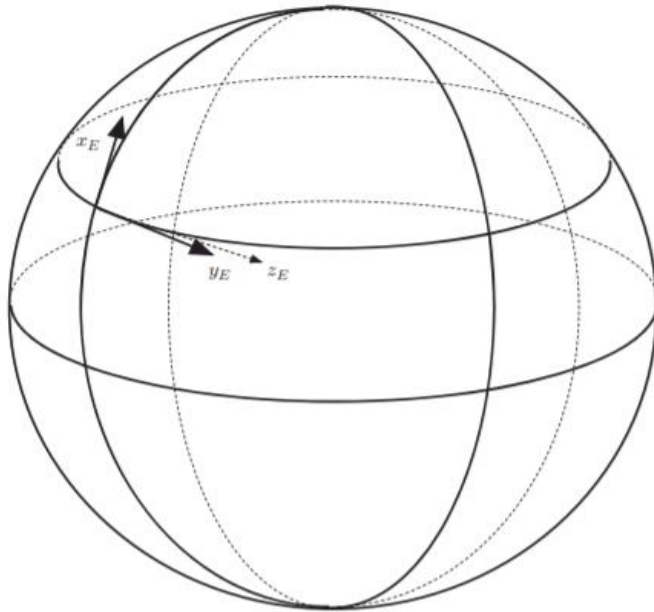


Figure 2.1. Earth-Fixed Coordinate System [22]

Body-Fixed Coordinate System

This is another coordinate system found in every flight simulator. This one is fixed on the body, meaning that it has no translational or angular velocity relative to the aircraft, with its origin most usually coinciding with the center of gravity of the aircraft. However, there are cases where the origin lies on the aerodynamic center of the body, especially when the gravity center is moving during the mission, because of the airplane mass being variable. The mission of the current thesis belongs to the last case, so the origin of the axes coincides with the aircraft's aerodynamic center. x_B lies on the plane of symmetry and points towards the airplane's nose, y_B is perpendicular to x_B and points towards the right wing and finally z_B is perpendicular to the x_B - y_B plane and points downwards. The B subscript is used for the Body-fixed coordinate system.

The body-fixed reference frame makes it easy to define the angular displacement terms: roll, pitch and yaw. Roll is the aircraft's rotation about its longitudinal axis, which coincides with x_B , pitch is the rotation about the lateral axis, which coincides with y_B and yaw is the rotation about z_B . Roll is positive when the right wing "drops", pitch is positive when the nose rises and yaw is positive when the nose moves clockwise, viewed from above, as shown in **Figure 2.2**.

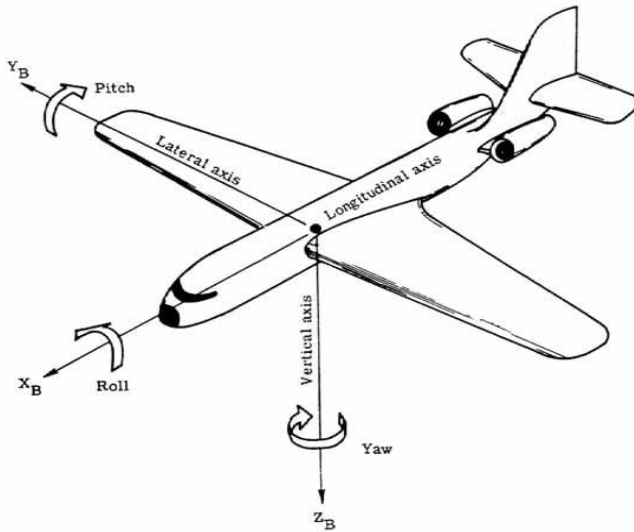


Figure 2.2. Body-Fixed Coordinate System [23]

Wind-Axis Coordinate System

This reference frame is also fixed on the aircraft. The major difference from the body-fixed system is that x_w is parallel to the velocity of the aircraft relative to the air mass, meaning that it doesn't necessarily lie on the symmetry plane. y_w is again perpendicular to x_w , pointing to the right, and z_w lies on the symmetry plane, vertical to the x_w - y_w plane.

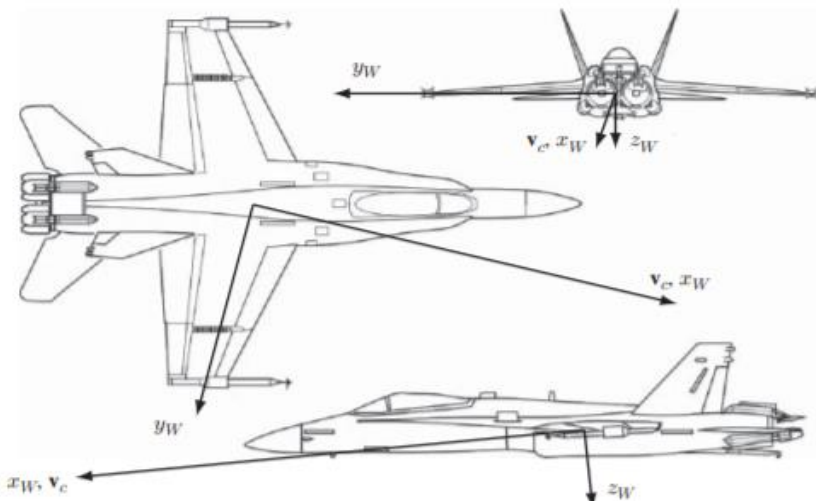


Figure 2.3. Wind-Axis Coordinate System (v_c : velocity relative to the air mass) [22]

The main reason for the wind axis system is that it is more convenient for calculating aerodynamic forces. For instance, lift is, by definition, perpendicular to the relative wind, while drag is parallel. With wind axes, both lift and drag resolve into a force parallel to one of the axes. The transformation from body to wind axes consists of two rotations. First the body axes are rotated about the y -axis through the angle of attack α ; the axes are then rotated about the z -axis through the angle of sideslip β , yielding the wind axes. Angle of attack is positive when the relative wind is from below the x_B axis and sideslip is positive when the relative wind is from the right of the plane of symmetry, as shown in **Figure 2.4**. The angle of attack and the angle of sideslip are defined respectively by:

$$\alpha = \tan^{-1} \left(\frac{w_a}{u_a} \right) \quad (2.1)$$

$$\beta = \sin^{-1} \left(\frac{v_a}{V} \right) \quad (2.2)$$

For navigation, the main concerns are position and velocity with respect to the Earth, whereas for aircraft performance the main concerns are position and velocity with respect to the atmosphere. On the other hand, the direction of a jet engine's propulsive force may often be considered fixed with respect to the body of the aircraft. There are many more coordinate systems describing the position of an aircraft. Mentioning them is beyond the scope of this study, since only the abovementioned ones are used.

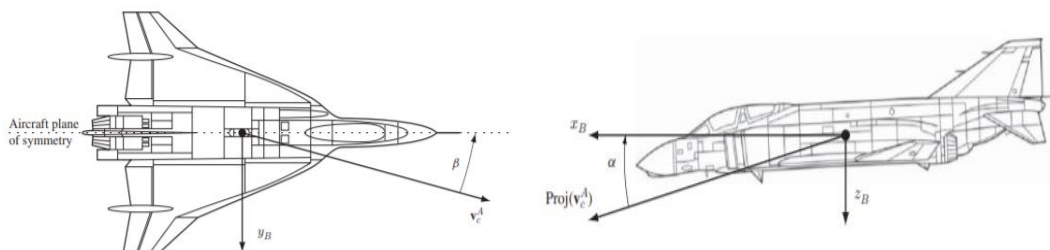


Figure 2.4. Sideslip (left) and Angle of Attack (right) [22]

Latitude and Longitude

Position on the Earth is measured by latitude and longitude. Latitude is denoted by the symbol λ and longitude by the symbol μ . Latitude is measured as positive north and negative south of the equator, $-90 \text{ deg} \leq \lambda \leq +90 \text{ deg}$; and longitude positive east and negative west of zero longitude, $-180 \text{ deg} < \mu \leq +180 \text{ deg}$.

Table 2.1. Coordinate Systems Definition

<i>Coordinate System</i>	<i>Subscript</i>	<i>Definition</i>
<i>Earth-Fixed</i>	E	O: at an arbitrary fixed point at sea level x: pointing North y: pointing East z: pointing to the center of the Earth
		O: aircraft aerodynamic center x: pointing North y: pointing East z: pointing to the center of the Earth
<i>Local-Horizontal</i>	H	O: aircraft aerodynamic center x: pointing North y: pointing East z: pointing to the center of the Earth
		O: aircraft aerodynamic center x: pointing towards the nose y: pointing to the right z: pointing downwards
<i>Body-Fixed</i>	B	O: aircraft aerodynamic center x: in the direction of velocity relative to air y: vertical to x, to the right z: vertical to x-y plane, pointing bottom side
		O: aircraft aerodynamic center x: in the direction of velocity relative to air y: vertical to x, to the right z: vertical to x-y plane, pointing bottom side
<i>Wind</i>	W	O: aircraft aerodynamic center x: in the direction of velocity relative to air y: vertical to x, to the right z: vertical to x-y plane, pointing bottom side

Coordinate System Transformations

An equally important subject to the aforementioned coordinate systems is the relationship between them, and the way a variable can be expressed from a system to another one. For instance, when the external forces acting on the aircraft begin to be summed, they will have to be related to a common reference frame [22]. If a body-fixed system is considered to be the common frame, then it is necessary to be able to take the gravity vector (weight) from the local horizontal reference frame, thrust from some other body-axis frame, and the aerodynamic forces from the wind-axis frame and represent all these forces in the body-fixed frame. Some of these systems are simply related to each other by a simple rotation around their common axis. However, there are more complicated relationships, which vary with time. For example, the orientation of a given body-fixed coordinate system with respect to the wind axes determines certain aerodynamic forces and moments which change that orientation. First, this relationship needs to be defined at a frozen instant in time. The instantaneous relationship is addressed by determining a transformation that will take the representation

of an arbitrary vector in one system and convert it to its representation in the other. There are three well known approaches to finding these transformations, the directions cosines, the Euler angles and the quaternions. In the current thesis only the Euler angles will be discussed, since it's the approach used in the flight simulator.

Initially, the transformation matrix is defined. Consider two reference frames, F_1 and F_2 , and a vector v whose components are known in F_1 , represented as $\{v\}_1$:

$$\{v\}_1 = \begin{Bmatrix} v_{x1} \\ v_{y1} \\ v_{z1} \end{Bmatrix}$$

The goal is to determine the representation of the same vector in F_2 , or in other words $\{v\}_2$:

$$\{v\}_2 = \begin{Bmatrix} v_{x2} \\ v_{y2} \\ v_{z2} \end{Bmatrix}$$

These are linear spaces, so the transformation of the vector is simply a matrix multiplication denoted as $T_{2,1}$, such that $\{v\}_2 = T_{2,1}\{v\}_1$. Transformations such as $T_{2,1}$ are called similarity transformations. The transformations involved in simple relations of orthogonal reference frames have many special properties. The order of subscripts of $T_{2,1}$ is such that the left subscript goes with the system of the vector on the left side of the equation and the right subscript with the vector on the right. For the matrix multiplication to be conformal $T_{2,1}$ must be a 3×3 matrix:

$$T_{2,1} = \begin{bmatrix} t_{11} & t_{12} & t_{13} \\ t_{21} & t_{22} & t_{23} \\ t_{31} & t_{32} & t_{33} \end{bmatrix}$$

The whole point is to figure out how to evaluate the numbers t_{ij} . In order to describe the Euler angles approach, it is essential to know some things about the direction cosine matrix. The aforementioned vector v is the vector sum of the three components $v_{x1}i_1, v_{y1}j_1, v_{z1}k_1$, so it can be replaced by those three components. The projection of v onto x_2 is the same as the

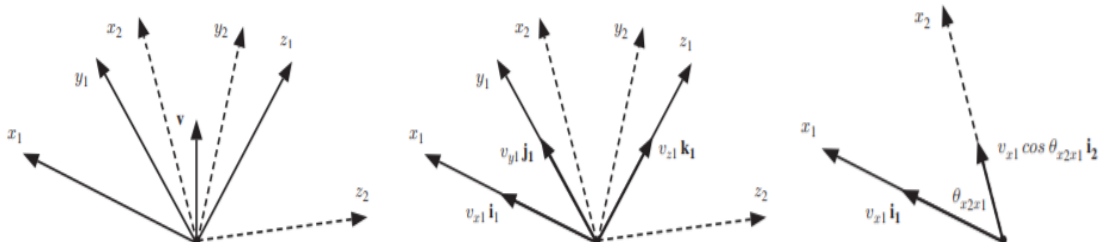


Figure 2.5. a) v represented on F_1 and F_2 , **b)** v in component form in F_1 , **c)** one component in x_1 and x_2 [22]

vector sum of the projections of each of its components onto x_2 . The same principle applies for y_2 and z_2 . The angle generated going from x_2 to x_1 is defined as $\theta_{x_2x_1}$. The projection of $v_{x_1}i_1$ onto x_2 therefore has magnitude $v_{x_1}\cos\theta_{x_2x_1}$ and direction i_2 .

Following the same procedure for all components in all axes results in the following vector-matrix notation:

$$\begin{Bmatrix} v_{x_2} \\ v_{y_2} \\ v_{z_2} \end{Bmatrix} = \begin{bmatrix} \cos\theta_{x_2x_1} & \cos\theta_{x_2y_1} & \cos\theta_{x_2z_1} \\ \cos\theta_{y_2x_1} & \cos\theta_{y_2y_1} & \cos\theta_{y_2z_1} \\ \cos\theta_{z_2x_1} & \cos\theta_{z_2y_1} & \cos\theta_{z_2z_1} \end{bmatrix} \begin{Bmatrix} v_{x_1} \\ v_{y_1} \\ v_{z_1} \end{Bmatrix} \quad (2.3)$$

Clearly this is $\{v\}_2 = T_{2,1}\{v\}_1$, with $t_{ij} = \cos\theta_{(axis)2(axis)1}$ in which i or j is 1 if the corresponding (axis) is x, 2 if (axis) is y and 3 if (axis) is z.

Now the Euler angles are defined. If there are only three independent variables in the direction cosine matrix, then each of the t_{ij} can be expressed in terms of a set of three independent variables. One means of determining these variables is by use of a famous theorem of the Swiss mathematician Leonhard Euler (1707 – 1783). Briefly, this theorem holds that any arbitrarily oriented reference frame may be placed in alignment with any other reference frame by three successive rotations about its axes. The order of selection of axes in these rotations is arbitrary, but the same axis may not be used twice in succession. The rotation sequences are usually denoted by three numbers, 1 for x, 2 for y and 3 for z. The twelve valid sequences are 123, 121, 131, 132, 213, 212, 231, 312, 313, 321 and 323. The angles through which these rotations are performed are called generically Euler angles and are defined as positive according to the right-hand rule for right-handed coordinate systems. The rotation sequence most often used in flight dynamics is the 321, or z-y-x. Considering a rotation from F_1 to F_2 , the first rotation is about z_1 through an angle θ_z , which is positive according to the right-hand rule about the z_1 -axis. With two rotations to go, the resulting alignment in general is oriented with neither F_1 nor F_2 , but some intermediate reference frame, denoted F' . Since the rotation was about z_1 , z' is parallel to it but neither of the other two primed axes are. The next rotation is through an angle θ_y about the axis y' of the first intermediate reference frame to the second one, F'' . Note that $y''=y'$, and neither y'' or z'' are

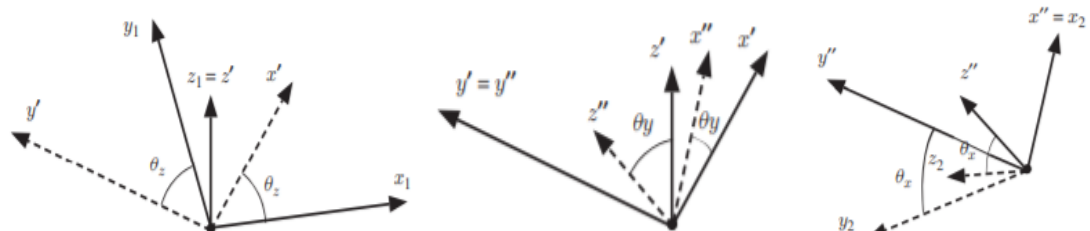


Figure 2.6. Rotations through θ_z , θ_y and θ_x [22]

necessarily axes of either F_1 or F_2 . The final rotation is about x'' through angle θ_x and the final alignment is parallel to the axes of F_2 .

Assuming the three angles are known, the next step is to relate them to the elements of the direction cosine matrix $T_{2,1}$. This can be managed by seeing how the arbitrary vector v is represented in each of the intermediate and final reference frames in terms of its representation in the prior reference frame. Considering first the rotation about z_1 , in terms of direction cosines, the angles between the axes are as follows: between z_1 and z' it is zero; between either z and any of x or y it is 90 degrees; between x_1 and x' or y_1 and y' it is θ_z ; between x_1 and y' it is $90 + \theta_z$ and finally between y_1 and x' it is $90 - \theta_z$. In matrix form:

$$\begin{aligned} \begin{Bmatrix} v_{x'} \\ v_{y'} \\ v_{z'} \end{Bmatrix} &= \begin{bmatrix} \cos\theta_{x'x_1} & \cos\theta_{x'y_1} & \cos\theta_{x'z_1} \\ \cos\theta_{y'x_1} & \cos\theta_{y'y_1} & \cos\theta_{y'z_1} \\ \cos\theta_{z'x_1} & \cos\theta_{z'y_1} & \cos\theta_{z'z_1} \end{bmatrix} \begin{Bmatrix} v_{x_1} \\ v_{y_1} \\ v_{z_1} \end{Bmatrix} \\ &= \begin{bmatrix} \cos\theta_z & \cos(90 - \theta_z) & \cos 90 \\ \cos(90 + \theta_z) & \cos\theta_z & \cos 90 \\ \cos 90 & \cos 90 & \cos 0 \end{bmatrix} \begin{Bmatrix} v_{x_1} \\ v_{y_1} \\ v_{z_1} \end{Bmatrix} \\ &= \begin{bmatrix} \cos\theta_z & \sin\theta_z & 0 \\ -\sin\theta_z & \cos\theta_z & 0 \\ 0 & 0 & 1 \end{bmatrix} \begin{Bmatrix} v_{x_1} \\ v_{y_1} \\ v_{z_1} \end{Bmatrix} \end{aligned} \quad (2.4)$$

In short, $\{v\}' = T_{F',1}\{v\}_1$ in which:

$$T_{F',1} = \begin{bmatrix} \cos\theta_z & \sin\theta_z & 0 \\ -\sin\theta_z & \cos\theta_z & 0 \\ 0 & 0 & 1 \end{bmatrix}$$

Similarly, from the rotations about y' and x'' the following matrices are derived:

$$\begin{aligned} T_{F'',F'} &= \begin{bmatrix} \cos\theta_y & 0 & -\sin\theta_y \\ 0 & 1 & 0 \\ \sin\theta_y & 0 & \cos\theta_y \end{bmatrix} \\ T_{2,F''} &= \begin{bmatrix} 1 & 0 & 0 \\ 0 & \cos\theta_x & \sin\theta_x \\ 0 & -\sin\theta_x & \cos\theta_x \end{bmatrix} \end{aligned}$$

By multiplying the three transformation matrices, $T_{2,1}$ can be derived, which is the transformation matrix needed:

$$T_{2,1} = \begin{bmatrix} \cos\theta_y \cos\theta_z & \cos\theta_y \sin\theta_z & -\sin\theta_y \\ \sin\theta_x \sin\theta_y \cos\theta_z - \cos\theta_x \sin\theta_z & \sin\theta_x \sin\theta_y \sin\theta_z + \cos\theta_x \cos\theta_z & \sin\theta_x \cos\theta_y \\ \cos\theta_x \sin\theta_y \cos\theta_z + \sin\theta_x \sin\theta_z & \cos\theta_x \sin\theta_y \sin\theta_z - \sin\theta_x \cos\theta_z & \cos\theta_x \cos\theta_y \end{bmatrix}$$

Some properties of $T_{2,1}$ are the following:

- $|T_{2,1}| = |T_{2,F''} T_{F'',F'} T_{F',1}| = |T_{2,F''}| |T_{F'',F'}| |T_{F',1}|$
- For a transformation matrix:

$$T_{1,2} = \begin{bmatrix} \cos\varphi_y \cos\varphi_z & \cos\varphi_y \sin\varphi_z & -\sin\varphi_y \\ \sin\varphi_x \sin\varphi_y \cos\varphi_z - \cos\varphi_x \sin\varphi_z & \sin\varphi_x \sin\varphi_y \sin\varphi_z + \cos\varphi_x \cos\varphi_z & \sin\varphi_x \cos\varphi_y \\ \cos\varphi_x \sin\varphi_y \cos\varphi_z + \sin\varphi_x \sin\varphi_z & \cos\varphi_x \sin\varphi_y \sin\varphi_z - \sin\varphi_x \cos\varphi_z & \cos\varphi_x \cos\varphi_y \end{bmatrix}$$

where the angles are physically different from those in $T_{2,1}$, it can be noted that $T_{1,2} = T_{2,1}^{-1} = T_{2,1}^T$ and can be written as:

$$T_{1,2} = \begin{bmatrix} \cos\theta_y \cos\theta_z & \sin\theta_x \sin\theta_y \cos\theta_z - \cos\theta_x \sin\theta_z & \cos\theta_x \sin\theta_y \cos\theta_z + \sin\theta_x \sin\theta_z \\ \cos\theta_y \sin\theta_z & \sin\theta_x \sin\theta_y \sin\theta_z + \cos\theta_x \cos\theta_z & \cos\theta_x \sin\theta_y \sin\theta_z - \sin\theta_x \cos\theta_z \\ -\sin\theta_y & \sin\theta_x \cos\theta_y & \cos\theta_x \cos\theta_y \end{bmatrix}$$

The two matrices are the same, only the definitions of the angles are different. Clearly the relationships among the two sets of angles are non-trivial. In short, the definitions of Euler angles are unique to the rotation sequence used (321, 213, etc.) and the decision as to which frame one goes from and which one goes to in that sequence (F_1 to F_2 or F_2 to F_1).

Specific symbols have been given to the 321 Euler angles for the most frequently occurred transformations. These are summarized as follows:

Table 2.2. Frequent Transformation Angles

$T_{F2,F1}$	ϑ_x	ϑ_y	ϑ_z
$T_{B,H}$	ϕ	θ	ψ
$T_{W,H}$	μ	γ	χ
$T_{B,W}$	σ	α	$-\beta$

Finally, there is a principal range of values of the Euler angles, which is fixed largely by convention and may vary according to the application. In the current study, the convention is:

$$-\pi \leq \theta_x \leq \pi$$

$$-\pi/2 \leq \theta_y \leq \pi/2$$

$$0 \leq \theta_z \leq 2\pi$$

which is the most frequently used in flight dynamics. This convention may cause several problems to the simulation, in case of the angles getting values outside of their ranges in any moment during the mission. Those problems can be overcome using the quaternions approach instead of the Euler angles. However, this approach is way more complicated, with

no physical substance. This, in combination with the fact that the current aircraft's mission lies inside the abovementioned ranges, led to the selection of the Euler angles approach.

Aircraft State

A major set of variables for the flight simulator is the one constituted by the aircraft's state variables. These variables, as their name declares, describe the state of the airplane at every instant during the simulation. There are three position states and three velocity states associated with the translational motion of the aircraft. Similarly, there are three angular position and three angular velocity states associated with the rotational motion [24]. The state variables are listed in **Table 2.3**. There are cases where instead of the body axes velocity components (u, v, w), airspeed (V), angle of attack (α) and sideslip (β) are preferred, but in the model at hand, the state variables of **Table 2.3** were selected. Occasionally, the aircraft's altitude h will be used instead of z_E :

$$h = -z_E$$

Table 2.3. Aircraft State Vector

Symbol	Description
x_E	Position along the x_E -axis
y_E	Position along the y_E -axis
z_E	Position along the z_E -axis
u	Body Velocity component on the x_B -axis
v	Body Velocity component on the y_B -axis
w	Body Velocity component on the z_B -axis
ϕ	Roll Euler Angle
θ	Pitch Euler Angle
ψ	Yaw Euler Angle
p	Roll Rate measured along the x_B -axis
q	Pitch Rate measured along the y_B -axis
r	Yaw Rate measured along the z_B -axis

These variables, along with their time derivatives, called state rates, constitute the main part of the simulation model, since all other parts are utilized in order to calculate the aircraft's state in every loop.

Stability and Control

By the start of the twentieth century, the aeronautical community had solved many of the technical problems necessary for achieving powered flight of a heavier-than-air aircraft. One of the problems still beyond the grasp of these early investigators was a lack of understanding of the relationship between stability and control, as well as the influence of the pilot on the pilot-machine system [25]. Stability is the tendency, or lack of it, of an airplane to fly at a prescribed flight condition and its ability to return to its former condition, after a disturbance, without the participation of the pilot or a device. The disturbance may be generated by the pilot's control actions or by atmospheric phenomena, such as wind gusts, wind gradients or turbulent air. Control is the ability of a pilot or a device to change the airplane's flight conditions. An aircraft must have sufficient stability so that the pilot does not become fatigued by constantly having to control the aircraft owing to external disturbances. One of the essential conditions for an aircraft to fly its mission successfully is that it must be able to achieve equilibrium flight. The concept of equilibrium flight, when the aircraft is flying straight, at constant speed and altitude, is a major part of the mission, also called cruise. At equilibrium, the sum of all forces and moments acting on the body must equal zero. For example, at cruise, lift equals weight and thrust equals drag. Moreover, no net rotating moments are acting on the aircraft. But what if the airplane moves out of equilibrium flight,

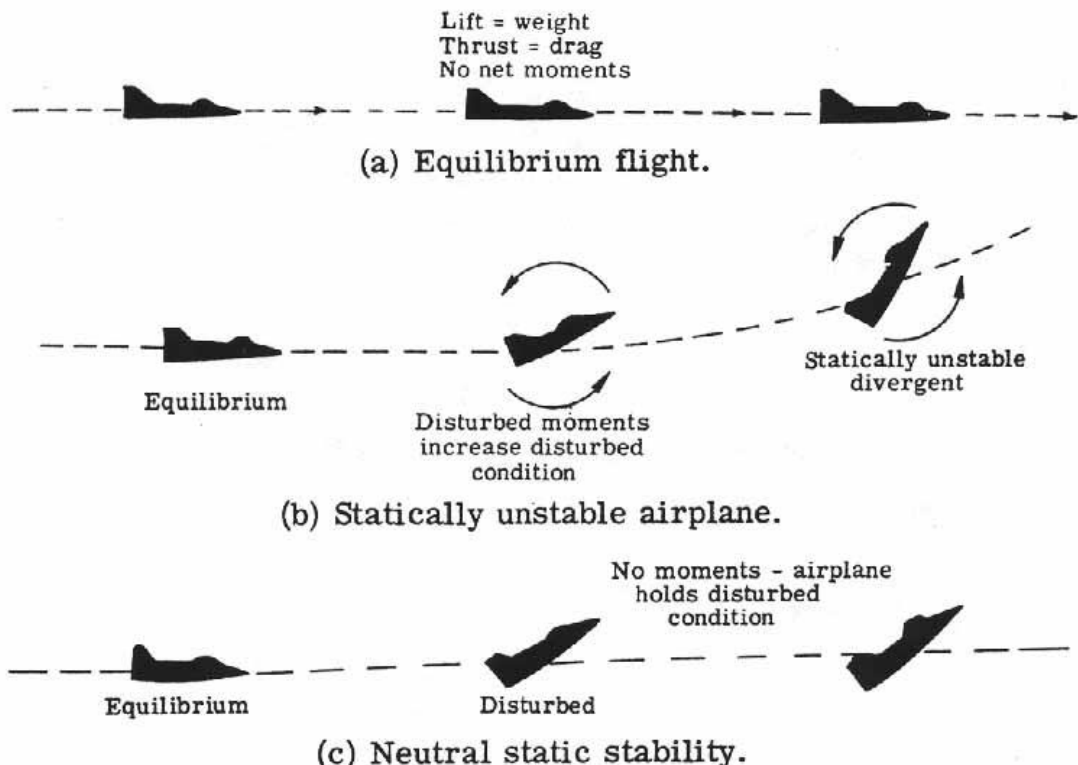


Figure 2.7. Aircraft Static Stability Cases [26]

because of any disturbance, such as air turbulence or a wind gust? Will it finally return to equilibrium or will it get further disturbed? The answer to these questions lies on the concept of static and dynamic stability.

Static stability is the initial tendency of the vehicle to return to its equilibrium state after a disturbance. If the aircraft is statically stable, reacting forces and moments will be generated, restoring its equilibrium condition. In case of it holding its disturbed position, it means that it is statically neutral. Finally, if the initial disturbance worsens, due to the moments and forces enhancing it, the airplane is statically unstable.

Flight stability and control can be categorized in relation to the axes they are referred to. The first and most important category is the longitudinal, which is associated with the motion inside the x-z plane, with the wings always leveled. The second one is the lateral-directional, which consists of rolling, yawing and sideslipping, at constant elevation angle. In aeronautical terms, longitudinal static stability involves the generation of a restoring (nose-down) pitching moment in response of an increase in the angle of attack, without any control action from the pilot, as mentioned above. Moreover, a steady flight condition is defined balanced, if the resultant force and moment about the center of gravity are both zero, that is the aircraft is in equilibrium. In particular, this requires the pitching moment to be zero. Thus, static analysis

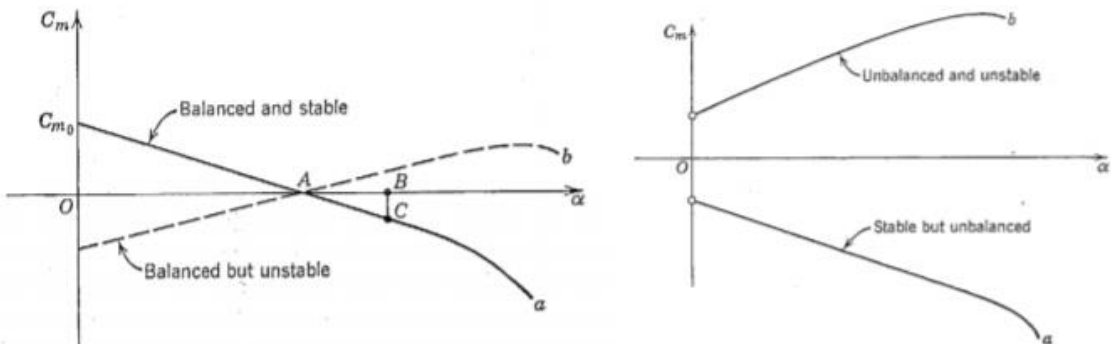


Figure 2.8. Pitching Moment versus Angle of Attack Curves [27]

suggests that, for an aircraft to be statically stable in pitch, the variation in pitching moment with angle of attack must be negative; then, for an equilibrium condition to exist, the pitching moment at zero angle of attack must be positive:

$$C_{m\alpha} < 0$$

$$C_{m_0} > 0$$

A mathematical analysis of the longitudinal static stability of a complete standard aircraft yields the position of the point at which the resultant lift is applied, called neutral point. Since the pitching moment of an isolated surface about its AC can be safely considered invariant

with α , it follows that the resultant aerodynamic moment of the aircraft about that specific point is constant with α . On this basis, it is possible to express the variation in pitching moment due to changes in α , as:

$$C_{m_\alpha} = -C_{L_\alpha}(k_n - k) \quad (2.5)$$

where the term in brackets denotes the dimensionless distance of the NP from the CG, positive for CG fore of the NP. It is called the static margin (K), usually quoted in percentage of the mean aerodynamic chord, and it quantifies the margin of movement of the CG prior to reaching the stability limit. At first analysis, the static margin is a measure of the static stability of the airplane with respect to α disturbances. It follows that the neutral point corresponds to the AC of the complete aircraft, that is to the position of CG at which C_{m_α} is zero and static stability is neutral. The larger the surface and the moment arm of the tail, the further aft the neutral point moves. If the CG is behind the neutral point, the aircraft is longitudinally unstable ($K < 0$), and active inputs to the control surfaces are required to maintain steady flight. It should be noted, though, that the trade-off of reduced stability is an increase in responsiveness to commands, i.e. an improvement in maneuverability, a concept antithetical to stability. Indeed, an aircraft with a large static margin is very stable, but also sluggish to respond to commands and more prone to saturate the controls, due to their reduced effectiveness. The value of the static margin is of critical importance in the design of an aircraft, not only because it represents the main indicator of the stability of the design, but also because, ultimately, it determines the controllability and handling qualities of the vehicle [27].

Directional stability is concerned with the static stability of the aircraft about the z-axis [25]. It is desirable that the aircraft should tend to return to an equilibrium condition when subjected to some form of yawing disturbance, by developing a yawing moment which will restore the aircraft to its equilibrium state. In **Figure 2.9**, airplane 1 will develop the essential restoring moment after being disturbed to a positive sideslip angle β . On the contrary, airplane 2 will produce a moment which will tend to increase β . The conclusion is that, in order for the airplane to have static directional stability, the slope of the yawing moment curve versus β must be positive:

$$C_{n_\beta} > 0$$

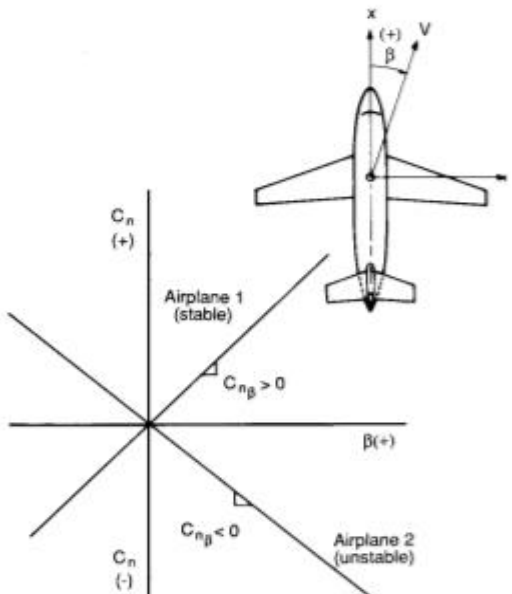


Figure 2.9. C_{n_β} for Static Directional Stability [25]

Lateral stability is the stability of the aircraft about the x-axis. An aircraft possesses static lateral stability if, when it is disturbed from a wings-level attitude, a restoring rolling moment is developed. This moment is a function of the sideslip angle. The requirement in this case is that:

$$C_{l\beta} < 0$$

The main contributor to $C_{l\beta}$ is the wing dihedral angle, which is defined as the spanwise inclination of the wing with respect to the horizontal. If the wing tip is higher than the root section, then the dihedral angle is positive. When an aircraft is disturbed from a wings-level attitude, it will begin to sideslip. This results to a component of the relative wind to be directed toward the side of the airplane. The leading wing experiences an increased angle of attack and consequently an increase in lift. The trailing wing experiences the opposite effect. This leads to a rolling restoring moment that tries to bring the wing back to the wings-level attitude and is known as the “dihedral effect”. Wing sweep also contributes to the dihedral effect. In the case of a sweptback wing, the windward wing has an effective decrease in sweep angle, which results in a higher lift coefficient for a given angle of attack. Therefore, it will experience more lift than the trailing wing, resulting to the essential restoring roll moment. Additionally, wing position along the z-axis with respect to the fuselage, has an influence on the dihedral effect. A low wing position leads to a negative dihedral effect and a high wing position leads to a positive one.

As for dynamic stability, it is related with the time history of the motion of the vehicle after it is disturbed from its equilibrium state. For instance, in case of a positive pitching moment, the aircraft will nose up, then overshoot, then nose down, overshoot again, etc. If that oscillatory motion decays with time, leading the body to its former equilibrium condition, it means that the body is dynamically stable. On the other hand, if the amplitude of the motion increases, the airplane is dynamically unstable. There is also the case when the amplitude of the motion has a constant magnitude, which means that the aircraft is dynamically neutral. The reduction of the disturbance with time indicates that there is resistance to the motion and, therefore, that energy is dissipated. This dissipation of energy is called positive damping. As pictured in **Figure 2.10**, an aircraft can be statically stable but dynamically unstable at the same time. However, if it is dynamically stable, it must be statically stable too. In case of it being statically and dynamically stable, we say that the aircraft operates under “trim” conditions. At that case, it can be flown “hands off” by the pilot, with no control necessary, except the case a change in equilibrium condition is needed.

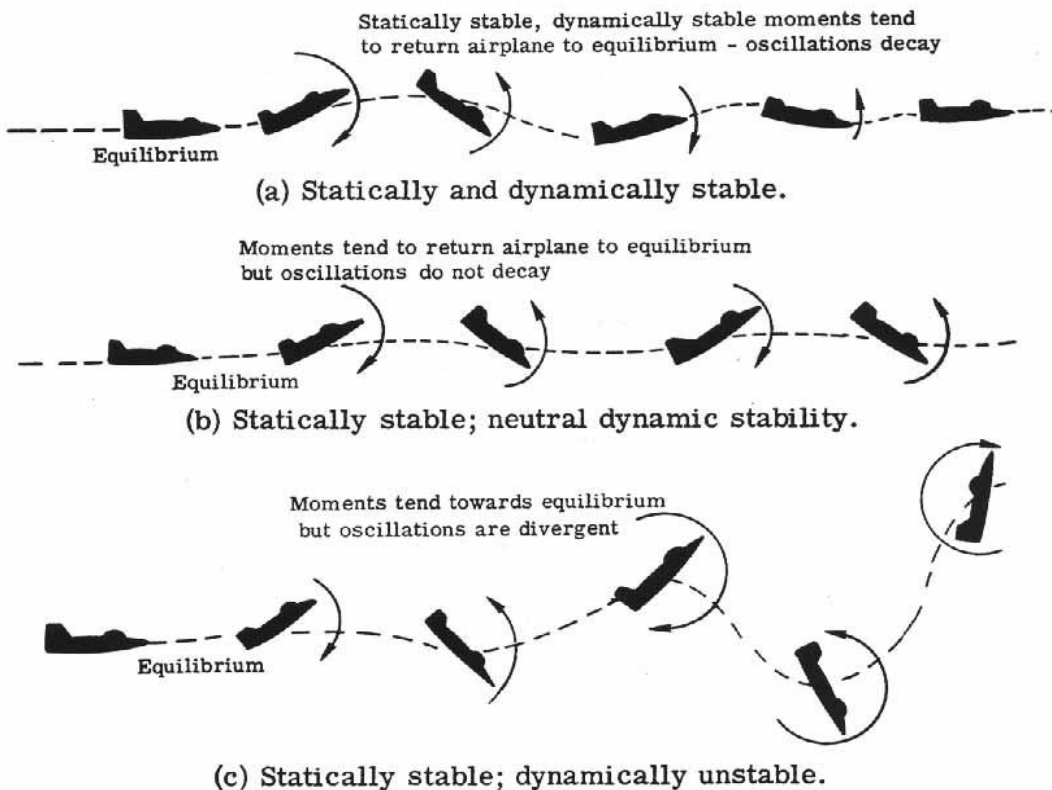


Figure 2.10. Aircraft Dynamic Stability Cases [26]

Of particular interest to the pilot and designer is the degree of dynamic stability. Dynamic stability is usually specified by the time needed for a disturbance to be damped to half of its initial amplitude or, in case of an unstable motion, the time needed for the initial amplitude to double. In case of an oscillatory motion, the frequency and period of the motion are of great importance.

Control of an aircraft can be achieved by providing an incremental lift force on one or more of the aircraft's lifting surfaces. The incremental lift force can be produced by deflecting the entire lifting surface or by deflecting a control surface incorporated in the lifting surface [25]. Owning the fact that the control surfaces are located at some distance from the aerodynamic center, the incremental lift force creates a moment about the aircraft's AC. The typical set of control surfaces includes the elevator, the ailerons and the rudder. Elevators contribute to pitch control, ailerons to roll control and rudders to yaw control. As for throttle, which is considered as another control tool, its contribution depends on the position of the engine related to the AC, as well as its orientation. The BWB platform is not a typical geometry and its control surfaces are consequently not the typical ones. More specifically, the control surfaces of the DELAER RX-3 consist of two elevons, one on each wing's trailing edge, and two

ruddervators on its winglets. An elevon, as its name declares, is a combination of an elevator and an aileron, used on tailless aircrafts. This device is capable of providing pitch control, when both elevons are deflected in the same direction, or roll control when they have opposite deflections. As for the ruddervators, they are a combination of a rudder and an elevator. They are mostly used as rudders, providing yaw control by deflecting them in the same direction. However, when deflected in opposite direction, they work as elevators, contributing in pitch control, since the winglets are slightly turned outwards. The advantage of those surfaces is the greater lever arm they have, in comparison with the typical ones, since they are at the wings' edges, away from the aircraft's CG and AC, contributing notably in stability and control with their resulting moments. Positive deflections of the primary flight controls will be determined by a right-hand rule in which the thumb points along the axis of the primary moment being generated, and the curled fingers point in the direction of positive deflection. Thus, "aileron" deflection is positive when the right elevon is trailing-edge down and the left is up, "elevator" deflection is positive when both elevons are trailing edge down, and "rudder" deflection is positive when both ruddervators are trailing-edge right. As for the engine, it is positioned on the aircraft's symmetry plane, higher than the AC, with an angle of 2 degrees from the x_B -axis. This means that throttle contributes solely to pitch control, since thrust acts only in the x_B - z_B plane.

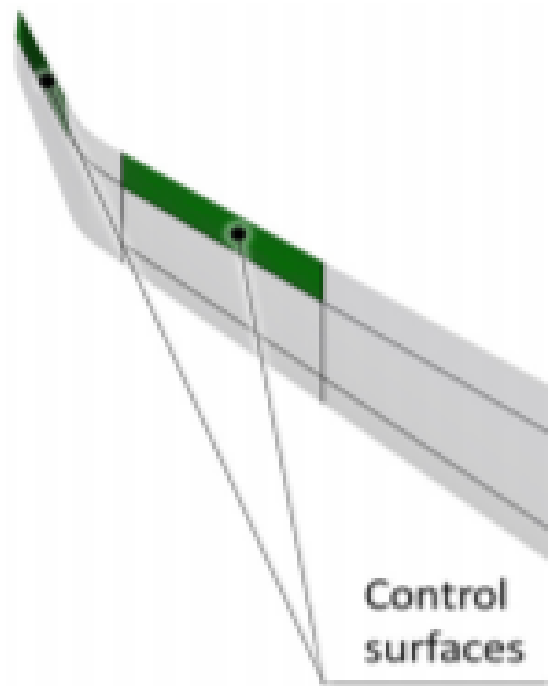


Figure 2.11. DELAER RX-3's Control Surfaces

Mathematical Modeling for Simulation

Piloted flight simulation is realized by mathematical modeling of the aircraft's aerodynamic, flight control, propulsion, landing gear and environmental characteristics, i.e. the response to atmospheric turbulence and wind shear. Mathematical models, used to simulate modern aircraft, consist of an extensive set of non-linear differential equations with large amounts of aerodynamic function data. In addition, these equations contain arbitrary discrete and continuous forcing functions, and a multiplicity of constraints imposed on the states of the different aircraft systems. From the resulting forces and moments, generated by these systems, the equations of motion are composed and solved by the computer using an appropriate integration algorithm. This process allows the simulation of the complete range of static and dynamic aircraft operating conditions, including landing and takeoff, ground-handling and emergency situations such as stalling and component malfunction. Because there is a 'pilot-in-the-loop', and/or hardware and avionics in the loop, the complete set of equations must be solved in real-time. This means that the simulated events must occur within the same time scale as they would occur in the real aircraft. Therefore, in real-time flight simulation, the computer must carry out all calculations in the mathematical model, including input/output, a sufficient number of times per second to achieve dynamic fidelity of the highest natural frequency present in the simulation response. More information can be found in Ref. [28].

Equations of Motion

The motions of an airplane are affected by the external forces (F) and moments (M) resulting from flight through the atmosphere, engine thrust and landing gear forces during take-off and landing, acting on the airplane. The airplane motions are calculated using the equations of motion as derived from Newton's laws:

$$dF = \frac{d}{dt}(dm \cdot V) \quad (2.6)$$

where point mass dm moves with time varying velocity V under the influence of a force dF , and:

$$dM = \frac{d}{dt}(dmr \times V) \quad (2.7)$$

where the moment of the force about a fixed point, dM , is equal to the time derivative of the angular momentum of the body relative to that same fixed point.

The equations of motion of an airplane can be derived on the basis of the above two expressions, by adding up the forces acting on all parts of the airplane as well as the moments

due to these forces about the CG or the AC of the airplane, as explained in detail in Ref. [22]. The resulting general equations of motion of an airplane in the body axes reference frame are as follows:

$$F_x = -mg\sin\theta + X = m(\dot{u} + qw - rv) \quad (2.8)$$

$$F_y = mg\cos\theta\sin\varphi + Y = m(\dot{v} + ru - pw) \quad (2.9)$$

$$F_z = mg\cos\theta\cos\varphi + Z = m(\dot{w} + pv - qu) \quad (2.10)$$

$$M_x = L = I_{xx}\dot{p} + (I_{zz} - I_{yy})qr - I_{xz}(\dot{r} + pq) \quad (2.11)$$

$$M_y = M = I_{yy}\dot{q} + (I_{xx} - I_{zz})rp - I_{xz}(p^2 - r^2) \quad (2.12)$$

$$M_z = N = I_{zz}\dot{r} + (I_{yy} - I_{xx})pq - I_{xz}(\dot{p} - rq) \quad (2.13)$$

To these equations, the following kinematic equations should be added, expressing the relations between the rates of change of the airplane's attitude angles and the angular velocities about the airplane body axes:

$$\dot{\phi} = p + (q\sin\varphi + r\cos\varphi)\tan\theta \quad (2.14)$$

$$\dot{\theta} = q\cos\varphi - r\sin\varphi \quad (2.15)$$

$$\dot{\psi} = q\frac{\sin\varphi}{\cos\theta} + r\frac{\cos\varphi}{\cos\theta} \quad (2.16)$$

The above equations describe the most general motions an airplane can perform and are based on the following restrictive assumptions:

- The airplane's mass is constant in the time interval during which the motions of the airplane are studied.
- The airplane is a rigid body in the motion under consideration.
- The mass distribution of the airplane is symmetric relative to the x-z plane.
- The rotation of the earth in space, as well as the curvature of the earth's surface are negligible.

In real-time flight simulation, the non-linear equations of motion, covering the complete flight envelope, are used, starting from the total force and moments as given above. Rearranging these equations and introducing the inertia parameters results in the following equations, where all time derivatives appear in the left-hand side:

$$\dot{u} = \frac{X}{m} - g\sin\theta - qw + rv \quad (2.17)$$

$$\dot{v} = \frac{Y}{m} + g \cos\theta \sin\varphi + pw - ru \quad (2.18)$$

$$\dot{w} = \frac{Z}{m} + g \cos\theta \cos\varphi - pv + qu \quad (2.19)$$

$$\dot{p} = \frac{I_{zz}}{I_D} [L + I_{xz}pq - (I_{zz} - I_{yy})qr] + \frac{I_{xz}}{I_D} [N - I_{xz}qr - (I_{yy} - I_{xx})pq] \quad (2.20)$$

$$\dot{q} = \frac{1}{I_{yy}} [M - (I_{xx} - I_{zz})pr - I_{xz}(p^2 - r^2)] \quad (2.21)$$

$$\dot{r} = \frac{I_{xz}}{I_D} [L + I_{xz}pq - (I_{zz} - I_{yy})qr] + \frac{I_{xx}}{I_D} [N - I_{xz}qr - (I_{yy} - I_{xx})pq] \quad (2.22)$$

where: $I_D = I_{xx}I_{zz} - I_{xz}^2$

From the components u, v and w of the airspeed V of the aircraft CG relative to the ambient air, the components of V along the axes of the earth reference frame are computed:

$$\dot{x}_E = [ucos\theta + (vsin\varphi + wcos\varphi)sin\theta]cos\psi - (vcos\varphi - wsing\varphi)sin\psi \quad (2.23)$$

$$\dot{y}_E = [ucos\theta + (vsin\varphi + wcos\varphi)sin\theta]sin\psi + (vcos\varphi - wsing\varphi)cos\psi \quad (2.24)$$

$$\dot{z}_E = -usin\theta + (vsin\varphi + wcos\varphi)cos\theta \quad (2.25)$$

All of the aforementioned equations constitute the complete set of the equations of motion of an airplane. However, they are independent of a particular airplane. The external forces X, Y and Z and moments L, M and N are those generated by the aerodynamics, engine and landing gear.

The aforementioned set of equations of motion is based on the assumption of constant mass. In this case, the reduction of mass, caused by the fuel consumption with time, is taken into consideration, as well as the step change in mass when the payload drops. In other words, there is an $\dot{m}_f \neq 0$. The differentiation from the general set of equations of motion can be found in reference [29] and is presented below.

$$\dot{V}_B = \frac{F_B}{m_s + m_f} - \frac{\dot{m}_f}{m_s + m_f} V_B - \omega_B \times V_B \quad (2.26)$$

$$\dot{\omega}_B = I^{-1}M_B + I^{-1}[\omega_B \times (I\omega_B)] - I^{-1}\dot{I}\omega_B \quad (2.27)$$

$$\dot{r}_E = T_{H,B}^T V_B \quad (2.28)$$

$$\dot{T}_{H,B} = -\Omega T_{H,B} \quad (2.29)$$

where:

- $V_B = \begin{bmatrix} u \\ v \\ w \end{bmatrix}$, $\omega_B = \begin{bmatrix} p \\ q \\ r \end{bmatrix}$, $\dot{r}_E = \begin{bmatrix} \dot{x}_E \\ \dot{y}_E \\ \dot{z}_E \end{bmatrix}$
- F_B and M_B are the sums of the aerodynamic, gravity, propulsive and landing gear forces and moments respectively on the body-fixed reference frame.
- m_s is the solid aircraft mass, which is constant.
- m_f is the fuel mass, which is variable with time.
- \dot{m}_f is the rate of change of the fuel mass with time, which has a negative value since fuel is consumed.
- I is the inertia matrix.
- $T_{H,B}$ is the rotation matrix from body to horizontal axes.
- $\Omega = \begin{bmatrix} 0 & -r & q \\ r & 0 & -p \\ -q & p & 0 \end{bmatrix}$

Aerodynamic Forces and Moments

The aerodynamic forces and moments on a body, no matter its shape, are due to only two basic sources:

- Pressure distribution over the body surface
- Shear stress distribution over the body surface

The only mechanisms nature has for imposing a force to a body moving through a fluid are pressure distribution, which is normal to the surface, and shear stress distribution, which is tangential [12]. Shear stress is caused by friction between the body and the air.

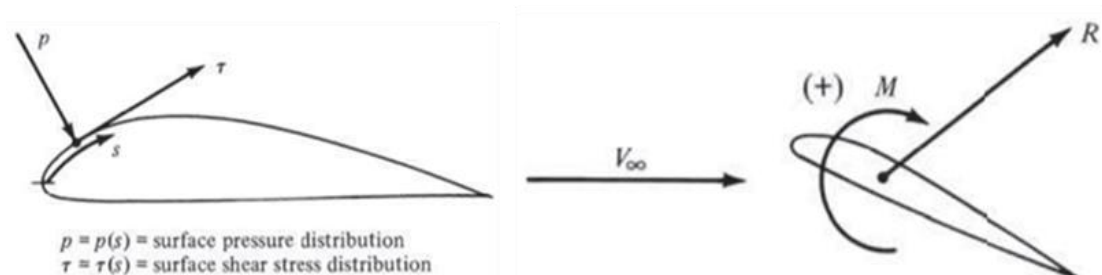


Figure 2.12. Pressure and shear stress on an airfoil and the Resultant Aerodynamic Force and Moment [12]

The net effect of the p and τ distributions integrated over the complete body surface is a resultant aerodynamic force R and moment M on the body (**Figure 2.12**). V_∞ is the relative wind velocity, defined as the velocity far ahead of the body (freestream velocity). Hence, by definition, the lift and drag forces are the components of R perpendicular and parallel to V_∞ , respectively. In the field of aerodynamics and aircraft design, lift (L) is the force used to counter gravity, whereas drag (D) is the cost that a flying body must “pay” to retain its motion. Consequently, the lift-to-drag (L/D) ratio can be defined as an efficiency parameter.

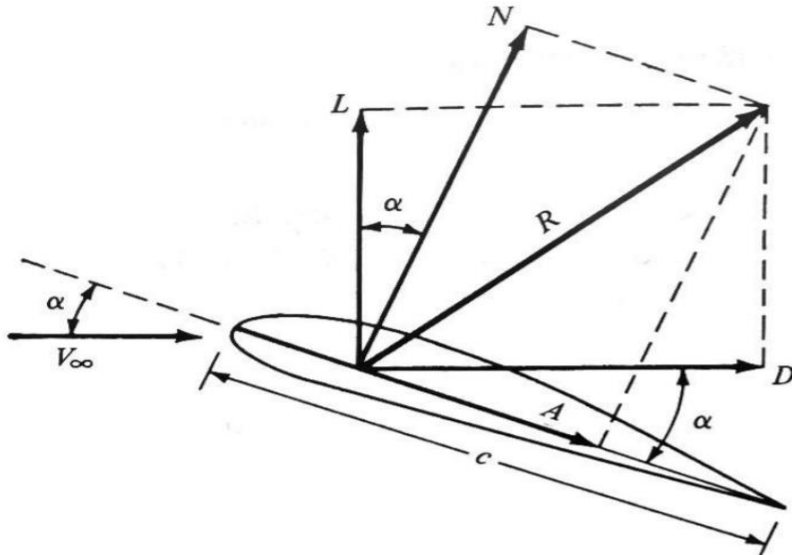


Figure 2.13. Aerodynamic Forces on an Airfoil [12]

Realistic modeling of the aerodynamic forces and moments is very difficult and time inefficient. They are complex functions of the airplane’s state and control variables, as well as the local environment. The relationships get even more complicated considering the interactions between different components of the aircraft, such as wings, control surfaces etc, and external interactions. There are different levels of complexity in aerodynamic modeling. The simplest models are accurate only near a certain trim condition, but there are more sophisticated ones, which are accurate for the whole normal flight envelope, except stall or other unusual situations. Such models are the polynomial ones. This is the category this flight simulator’s model falls into. The model must use non-dimensionalized forces and moments. It is well known from basic aerodynamics that forces are made non-dimensional by dividing them by the dynamic pressure \bar{q} and a characteristic area S , and moments by \bar{q}, S and a characteristic length, which is the wing mean chord \bar{c} for pitching moment non-dimensionalization and the wingspan b for rolling and yawing moments. The dynamic

pressure depends on the local density ρ of the atmosphere, which depends on the altitude h the aircraft is flying, and the velocity V of the aircraft relative to the air mass:

$$\bar{q} = \frac{1}{2} \rho V^2 \quad (2.30)$$

The non-dimensional quantity of a force or moment is denoted as a coefficient C with the appropriate subscript, depending on which force or moment it refers to:

$$C_D = \frac{D}{\bar{q}S}, C_L = \frac{L}{\bar{q}S}, C_Y = \frac{Y}{\bar{q}S} \quad (2.31 - 2.33)$$

$$C_l = \frac{L}{\bar{q}Sb}, C_m = \frac{M}{\bar{q}Sc}, C_n = \frac{N}{\bar{q}Sb} \quad (2.34 - 2.36)$$

These coefficients are dependent on other variables. Each one of them is a combination of functions of these variables, which are finally summed to give the total coefficient. Clearly, some of these dependencies are more important, and some are affecting the forces and moments at such a low level, that they can be neglected for the purposes of the current mission. The most important dependencies are presented below:

$$C_D = C_D[M, \alpha, \delta_m]$$

$$C_Y = C_Y[\beta, \hat{p}, \hat{r}, \delta_n]$$

$$C_L = C_L[M, \alpha, \hat{q}, \delta_m]$$

$$C_l = C_l[\beta, \hat{p}, \hat{r}, \delta_l, \delta_n]$$

$$C_m = C_m[M, \alpha, \hat{q}, \delta_m]$$

$$C_n = C_n[\beta, \hat{p}, \hat{r}, \delta_l, \delta_n]$$

One of the dependencies is this on velocity, which is primarily due to Mach effects and affects most of the aerodynamic coefficients. However, in the current mission, the low Mach subsonic regime makes this effect negligible, as stated in a previous NASA study [30]. The angular velocity dependencies, p , q and r are non-dimensionalized too:

$$\hat{p} = \frac{pb}{V}, \hat{q} = \frac{q\bar{c}}{V}, \hat{r} = \frac{rb}{V} \quad (2.37 - 2.39)$$

As for the control deflection dependencies, they represent the roll (δ_l), pitch (δ_m) and yaw (δ_n) control. These are the typical terms for these deflections. However, in the BWB case, they must be matched to their corresponding control surfaces deflections. More specifically:

- δ_{ee} : elevon deflection to function as elevator, contributing to pitch control
- δ_{er} : elevon deflection to function as aileron, contributing to roll control
- δ_{re} : ruddervator deflection to function as elevator, contributing to pitch control
- δ_{rr} : ruddervator deflection to function as rudder, contributing to yaw control

The current model falls into the polynomial models' category, as mentioned above. Polynomial models represent the resultant aerodynamic forces and moments as polynomial functions of state variables and control variables. The polynomials can have terms in more than one variable. One fact considering airplane aerodynamics is that a mostly linear polynomial model can be fairly accurate for a wide range of flight conditions. Certain phenomena cause the relative linearity of the airplane's behavior to break down, such as stall (high angles of attack) and drag divergence (high Mach numbers), to name a few. However, in flight regimes not involving stall or drag divergence, a mostly linear model can be quite accurate. In order for a polynomial model to work well, it must calculate aerodynamic forces and moments about the reference point in body axes. The force coefficients given above are the wind-axis representations of lift and drag (C_L and C_D) and the body-axis representation of side force (C_Y). This mixed system is transformed to C_X , C_Y and C_Z as follows:

$$\begin{bmatrix} C_X \\ C_Y \\ C_Z \end{bmatrix} = \begin{bmatrix} \cos\alpha\cos\beta & -\cos\alpha\sin\beta & -\sin\alpha \\ 0 & 1 & 0 \\ \sin\alpha\cos\beta & -\sin\alpha\sin\beta & \cos\alpha \end{bmatrix} \begin{bmatrix} -C_D \\ C_Y \\ -C_L \end{bmatrix} \quad (2.40)$$

The complete aerodynamic polynomial model is presented below:

$$C_D = C_{D_0} + C_{D_\alpha} \alpha + C_{D_{\alpha^2}} \alpha^2 + C_{D_{\alpha^3}} \alpha^3 + C_{D_{\alpha^4}} \alpha^4 + C_{D_{\alpha^5}} \alpha^5 + C_{D_{\delta_{ee}}} \delta_{ee} + C_{D_{\delta_{ee}^2}} \delta_{ee}^2 + C_{D_{\delta_{ee}^3}} \delta_{ee}^3 + C_{D_{\delta_{ee}^4}} \delta_{ee}^4 + C_{D_{\delta_{re}}} \delta_{re} + C_{D_{\delta_{re}^2}} \delta_{re}^2 \quad (2.41)$$

$$C_Y = C_{Y_0} + C_{Y_\beta} \beta + C_{Y_{\hat{p}}} \hat{p} + C_{Y_{\hat{r}}} \hat{r} + C_{Y_{\delta_{rr}}} \delta_{rr} + C_{Y_{\delta_{rr}^2}} \delta_{rr}^2 + C_{Y_{\delta_{rr}^3}} \delta_{rr}^3 + C_{Y_{\delta_{rr}^4}} \delta_{rr}^4 \quad (2.42)$$

$$C_L = C_{L_0} + C_{L_\alpha} \alpha + C_{L_{\alpha^2}} \alpha^2 + C_{L_{\alpha^3}} \alpha^3 + C_{L_{\alpha^4}} \alpha^4 + C_{L_{\alpha^5}} \alpha^5 + C_{L_{\hat{q}}} \hat{q} + C_{L_{\delta_{ee}}} \delta_{ee} + C_{L_{\delta_{ee}^2}} \delta_{ee}^2 + C_{L_{\delta_{ee}^3}} \delta_{ee}^3 + C_{L_{\delta_{ee}^4}} \delta_{ee}^4 + C_{L_{\delta_{re}}} \delta_{re} + C_{L_{\delta_{re}^2}} \delta_{re}^2 + C_{L_{\delta_{re}^3}} \delta_{re}^3 + C_{L_{\delta_{re}^4}} \delta_{re}^4 \quad (2.43)$$

$$C_l = C_{l_0} + C_{l_\beta} \beta + C_{l_{\hat{p}}} \hat{p} + C_{l_{\hat{r}}} \hat{r} + C_{l_{\delta_{er}}} \delta_{er} + C_{l_{\delta_{er}^2}} \delta_{er}^2 + C_{l_{\delta_{er}^3}} \delta_{er}^3 + C_{l_{\delta_{er}^4}} \delta_{er}^4 + C_{l_{\delta_{rr}}} \delta_{rr} + C_{l_{\delta_{rr}^2}} \delta_{rr}^2 + C_{l_{\delta_{rr}^3}} \delta_{rr}^3 + C_{l_{\delta_{rr}^4}} \delta_{rr}^4 \quad (2.44)$$

$$C_m = C_{m_0} + C_{m_\alpha} \alpha + C_{m_{\alpha^2}} \alpha^2 + C_{m_{\alpha^3}} \alpha^3 + C_{m_{\alpha^4}} \alpha^4 + C_{m_{\alpha^5}} \alpha^5 + C_{m_{\hat{q}}} \hat{q} + C_{m_{\delta_{ee}}} \delta_{ee} + C_{m_{\delta_{ee}^2}} \delta_{ee}^2 + C_{m_{\delta_{ee}^3}} \delta_{ee}^3 + C_{m_{\delta_{ee}^4}} \delta_{ee}^4 + C_{m_{\delta_{ee}^5}} \delta_{ee}^5 + C_{m_{\delta_{re}}} \delta_{re} + C_{m_{\delta_{re}^2}} \delta_{re}^2 + C_{m_{\delta_{re}^3}} \delta_{re}^3 + C_{m_{\delta_{re}^4}} \delta_{re}^4 \quad (2.45)$$

$$\begin{aligned}
 C_n = & C_{n_0} + C_{n_\beta} \beta + C_{n_{\hat{p}}} \hat{p} + C_{n_{\hat{r}}} \hat{r} + C_{n_{\delta_{er}}} \delta_{er} + C_{n_{\delta_{er}^2}} \delta_{er}^2 + C_{n_{\delta_{er}^3}} \delta_{er}^3 + C_{n_{\delta_{er}^4}} \delta_{er}^4 \\
 & + C_{n_{\delta_{rr}}} \delta_{rr} + C_{n_{\delta_{rr}^2}} \delta_{rr}^2 + C_{n_{\delta_{rr}^3}} \delta_{rr}^3 + C_{n_{\delta_{rr}^4}} \delta_{rr}^4 + C_{n_{\delta_{rr}^5}} \delta_{rr}^5
 \end{aligned} \quad (2.46)$$

The values for the various coefficients can be computed from a combination of CFD analysis and the procedures described in Ref. [31].

An important phenomenon that influences the aircraft's aerodynamics is the ground effect. Ground effect is the phenomenon caused by the presence of a boundary below and near a wing. The boundary, which in this case is the ground, alters the flow of the air around the wing, not allowing it to expand as it would in free air. The result is an increase in lift and a reduction in the induced drag. The additional lift is due to an increase in static pressure under the wing [32]. The ground effect is mostly essential for take-off and landing, when the aircraft flies at heights lower than its wingspan length.

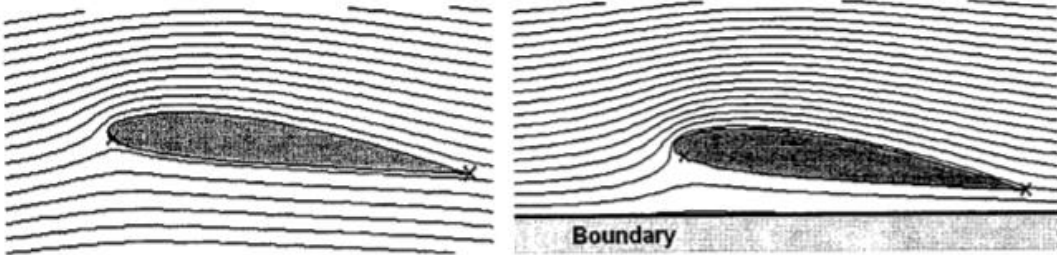


Figure 2.14. Flow Field inside (right) and outside (left) of the Ground Effect Regime [32]

Propulsion Forces and Moments

All forms of aircraft propulsion develop thrust by pushing air backwards. In the case of a propeller aircraft, as is the case at hand, the propulsive force is exerted directly on the aircraft by the propeller. The propeller is a rotating airfoil that generates thrust much as a wing generates lift [33]. Assuming the engine's power is given, thrust can be calculated from the following equation:

$$T = \frac{P \eta_p}{V} \quad (2.47)$$

where P is the engine's power, η_p is the propeller's efficiency and V is the aircraft's velocity relative to the air mass. The propeller's efficiency varies depending on the mission phase, for a fixed-pitch propeller. However, using a variable pitch propeller, an almost constant, optimum efficiency can be achieved. A variable-pitch propeller is a type of propeller with

blades that can be rotated around their long axis to change the blade pitch. Such propellers are used in propeller-driven aircraft to maintain engine RPM at any flight condition. In the case of zero velocity, since eq. 2.47 would result to an infinite value of thrust, another equation is used, giving the static thrust:

$$T = 0.9P^{\frac{2}{3}}(2\rho A_{swept})^{\frac{1}{3}} = 0.9P^{\frac{2}{3}}(2\rho(\pi(r_{tip}^2 - r_{root}^2)))^{\frac{1}{3}} \quad (2.48)$$

where A is the area swept out by the propeller, r_{tip} is the blade tip radius and r_{root} is the blade root radius.

There is a variation in thrust produced by the propeller with altitude, due to the variation in air density. Assuming the given engine's power corresponds to sea level conditions, a correction must be applied to compute thrust at a different altitude:

$$T = P_{SL} \left(A_P \frac{\rho}{\rho_{SL}} - B_P \right) \frac{\eta_p}{V} \quad (2.49)$$

where P_{SL} is power at sea level, ρ_{SL} is air density at sea level and A_P and B_P are constants with the typical values of:

$$A_P = 1.132, \quad B_P = A_P - 1 = 0.132$$

The thrust axis for an aircraft is the line of action of the total thrust at any instant. It depends on the location, number, and characteristics of the engines. The direction of thrust usually lies on the plane of symmetry but may not align with the x_B axis. The symbol ϵ_T will be used to denote the angle between T and x_B .

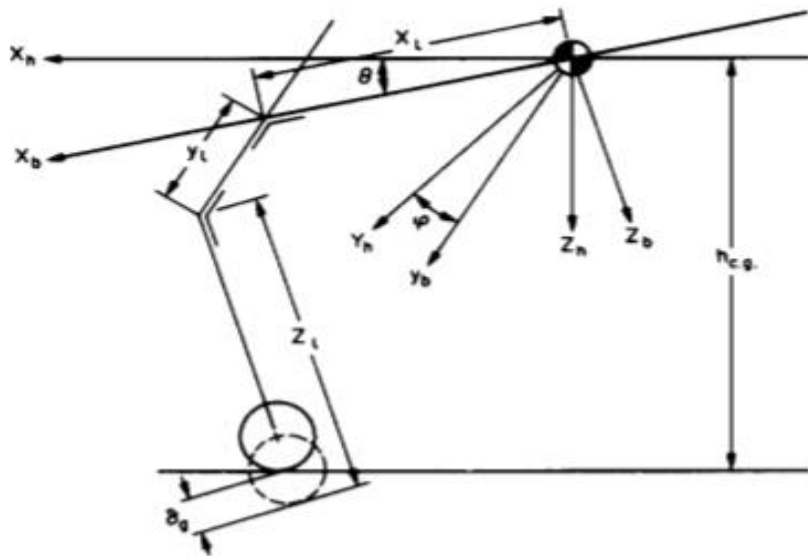
Landing Gear Forces and Moments

In order for take-off and landing to be simulated, the forces and moments produced by the landing gear must be included in the equations of motion. The landing gear forces, as stated in Ref. [28], are split into:

- the vertical force
- the longitudinal force

The lateral force is neglected, as its effect is of no great concern in the case at hand. The vertical force is a function of the tyre deflection (δ_t), the strut deflection (δ_s) and the gear rate of deflection ($\dot{\delta}_g$), where the gear deflection is:

$$\delta_g = \delta_t + \delta_s \quad (2.50)$$



$$h_{cg} = (z_l - \delta_g) \cos \theta \cos \varphi + y_l \sin \varphi - x_l \sin \theta$$

$$\delta_g = z_l - \frac{1}{\cos \theta \cos \varphi} (h_{cg} + x_l \sin \theta - y_l \sin \varphi)$$

assume that: $\cos \theta \cos \varphi = 1$

$$\delta_g = z_l - h_{cg} - x_l \sin \theta + y_l \sin \varphi$$

Figure 2.15. Computation of δ_g [28]

The total deflection and deflection rate of each landing gear are calculated as follows (**Figure 2.15**):

$$\delta_g = z_g - h_{CG} - x_g \sin \theta + y_g \sin \varphi \quad (2.51)$$

$$\dot{\delta}_g = -\dot{h}_{CG} - x_g \dot{\theta} \cos \theta + y_g \dot{\varphi} \cos \varphi \quad (2.52)$$

where x_g , y_g and z_g are the gear's coordinates measured from the AC. Three conditions are possible, depending on the value of δ_g :

1. $\delta_g \leq 0$

The landing gear makes no ground contact, so:

$$F_V = 0$$

$$\delta_g = 0$$

2. $\delta_g > 0$ and $\delta_s = 0$

The landing gear makes ground contact, but the vertical force does not exceed the preload of the strut P ($F_V \leq P$), so:

$$\delta_g = \delta_t \quad (2.53)$$

$$F_V = P \frac{\delta_g}{\delta_{t_P}} \quad (2.54)$$

where δ_{t_P} is the deflection of the tyre for $F_V = P$

3. $\delta_g > 0$ and $\delta_s > 0$

In this case the vertical force exceeds the preload of the strut. The strut damping force F_D is considered to be linear with the gear deflection rate. So, in this case:

$$F_D = c_v \dot{\delta}_g \quad (2.55)$$

$$F_V = P \frac{\delta_{g_{max}}}{\delta_{g_{max}} + \delta_{t_P} - \delta_g} + F_D \quad (2.56)$$

where $\delta_{g_{max}}$ is the maximum deflection of the gear and c_v is the gear's damping constant.

The longitudinal force, which lies upon the x_H axis, is a friction force. It is a function of the brake pedal deflection (δ_{bp}), the vertical force (F_V) on each gear, the braking friction coefficient (μ_B) and the rolling friction coefficient (μ_{roll}). The braking friction coefficient depends on the brake pedal deflection:

$$\mu_B = \mu_{B_{max}} \frac{\delta_{bp}}{\delta_{bp_{max}}} \quad (2.57)$$

where $\mu_{B_{max}}$ is the maximum braking friction coefficient and $\delta_{bp_{max}}$ is the maximum brake pedal deflection. The total friction coefficient on each landing gear is:

$$\mu = \mu_B + \mu_{roll} \quad (2.58)$$

Finally, the longitudinal force on each gear is:

$$F_\mu = F_V \mu \quad (2.59)$$

Typical values for the rolling friction coefficient can be found in literature, such as Ref. [33].

Since the forces are calculated in the local-horizontal reference frame, they have to be transformed to body axes, in order to be added to the external forces and moments acting on the aircraft:

$$\begin{bmatrix} F_X \\ F_Y \\ F_Z \end{bmatrix} = \begin{bmatrix} -\cos\theta & 0 & -\sin\theta \\ -\sin\theta\sin\varphi & -\cos\varphi & -\cos\theta\sin\varphi \\ -\sin\theta\cos\varphi & \sin\varphi & -\cos\theta\cos\varphi \end{bmatrix} \begin{bmatrix} F_\mu \\ 0 \\ F_V \end{bmatrix} \quad (2.60)$$

The external moments due to landing gear are:

$$\begin{bmatrix} L_{LG} \\ M_{LG} \\ N_{LG} \end{bmatrix} = \sum \begin{bmatrix} 0 & -(z_g - \delta_g) & y_g \\ z_g - \delta_g & 0 & x_g \\ -y_g & x_g & 0 \end{bmatrix} \begin{bmatrix} F_X \\ F_Y \\ F_Z \end{bmatrix} \quad (2.61)$$

The total external forces and moments due to landing gear are:

$$X_{LG} = (F_X)_{left} + (F_X)_{right} + (F_X)_{front} \quad (2.62)$$

$$Y_{LG} = (F_Y)_{left} + (F_Y)_{right} + (F_Y)_{front} \quad (2.63)$$

$$Z_{LG} = (F_Z)_{left} + (F_Z)_{right} + (F_Z)_{front} \quad (2.64)$$

$$L_{LG} = (L_{LG})_{left} + (L_{LG})_{right} + (L_{LG})_{front} \quad (2.65)$$

$$M_{LG} = (M_{LG})_{left} + (M_{LG})_{right} + (M_{LG})_{front} \quad (2.66)$$

$$N_{LG} = (N_{LG})_{left} + (N_{LG})_{right} + (N_{LG})_{front} \quad (2.67)$$

Atmosphere and Wind Effect

Another crucial parameter affecting the aircraft's behavior is the atmosphere around it. Air density and wind velocity are the most important atmospheric conditions. The International Standard Atmosphere (ISA) model gives the average temperature, pressure, and density (over time) at any point in the atmosphere, as a function of altitude [19]. For altitudes less than 36000 ft, the average values as a function of altitude (which is an empirical formula) are:

$$\bar{T} = 518.69 \text{ } ^\circ R - (0.003566 \text{ } ^\circ R/ft)h \quad (2.68)$$

$$\bar{p} = (2116.8 \text{ } psf) \left(\frac{\bar{T}}{518.69 \text{ } ^\circ R} \right)^{5.262} \quad (2.69)$$

$$\bar{\rho} = \frac{\bar{p}}{R\bar{T}} \quad (2.70)$$

The equations above only give the average conditions at a point in the atmosphere, hence the overbars. Depending on the weather, the temperature and pressure could be different than the average. Many flight simulators have meteorological models to simulate these fluctuations.

As for wind velocity, it represents the air mass velocity relative to the ground. The relationship between ground velocity, airspeed and wind velocity is given by:

$$V_g = V + V_w \quad (2.71)$$

where V_g is the ground velocity, V is the airspeed and V_w is the wind velocity. The total wind velocity vector is constituted by the constant vector (V_{ws}), representing a steady ambient wind, and a stochastic component (V_{wg}), that represents wind gusts and other atmospheric disturbances such as wind turbulence and wind shear:

$$V_w = V_{ws} + V_{wg} \quad (2.72)$$

The gust portion of the wind can be written in terms of its body-frame components as:

$$V_{wg} = \begin{bmatrix} u_{wg} \\ v_{wg} \\ w_{wg} \end{bmatrix}$$

The application of turbulence and wind shear in piloted flight simulation may be used for several purposes, such as to serve as a general distracting element to increase the pilot's overall workload or to represent the actual disturbances acting on the aircraft in real flight, in

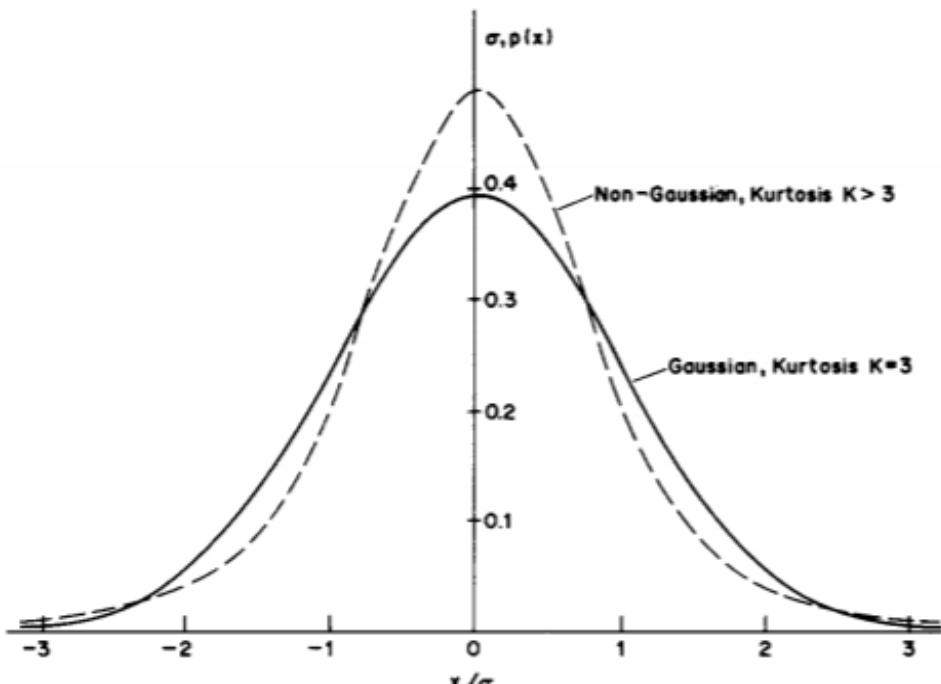


Figure 2.16. The Gaussian and a possible non-Gaussian Distribution Function [28]

order to investigate aircraft performance. In the first application, simple filtering of Gaussian [34] white noise is a possible solution, as the accuracy requirements on the simulated turbulence are rather low. However, as greater reliance is placed on the flight simulator, the accurate reproduction of turbulence and wind shear becomes more important. Atmospheric turbulence is, in contrast with other elements of flight simulation like aircraft motion due to control inputs, not deterministic but stochastic by nature. Thus, the mathematical model describing the turbulence velocity components is based on statistical methods like power spectra and probability distributions [28]. Measurements of actual turbulence velocities have shown that atmospheric turbulence is a non-Gaussian process, which poses a serious problem on its simulation. The so-called 'patchy' characteristics of atmospheric turbulence exhibit local regions of higher energy concentrations separated by relatively calm periods, which cause deviations from the Gaussian distribution function. The non-Gaussian characteristics are described by two parameters: 'Kurtosis', K, and a 'patchiness parameter', R. **Figure 2.16** shows the Gaussian and a possible non-Gaussian distribution function, which are distinguished by the value of the Kurtosis, K, defined as:

$$K = \frac{m_4}{m_2^2} \quad (2.73)$$

where m_2 is the second order central moment, known as the variance σ^2 , and m_4 is the fourth order central moment, which takes the value of $3\sigma^4$ (resulting in $K = 3$) in a Gaussian process. The second parameter, which describes the 'patchiness' in atmospheric turbulence, is the parameter R. The patchy characteristics may cause sudden large deviations in aircraft attitude, which demand pilot corrective actions. The complete patchy turbulence simulation is obtained, using five turbulence velocities as inputs to the mathematical model of the airplane. The generation of each of these turbulence velocities consists of three independent white noise sources, feeding three linear filters, as shown in **Figure 2.18**. The filter outputs $a(t)$, $b(t)$ and $c(t)$ are mixed such as to obtain the desired patchy characteristic of the turbulence velocity. The longitudinal turbulence velocity $u_{g\text{sym}}$ and vertical velocity $w_{g\text{sym}}$ determine the symmetric airplane motions due to atmospheric turbulence. The lateral

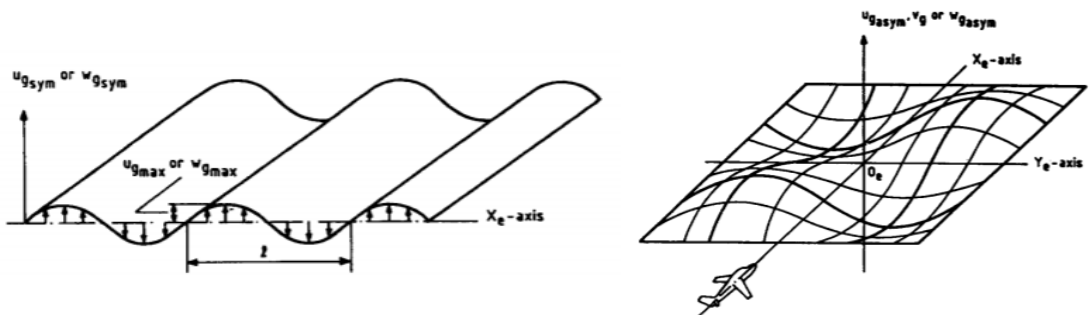


Figure 2.17. Representation of the Wind Turbulence Field [28]

turbulence velocity v_g and the turbulence velocities $u_{g\text{asym}}$, and $w_{g\text{asym}}$ determine the asymmetric airplane motions due to atmospheric turbulence.

The actual generation of each of these five stochastic turbulence velocities employs the product of two independent Gaussian processes, shaped by linear filters to acquire the power spectra of the turbulence velocities, according to Dryden [35]. Turbulence velocities as a result of the multiplication, however, are more severely non-Gaussian than indicated by experimental data. Therefore, a third independent Gaussian process, linearly filtered also to obtain the Dryden power spectrum, is added to create a wide variety of possible patchy characteristics. The mathematical formulation for the generation of the five turbulence

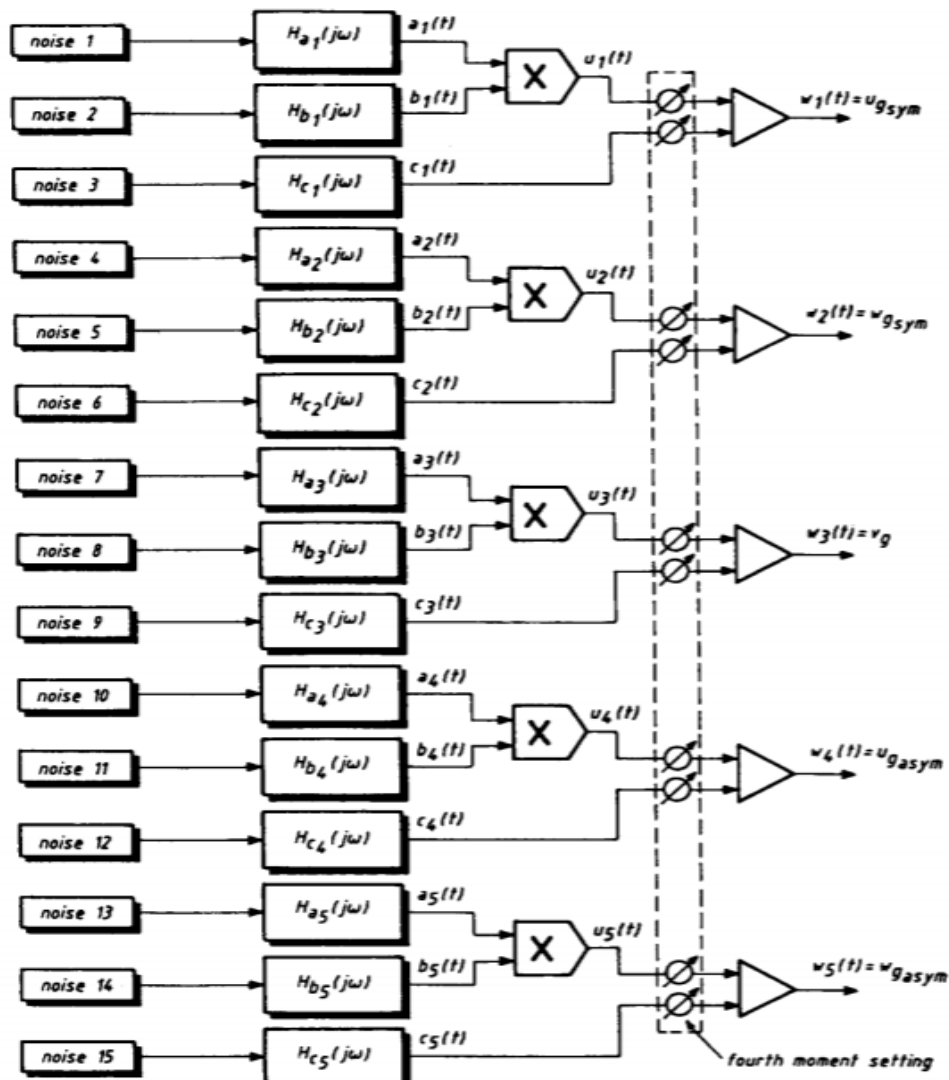


Figure 2.18. The Generation of "Patchy" Atmospheric Turbulence for Real-Time Simulation [28]

velocities can be found in Ref. [28]. It will not be described here since the simulator studied uses the fixed Simulink blocks for the environmental model, as shown in the Tools and Methods chapter.

During an actual approach to landing of an airplane there is usually some wind in the lower atmosphere. The wind shear phenomenon can be described as a variation of the wind velocity with altitude. The combined effect of two atmospheric disturbance components represents the total wind shear:

- The variation of the mean or steady-state wind velocity with altitude, as determined from the wind profile and the change in wind direction with altitude.
- The resulting stochastic component of the prevailing patchy atmospheric turbulence as described above.

The wind velocity vector magnitude, or wind speed, is modelled by expressions matched to experimental data. In unstable atmospheric conditions a logarithmic law seems to fit the experimental data quite well. Employing the notation as given in Ref. [28], for standard atmospheric stability conditions and flat terrain:

$$u(z) = \frac{u^*}{k} \ln \left(\frac{z}{z_0} \right) \quad (2.74)$$

where:

- $u(z)$ = wind speed at height z
- u^* = friction velocity = 0.47 m/s, being constant up to a height z of at least 100 m
- k = Von Karman constant = 0.4
- z_0 = aerodynamic roughness height = 0.1 m

In order to bring the wind shear and turbulence models to a common basis, the wind speed is expressed as a function of the wind velocity at a reference height of 9.15 m (30 ft). The following expression for the wind speed V_w is:

$$V_w = V_{w_{9.15}} (0.43 \log_{10} h + 0.572) \quad 0 < h < 300 \text{ m} \quad (2.75)$$

$$V_w = 1.637 V_{w_{9.15}} \quad h \geq 300 \text{ m} \quad (2.76)$$

where:

- V_w [m/s] = wind speed at height h
- $V_{w_{9.15}}$ [m/s] = wind speed at 9.15 m altitude
- h [m] = altitude above the terrain

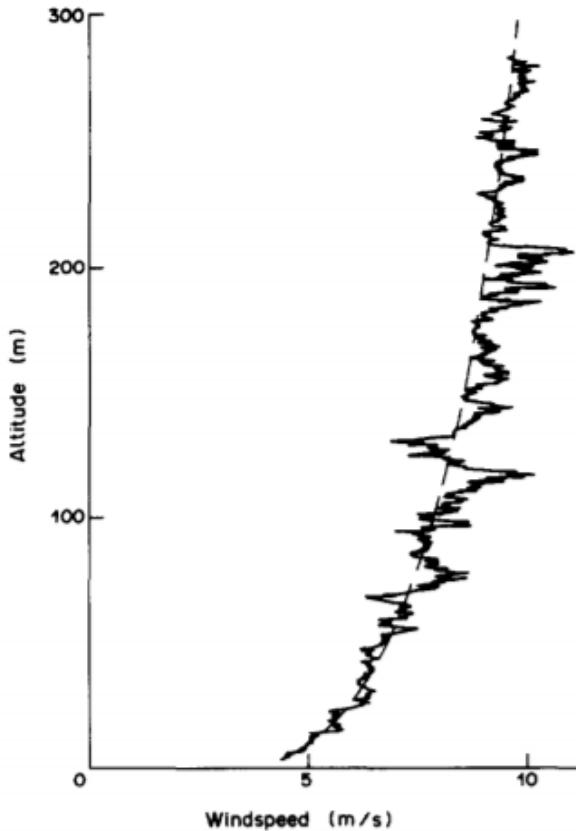


Figure 2.19. Superposition of the Wind Profile and Turbulence [28]

Turbulence Theory

Turbulent flows are highly complex, consisting of multiple length and time scales, unsteadiness, randomness and three-dimensionality [36]. The most accepted theory of turbulence is based on the ‘energy cascade’ concept developed by Kolmogorov [37], [38]. According to his theory, turbulence is composed of eddies of different sizes with each one possessing a certain amount of energy that depends on its dimension. The larger eddies break up transferring their energy to smaller size eddies in a chain process by which the smaller newly formed eddies undergo similar breakup processes and transfer their energy to even smaller eddies [39]. This process continues until the smallest possible eddy size is reached. The smallest eddies are of scales at which molecular viscosity is effective at dissipating the turbulent kinetic energy as heat. As a result, numerical methods, known as CFD, must be used to solve turbulent flows. These methods discretize the flow domain into smaller cells, which are then resolved by solving the flow equations for each cell. Then, by using averaging and approximation techniques over each of the cells, scalar and vector fields are computed. The three main categories of CFD, which can be used to compute the flow field for a given problem

are: direct numerical simulation (DNS), large eddy simulation (LES) and Reynold-averaged Navier-Stokes (RANS) methods. DNS is the most accurate because Navier-Stokes equations are numerically solved without the use of any turbulence model and all the spatial scales of the turbulence must be resolved in the computational mesh, including the smallest dissipative scales (Kolmogorov scales). However, due to its prohibitive computational cost, it cannot be employed to solve industrial problems and it is viewed mainly as a research tool. LES is somewhat of a mixture of DNS and RANS, because the large-scale structures are computed and the smaller scales are modeled. The principal idea behind LES is to reduce the computational cost by ignoring the smallest length scales, which are the most computationally expensive to resolve, while still giving an accurate and detailed solution of the flow field. RANS is based on time-averaged equations and is the least computationally intensive method, however, it is the least detailed and exact method. The Reynolds stresses are fully approximated by turbulence models. From these descriptions, it is clear that there is a trade-off between computational intensity and level of detail and accuracy. RANS methods are much faster, which makes them ideal for design iteration and optimization, although they give heavily approximated solutions. In any RANS method the most difficult issue to deal with is the closure problem. This problem arises because the number of the unknowns is larger than the number of the equations. One of the problems with the above concept of Reynolds decomposition and averaging is that it introduces additional variables (Reynolds stresses). Reynolds stress is a property of the flow; hence, it is dependent on the flow variables themselves. For this reason, it changes from flow to flow and no general constitutive relations are available. Boussinesq suggested describing Reynolds stress in a similar way viscous stress is described, introducing the turbulent viscosity. However, these models used a constant value for turbulent viscosity and did not give accurate results. Later, Prandtl introduced the mixing length concept analogous to the mean free path of the molecules in gas. He also prescribed an algebraic expression relating turbulent viscosity to the mixing length, producing the algebraic or zero-equation models. Zero-equation refers to the fact that no additional transport equations besides to energy, mass and momentum equations are needed. Moreover, he introduced a concept of turbulent viscosity as a function of turbulent kinetic energy. This concept is physically more realistic and, due to the fact that he used one additional transport equation to model turbulent kinetic energy, models based on this concept are called one equation models. Both of the previous models are incomplete. The complete models do not need knowledge of the flow in advance, except for the initial and boundary conditions. The first model was introduced by Kolmogorov who connected the turbulent kinetic energy, k , with the rate of energy dissipation, ω and related the missing information of length and time scales to these quantities. These models are called two-equation models and are the most popular in terms of usage in the simulation of industrial applications. They offer a good compromise between numerical effort and computational accuracy. Practically, turbulence models produce a 'closed' system of equations, where there is an equality of equations and unknowns, by providing approximations for the unknown Reynolds stresses. Each of the models has advantages and disadvantages depending on the nature of the flow being studied, so there are no set procedures as to which turbulence model to use for a specific flow, only guidelines based on experience.

Turbulence Modeling

The modeling of turbulent flows using RANS methods begins with the continuity equation (incompressible) and the Navier-Stokes momentum equations for the mean flow.

$$\frac{\partial U_i}{\partial x_i} = 0 \quad (2.77)$$

$$\rho \left(\frac{\partial U_i}{\partial t} + U_j \frac{\partial U_i}{\partial x_j} \right) = - \frac{\partial p}{\partial x_i} + \mu \frac{\partial^2 U_i}{\partial x_i^2} - \rho g_i \quad (2.78)$$

Through a series of arithmetic operations, the resulting Reynolds-averaged Navier-Stokes momentum equations are obtained, with a new term introduced, known as the Reynolds stress tensor ($\rho \bar{u}_i \bar{u}_j$).

$$\rho \left(\frac{\partial U_i}{\partial t} + U_j \frac{\partial U_i}{\partial x_j} \right) = - \frac{\partial p}{\partial x_i} + \frac{\partial}{\partial x_j} \left(\mu \left(\frac{\partial U_i}{\partial x_j} + \frac{\partial U_j}{\partial x_i} \right) - \rho \bar{u}_i \bar{u}_j \right) \quad (2.79)$$

The Reynolds stress tensor has six components and therefore six unknowns have been introduced due to the Reynolds averaging completed on the Navier-Stokes equations. To resolve this issue, the following equation needs to be derived to compute the Reynolds stresses.

$$\overline{u_j N(U_i) + u_i N(U_j)} = 0 \quad (2.80)$$

After algebraic manipulation and simplifications, the resulting Reynolds stress equation is:

$$\begin{aligned} \frac{\partial \bar{u}_i \bar{u}_j}{\partial t} + \frac{\partial}{\partial x_k} (U_k \rho \bar{u}_i \bar{u}_j) &= -\rho \bar{u}_i \bar{u}_j \frac{\partial U_j}{\partial x_k} - \rho \bar{u}_j \bar{u}_k \frac{\partial U_i}{\partial x_k} + \varepsilon_{ij} - \Phi_{ij} \\ &\quad + \frac{\partial}{\partial x_k} \left[\nu \frac{\partial \bar{u}_i \bar{u}_j}{\partial x_k} + C_{ijk} \right] \end{aligned} \quad (2.81)$$

where: $\varepsilon_{ij} = 2\nu \overline{\frac{\partial u_i}{\partial x_k} \frac{\partial u_j}{\partial x_k}}$, $\Phi_{ij} = \overline{\frac{p'}{\rho} \left(\frac{\partial u_i}{\partial x_j} + \frac{\partial u_j}{\partial x_i} \right)}$ and $\rho C_{ijk} = \rho \bar{u}_i \bar{u}_j \bar{u}_k + \overline{p' u_i} \delta_{jk} + \overline{p' u_j} \delta_{ik}$

The turbulent kinetic energy is defined as:

$$k = \frac{1}{2} \overline{u_i u_i} \quad (2.82)$$

The differential equation for k which is used in common turbulence models is:

$$\frac{\partial k}{\partial t} + U_j \frac{\partial k}{\partial x_j} = \overline{u_i u_j} \frac{\partial U_i}{\partial x_j} - \nu \overline{\frac{\partial u_i}{\partial x_k} \frac{\partial u_j}{\partial x_k}} + \frac{\partial}{\partial x_j} \left(\nu \frac{\partial k}{\partial x_j} - \frac{1}{2} \overline{u_i u_i u_j} - \frac{1}{\rho} \overline{p' u_j} \right) \quad (2.83)$$

From this point onward, all of the turbulence models described utilize the k equation, however, approximations and assumptions are implemented to model the unknown terms. Generally, terms that require modeling are those which contain any fluctuating components. At each level of manipulation and averaging, new unknowns are introduced, which must be modeled to close the system of equations and obtain a numerical solution.

Two-equation eddy viscosity models (EVM)

By definition, two-equation models include two extra transport equations to represent the turbulent properties of the flow. This allows a two-equation model to account for history effects like convection and diffusion of turbulent energy. Modern two-equation models are based on the Boussinesq approximation, which approximates the Reynolds stresses as proportional to the mean velocity gradients:

$$-\rho \overline{u_i u_j} = \mu_t \left(\frac{\partial U_i}{\partial x_j} + \frac{\partial U_j}{\partial x_i} \right) - \frac{2}{3} \delta_{ij} \left(\rho k + \mu_t \frac{\partial U_k}{\partial x_k} \right) \quad (2.84)$$

where u is the fluctuating turbulent velocity, U is the mean velocity, k is the turbulent kinetic energy and μ_t is the eddy viscosity. For incompressible flows, $\partial U_k / \partial x_k = 0$. In two-equation models, the eddy viscosity is calculated from the solution of the two additional differential equations, one of which is often the turbulence kinetic energy, k . Three prominent eddy viscosity models available in most commercial CFD suites are the $k - \varepsilon$, $k - \omega$ and SST models, presented in the following section.

The $k - \varepsilon$ model

The $k - \varepsilon$ model is one of the most commonly used models and is useful for a wide range of turbulent flow problems. The eddy viscosity, μ_t , in the model is obtained from the turbulent kinetic energy, k , and the turbulent dissipation rate, ε (dissipation of velocity fluctuations). k and ε are obtained by solving transport equations 2.68 and 2.69.

$$\mu_t = C_\mu \rho \frac{k^2}{\varepsilon} \quad (2.85)$$

$$\frac{\partial(\rho k)}{\partial t} + \frac{\partial}{\partial x_j} (\rho U_j k) = \frac{\partial}{\partial x_j} \left[\left(\mu + \frac{\mu_t}{\sigma_k} \right) \frac{\partial k}{\partial x_j} \right] + P_k - \rho \varepsilon + P_{kb} \quad (2.86)$$

$$\frac{\partial(\rho \varepsilon)}{\partial t} + \frac{\partial}{\partial x_j} (\rho U_j \varepsilon) = \frac{\partial}{\partial x_j} \left[\left(\mu + \frac{\mu_t}{\sigma_\varepsilon} \right) \frac{\partial \varepsilon}{\partial x_j} \right] + \frac{\varepsilon}{k} (C_{\varepsilon 1} P_k - C_{\varepsilon 2} \rho \varepsilon + C_{\varepsilon 1} P_{\varepsilon b}) \quad (2.87)$$

where $C_{\varepsilon 1}$, $C_{\varepsilon 2}$, σ_k and σ_ε are constants. P_{kb} and $P_{\varepsilon b}$ represent the influence of the buoyancy forces. P_k is the turbulence production due to viscous forces, which is modeled using the following equation:

$$P_k = \mu_t \left(\frac{\partial U_i}{\partial x_j} + \frac{\partial U_j}{\partial x_i} \right) \frac{\partial U_i}{\partial x_j} - \frac{2}{3} \frac{\partial U_k}{\partial x_k} \left(3\mu_t \frac{\partial U_k}{\partial x_k} + \rho k \right) \quad (2.88)$$

As mentioned before, for incompressible flows, $\partial U_k / \partial x_k$ is small and the second term on the right side of the equation does not contribute significantly to the production. In these equations, the following constants derived by Launder and Spalding [40] are used:

$$C_\mu = 0.09, C_{\varepsilon 1} = 1.44, C_{\varepsilon 2} = 1.92, \sigma_k = 1.0, \sigma_\varepsilon = 1.3$$

The Wilcox $k-\omega$ model

The $k - \omega$ model is another commonly used two-equation turbulence model that was developed by Wilcox [41] and solves two transport equations, one for turbulent kinetic energy, k , and one for turbulent frequency, ω (specific dissipation rate). The specific dissipation rate, ω , is defined by the ratio ε/k . The k and ω transport equations are given by the equations 2.72 and 2.73, respectively.

$$\mu_t = \rho \frac{k}{\omega} \quad (2.89)$$

$$\frac{\partial(\rho k)}{\partial t} + \frac{\partial}{\partial x_j} (\rho U_j k) = \frac{\partial}{\partial x_j} \left[\left(\mu + \frac{\mu_t}{\sigma_k} \right) \frac{\partial k}{\partial x_j} \right] + P_k - \beta' \rho k \omega + P_{kb} \quad (2.90)$$

$$\frac{\partial(\rho \omega)}{\partial t} + \frac{\partial}{\partial x_j} (\rho U_j \omega) = \frac{\partial}{\partial x_j} \left[\left(\mu + \frac{\mu_t}{\sigma_\omega} \right) \frac{\partial \omega}{\partial x_j} \right] + \alpha \frac{\omega}{k} P_k - \beta \rho \omega^2 + P_{\omega b} \quad (2.91)$$

where P_k is the production rate of turbulence, which is calculated as in the $k - \varepsilon$ model.

The constants in these model equations are [41]:

$$\beta' = 0.09, \alpha = \frac{5}{9}, \beta = 0.075, \sigma_k = 2, \sigma_\omega = 2$$

The Baseline (BSL) $k-\omega$ model

The main problem with the Wilcox model is its well-known strong sensitivity to freestream conditions [42]. Depending on the value specified for ω at the inlet, a significant variation in the results of the model can be obtained. This is undesirable and in order to solve the problem, a blending between the $k - \omega$ model near the surface and the $k - \varepsilon$ model in the outer region was developed by Menter [43]. It consists of a transformation of the $k - \varepsilon$ model to a $k - \omega$ formulation and a subsequent addition of the corresponding equations.

Wilcox model:

$$\frac{\partial(\rho k)}{\partial t} + \frac{\partial}{\partial x_j} (\rho U_j k) = \frac{\partial}{\partial x_j} \left[\left(\mu + \frac{\mu_t}{\sigma_{k1}} \right) \frac{\partial k}{\partial x_j} \right] + P_k - \beta' \rho k \omega \quad (2.92)$$

$$\frac{\partial(\rho \omega)}{\partial t} + \frac{\partial}{\partial x_j} (\rho U_j \omega) = \frac{\partial}{\partial x_j} \left[\left(\mu + \frac{\mu_t}{\sigma_{\omega 1}} \right) \frac{\partial \omega}{\partial x_j} \right] + \alpha_1 \frac{\omega}{k} P_k - \beta_1 \rho \omega^2 \quad (2.93)$$

Transformed $k - \varepsilon$ model:

$$\frac{\partial(\rho k)}{\partial t} + \frac{\partial}{\partial x_j} (\rho U_j k) = \frac{\partial}{\partial x_j} \left[\left(\mu + \frac{\mu_t}{\sigma_{k2}} \right) \frac{\partial k}{\partial x_j} \right] + P_k - \beta' \rho k \omega \quad (2.94)$$

$$\begin{aligned} \frac{\partial(\rho \omega)}{\partial t} + \frac{\partial}{\partial x_j} (\rho U_j \omega) &= \frac{\partial}{\partial x_j} \left[\left(\mu + \frac{\mu_t}{\sigma_{\omega 2}} \right) \frac{\partial \omega}{\partial x_j} \right] + 2\rho \frac{1}{\sigma_{\omega 2} \omega} \frac{\partial k}{\partial x_j} \frac{\partial \omega}{\partial x_j} \\ &\quad + \alpha_2 \frac{\omega}{k} P_k - \beta_2 \rho \omega^2 \end{aligned} \quad (2.95)$$

Now the equations of the Wilcox model are multiplied by function F_1 , the transformed $k - \varepsilon$ equations by a function $1 - F_1$ and the corresponding k and ω equations are added to give the BSL model. Including buoyancy effects, the BSL model reads:

$$\frac{\partial(\rho k)}{\partial t} + \frac{\partial}{\partial x_j} (\rho U_j k) = \frac{\partial}{\partial x_j} \left[\left(\mu + \frac{\mu_t}{\sigma_{k3}} \right) \frac{\partial k}{\partial x_j} \right] + P_k - \beta' \rho k \omega + P_{kb} \quad (2.96)$$

$$\begin{aligned} \frac{\partial(\rho \omega)}{\partial t} + \frac{\partial}{\partial x_j} (\rho U_j \omega) &= \frac{\partial}{\partial x_j} \left[\left(\mu + \frac{\mu_t}{\sigma_{\omega 3}} \right) \frac{\partial \omega}{\partial x_j} \right] + (1 - F_1) 2\rho \frac{1}{\sigma_{\omega 2} \omega} \frac{\partial k}{\partial x_j} \frac{\partial \omega}{\partial x_j} \\ &\quad + \alpha_3 \frac{\omega}{k} P_k - \beta_3 \rho \omega^2 + P_{\omega b} \end{aligned} \quad (2.97)$$

The coefficients of the new model are a linear combination of the corresponding coefficients of the underlying models:

$$\Phi_3 = F_1 \Phi_1 + (1 - F_1) \Phi_2 \quad (2.98)$$

All coefficients are listed again:

$$\begin{aligned} \beta' &= 0.09, \alpha = \frac{5}{9}, \beta_1 = 0.075, \sigma_{k1} = 2, \sigma_{\omega 1} = 2, \sigma_{k2} = 1.0, \\ \sigma_{\omega 2} &= \frac{1}{0.856}, \alpha_2 = 0.44, \beta_2 = 0.0828 \end{aligned}$$

The Shear Stress Transport (SST) Model

The $k - \omega$ based SST model accounts for the transport of the turbulent shear stress and gives highly accurate predictions of the onset and the amount of flow separation under adverse pressure gradients [44]. The BSL model combines the advantages of the Wilcox and the $k - \varepsilon$ model but still fails to properly predict the onset and amount of flow separation from smooth surfaces. This deficiency is discussed in detail by Menter [43] but primarily arises because these models, which do not account for the transport of the turbulent shear stress, overpredict the eddy viscosity. The proper transport behavior can be obtained by a limiter to the formulation of the eddy-viscosity:

$$\nu_t = \frac{a_1 k}{\max\left(a_1 \omega, \frac{\partial u}{\partial y} F_2\right)} \quad (2.99)$$

where $\nu_t = \mu_t / \rho$. Note that in the SST model, $\sigma_{k1} = 1.176$.

Blending Functions

The blending functions are critical to the success of the method. Their formulation is based on the distance to the nearest surface and the flow variables.

$$F_1 = \tanh(\arg_1^4) \quad (2.100)$$

$$\arg_1 = \min\left(\max\left(\frac{\sqrt{k}}{\beta' \omega y}, \frac{500\nu}{y^2 \omega}\right), \frac{4\rho k}{CD_{k\omega} \sigma_{\omega 2} y^2}\right) \quad (2.101)$$

where y is the distance to the nearest wall, ν is the kinematic viscosity and:

$$CD_{k\omega} = \max\left(2\rho \frac{1}{\sigma_{\omega 2} \omega} \frac{\partial k}{\partial x_j} \frac{\partial \omega}{\partial x_j}, 1.0 \times 10^{-10}\right) \quad (2.102)$$

$$F_2 = \tanh(\arg_2^2) \quad (2.103)$$

$$\arg_2 = \max\left(\frac{2\sqrt{k}}{\beta' \omega y}, \frac{500\nu}{y^2 \omega}\right) \quad (2.104)$$

The Reynolds Stress Turbulence Model (RSM)

As mentioned before, two-equation turbulence models ($k - \varepsilon$ and $k - \omega$ based models) offer good predictions of the characteristics and physics of most flows of industrial relevance. However, in flows where the turbulent transport or non-equilibrium effects are important, the eddy-viscosity assumption is no longer valid, and results of eddy viscosity models might be inaccurate [44]. Reynolds Stress models naturally include the effects of streamline

curvature, sudden changes in the strain rate, secondary flows or buoyancy compared to turbulence models using the eddy-viscosity approximation [44]. These models are based on transport equations for all components of the Reynolds stress tensor and the dissipation rate. These models do not use the eddy viscosity hypothesis but solve an equation for the transport of Reynolds stresses in the fluid. The exact production term and the inherent modeling of stress anisotropies theoretically make Reynolds stress models more suited to complex flows, however, practice shows that they are often not superior to two-equation models. The Reynolds averaged momentum equations for the mean velocity are:

$$\frac{\partial \rho U_i}{\partial t} + \frac{\partial}{\partial x_j} (\rho U_i U_j) - \frac{\partial}{\partial x_j} \left[\mu \left(\frac{\partial U_i}{\partial x_j} + \frac{\partial U_j}{\partial x_i} \right) \right] = - \frac{\partial p''}{\partial x_i} - \frac{\partial}{\partial x_j} (\rho \bar{u}_i \bar{u}_j) + S_{M_i} \quad (2.105)$$

where p'' is a modified pressure, S_{M_i} is the sum of body forces and the fluctuating Reynolds stress contribution is $\rho \bar{u}_i \bar{u}_j$. Unlike eddy viscosity models, the modified pressure has no turbulence contribution and is related to the static (thermodynamic) pressure by:

$$p'' = p + \frac{2}{3} \mu \frac{\partial U_k}{\partial x_j} \quad (2.106)$$

In the differential stress model, $\rho \bar{u}_i \bar{u}_j$ is made to satisfy a transport equation. A separate transport equation must be solved for each of the six Reynolds stress components of $\rho \bar{u}_i \bar{u}_j$. The differential equation Reynolds stress transport is:

$$\begin{aligned} \frac{\partial \rho \bar{u}_i \bar{u}_j}{\partial t} + \frac{\partial}{\partial x_j} (U_k \rho \bar{u}_i \bar{u}_j) - \frac{\partial}{\partial x_j} & \left(\left(\delta_{kl} \mu + \rho C_s \frac{k}{\varepsilon} \bar{u}_k \bar{u}_l \right) \frac{\partial \bar{u}_i \bar{u}_j}{\partial x_l} \right) \\ & = P_{ij} - \frac{2}{3} \delta_{ij} \rho \varepsilon + \Phi_{ij} + P_{ij,b} \end{aligned} \quad (2.107)$$

where, P_{ij} and $P_{ij,b}$ are shear and buoyancy turbulence production terms of the Reynolds stresses respectively, Φ_{ij} is the pressure-strain tensor, and C is a constant. Buoyancy turbulence terms $P_{ij,b}$ also take the buoyancy contribution in the pressure strain term into account and are controlled in the same way as for the $k - \omega$ and $k - \varepsilon$ model.

The Transition SST Model

The Transition SST model (also known as the $\gamma - Re_\theta$ model) is based on the coupling of the SST $k - \omega$ transport equations with two other transport equations, one for the intermittency and one for the transition onset criteria, in terms of momentum-thickness Reynolds number.

The transport equation for the intermittency γ is defined as:

$$\frac{\partial(\rho\gamma)}{\partial t} + \frac{\partial(\rho U_j \gamma)}{\partial x_j} = P_{\gamma 1} - E_{\gamma 1} + P_{\gamma 2} - E_{\gamma 2} + \frac{\partial}{\partial x_j} \left[\left(\mu + \frac{\mu_t}{\sigma_\gamma} \right) \frac{\partial \gamma}{\partial x_j} \right] \quad (2.108)$$

The transport equation for the transition momentum thickness Reynolds number $R\tilde{e}_{\theta_t}$ is

$$\frac{\partial(\rho R\tilde{e}_{\theta_t})}{\partial t} + \frac{\partial(\rho U_j R\tilde{e}_{\theta_t})}{\partial x_j} = P_{\theta_t} + \frac{\partial}{\partial x_j} \left[\sigma_{\theta_t} (\mu + \mu_t) \frac{\partial R\tilde{e}_{\theta_t}}{\partial x_j} \right] \quad (2.109)$$

Details about the variables and the various coefficients can be found in Ref. [44].

The transition model interacts with the SST turbulence model by modification of the k equation, as follows:

$$\frac{\partial(\rho k)}{\partial t} + \frac{\partial(\rho k u_i)}{\partial x_j} = \frac{\partial}{\partial x_j} \left(\Gamma_k \frac{\partial k}{\partial x_j} \right) + G_k^* - Y_k^* + S_k \quad (2.110)$$

where \tilde{G}_k and Y_k are the original production and destruction terms for the SST model.

In order to capture the laminar and transitional boundary layers correctly, the mesh must have a y^+ of approximately one.

The Spalart Allmaras Model (SA)

The Spalart-Allmaras model [45] is a one-equation model that solves a modeled transport equation for the kinematic eddy (turbulent) viscosity. The Spalart-Allmaras model was designed specifically for aerospace applications involving wall-bounded flows and seems to give good results for boundary layers subjected to adverse pressure gradients [44]. In its original form, the Spalart-Allmaras model is effectively a low-Reynolds number model, requiring the viscosity-affected region of the boundary layer to be properly resolved ($y^+ \sim 1$ meshes). Also, it should be ensured that the boundary layer is resolved with a minimum resolution of 10-15 cells. The transported variable in the Spalart-Allmaras model, $\tilde{\nu}$, is identical to the turbulent kinematic viscosity except in the near-wall (viscosity-affected) region. The transport equation for the modified turbulent viscosity $\tilde{\nu}$ is:

$$\frac{\partial}{\partial t} (\rho \tilde{\nu}) + \frac{\partial}{\partial x_i} (\rho \tilde{\nu} u_i) = G_{\tilde{\nu}} + \frac{1}{\sigma_{\tilde{\nu}}} \left[\frac{\partial}{\partial x_j} \left\{ (\mu + \rho \tilde{\nu}) \frac{\partial \tilde{\nu}}{\partial x_j} \right\} + C_{b2} \rho \left(\frac{\partial \tilde{\nu}}{\partial x_j} \right)^2 \right] - Y_{\tilde{\nu}} + S_{\tilde{\nu}} \quad (2.111)$$

Note that since the turbulence kinetic energy, k , is not calculated in the Spalart-Allmaras model, the last term in equation 2.66 is ignored when estimating the Reynolds stresses.

The turbulent viscosity, μ_t , is computed from $\mu_t = \rho \tilde{\nu} f_{v1}$

where the viscous damping function, f_{v1} , is given by $f_{v1} = \frac{\chi^3}{\chi^3 + C_{v1}^3}$ and $\chi \equiv \frac{\tilde{\nu}}{\nu}$. Details about the variables and the various coefficients can be found in Ref. [44].

Curvature Correction for the Spalart-Allmaras and Two-Equation Models

One drawback of the eddy-viscosity models is that these models are insensitive to streamline curvature and system rotation, which play a significant role in many turbulent flows of practical interest. A modification to the turbulence production term is available to sensitize the following standard eddy-viscosity models to the effects of streamline curvature and system for the above-mentioned turbulence models. Spalart and Shur [46] and Shur et al. [47] have derived a modification of the production term for the Spalart-Allmaras one-equation turbulence model to take streamline curvature and system rotation effects into account. Based on this work, a modification of the production term has been derived that helps sensitize the standard two-equation turbulence models to these effects [48]. The empirical function suggested by Spalart and Shur [46] to account for streamline curvature and system rotation effects is defined by

$$f_{rotation} = (1 + c_{r1}) \frac{2r^*}{1 + r^*} [1 - c_{r3} \tan^{-1}(c_{r2} \tilde{r})] - c_{r1} \quad (2.112)$$

Details about the variables and the various coefficients can be found in Ref. [44].

Leading-Edge Vortices

Delta wings are divided into slender and non-slender types depending on the swept angle. Generally, the non-slender type corresponds to the case of a sweep angle less than 65°. Research into the aerodynamics of non-slender or ‘low sweep’ delta wings is more limited than that available on slender delta wings. The flow structures over a non-slender wing differs substantially from those documented over the slender planforms at high angles of attack and Reynolds number. For delta wings undergoing a positive angle of attack, it is well known that, due to flow separation on the surface during flight, two rotating vortices in the opposite directions are created by the leading edge of the wing. Flow that was originally attached on the lower surface at modest angles of attack turns outward at severe turning and approaches the leading edge. These rotating vortices at the leading edges cause increased flow velocities, and as a result, according to Bernoulli theorem, low static pressure regions. This produces large suction forces near to the leading edge on the surface, which generates an additional lift commonly known as vortex lift. While a slender wing typically exhibits a coherent primary vortex generated by the rollup of the shear layer separating from each leading-edge, computational and experimental studies have demonstrated that a ‘dual’ primary vortex structure exists over non-slender wings at low incidence [49]. The typical features of the vortices developed on a delta wing are clearly dependent on the angle of attack of the wing. When α increases, the strength and size of the vortex increases. The inclination angle of the vortex path with respect to the wing surface increases linearly. For this reason, the plane containing the two vortex cores moves away from the wing surface. At a sufficiently high angle of attack, the vortices undergo a sudden expansion known as vortex breakdown. Once the

angle of attack is large enough for the vortex breakdown to have crossed the trailing edge, the wing experiences a substantial change in the local pressure field, producing a decrease in the lift curve slope and an increase in pitching moment. At sufficiently high angle of attack the whole of the vortex flow field has undergone breakdown, so that a gross separation without concentrated vortex features exists over the wing.

In recent years, many studies have been conducted in order to understand the aerodynamic characteristics and the flow behavior of unmanned combat air vehicles (UCAVs). UCAVs require higher maneuverability performance; thus, they adopt a delta type swept wing of BWB configuration. The sweptback wing has the advantage to increase aircraft maneuverability which is an utmost important factor for this type of UAV. However, the sweptback wing gauges to unstable, non-linear, pitching moment characteristics due to the complicated vortical structure over the wings [50], which cause an abrupt increment of C_m that results in the loss of longitudinal stability at a high angle of attack [51]. The $C_m - \alpha$ and $C_L - C_m$ curves for Boeing's BWB-450-1L configuration are presented in **Figure 2.20**.

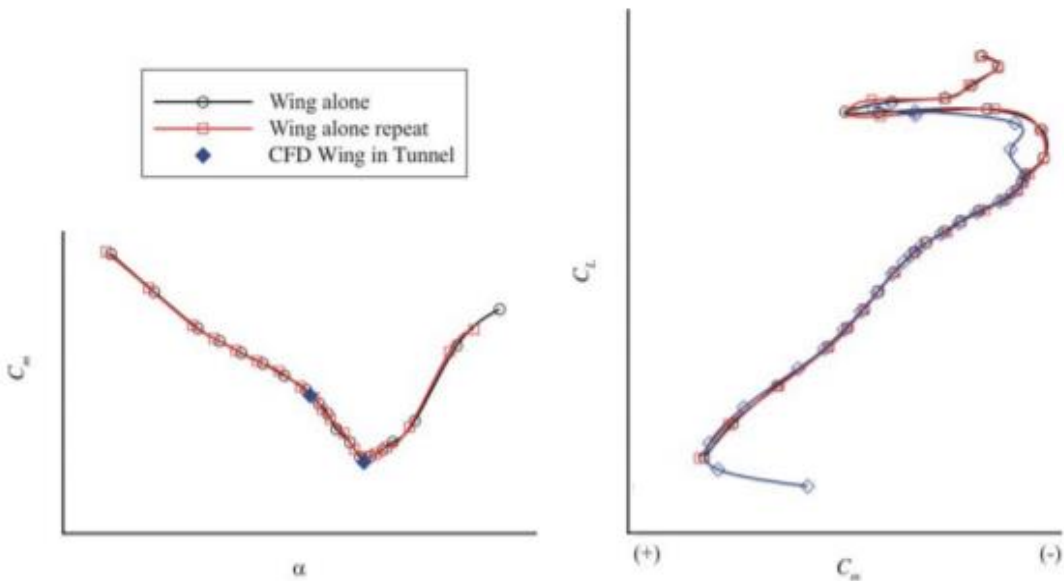


Figure 2.20. $C_m - \alpha$ and $C_L - C_m$ curves for Boeing's BWB-450-1L configuration [52]

Literature [50], [53], [54], showed that the flow of the SACCON UAV, a lambda wing planform with a leading-edge sweep angle of 53° , is governed by very complicated flow structures, which leads to non-linear aerodynamic characteristics at various angles of attack. This non-linear phenomenon was also confirmed in the X-31 aircraft, which has a double delta wing with an inner sweep angle of 57° and an outer sweep angle of 45° [55]. The unstable pitching moment characteristic is associated with flow separation around the outboard wing region and inboard vortex breakdown, which causes loss of lift [56], and this loss of lift generates a rapidly increasing nose-up moment at a specific range of angles of attack. This phenomenon is called 'pitch-break' or 'pitch-up'. The problem of pitch-up has been observed decades ago,

on the Hawker Hunter. By the use of a dogtooth cambered leading-edge extension the problem was overcome, as in high angles of attack, the dogtooth discontinuity reduced the outboard boundary layer flow and delayed tip stalling [57].

As mentioned before, the behavior of the vortex over non-slender wings is very complicated and has been found to be sensitive to parameters such as the swept angle [49], the geometry (radius) of the leading-edge, angles of attack and the Reynolds number. Hence, in order to improve or delay the non-linear characteristics of the pitch-break, several passive methods and aerodynamic devices have been suggested over the years to deal with this phenomenon. HoJoon Shim and Seung-O Park [58] conducted experiments on a BWB UCAV, slightly different from the UCAV 1303, which has a 47° leading-edge sweep angle, using vortex generators. They ascertained that, when the vortex generator was installed, this pitch break was found to be delayed to a much larger angle of attack. Sanghyun P. et al. [59] confirmed the previous statement by performing CFD analysis on the same geometry. HoJoon Shim et al. [60] showed that with the use of trapezoidal shape vortex generators, the flow separation region can be effectively controlled on a BWB UCAV. N.G. Verhaagen [61], [62] studied the effects of

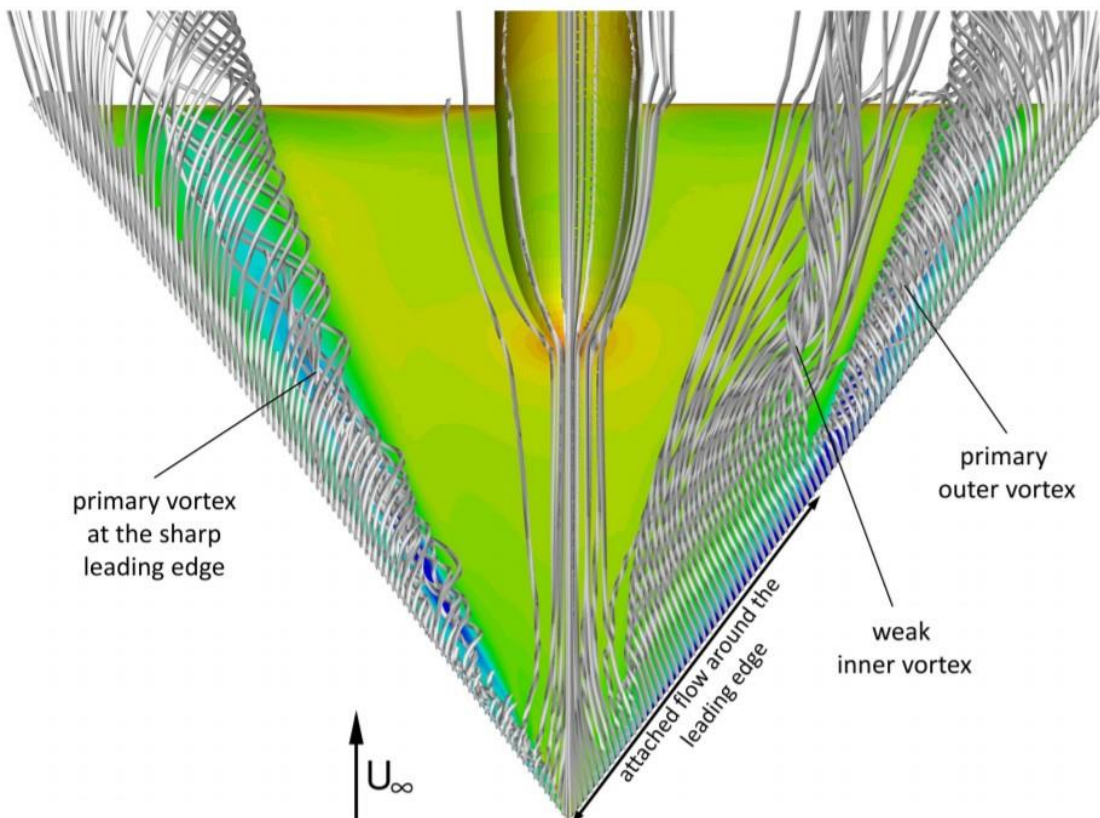


Figure 2.21. RANS Calculation of the Complex Vortex Topology around a Delta Wing with Sharp (left) and Round (right) Leading Edges [64]

different leading-edge radius on the flow over a 50° swept delta wing model. His experiments showed that contrary to a sharp leading-edge, on a rounded edge, the location of the primary separation line and separated flow structure are sensitive to the Reynolds number. However, the size and strength of the primary vortex tend to reduce with increasing leading-edge radius. Also, an increase in leading-edge radius decreases the lift only slightly, but reduces the drag significantly, which results in a higher lift-to-drag ratio, hence better performance of the delta wing at subsonic speeds. Mehdi Ghoreysi et al. [63] showed that for the sharp leading-edge model, separation always seems to occur at the leading-edge. On the other hand, the rounded leading-edge model separation seems to occur at higher angles and may not necessarily be initiated at the leading-edge, but further downstream. Overall, the main difference is that the flow over the rounded leading-edge model has a dual vortex structure for a wider range of angles of attack (**Figure 2.21**). Gwo-Bin Lee et al. [65] explored the feasibility of applying micromachined sensors and actuators to manipulate the flow inside the boundary layer, around the separation region, and control the leading-edge vortices, resulting in a large change in the three-axis moments. Terence Dan D. Vicroy [66] performed a series of low-speed wind tunnel tests on a BWB, while investigating the effect of slats on the pitch break phenomenon. His study showed that with the slats retracted, the configuration exhibits an unstable pitch break over the angle of attack range where the outboard wing section begins to stall prior to the inboard and center body sections. The stall of the outboard wings, which are aft of the moment reference center, resulted in a nose-up pitching moment change. However, deflecting the slat led to a delay of the stall of the outboard section and eliminated the unstable pitch break. As expected, the deflected slat also increased the maximum lift coefficient. A. Ghee [67] conducted experiments on a UCAV with deployable serrated flaps of three different configurations. He examined how their location and height affects the flow structure and found that these devices delay the angle of attack at which outer wing panel separation and wing vortex burst occurred. Weiheng Zhao et al. [51] showed that the leading-edge flap deflection could not only improve the non-linear characteristics effectively through

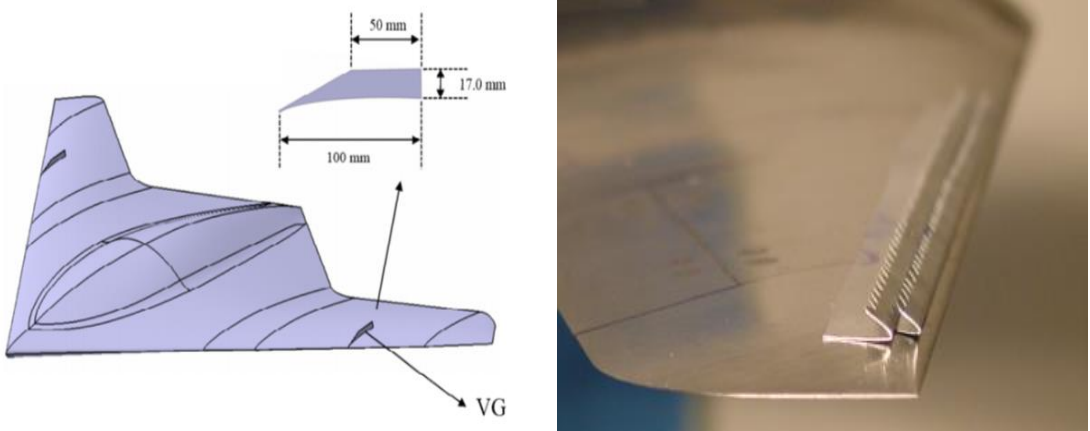


Figure 2.22. Vortex Generator (left) [60] and Deployable Serrated Flaps (right) [67]

the suppression of the outboard flow separation and enhancement of inboard leading-edge vortex, but also improve the maximum L/D of the examined configuration. Kosuke Toyoda et al. [68] conducted wind tunnel tests in order to investigate the effects of the inboard leading-edge flap on vortex behavior and outboard flow. I. Gursul et al. [69] present various flow control methods such as blowing and suction, low and high-frequency excitation, feedback control, passive control with wing flexibility, and plasma actuators.

CHAPTER 3

TOOLS AND METHODS

For the purposes of the current thesis, a number of essential tools and methods were created and utilized. The complete set of these tools and methods is presented in this chapter, starting with the ones corresponding to the Flight Simulator and then the tools used in the Leading-Edge Vortices study.

Flight Simulator

Flight Model

The main part of a complete flight simulator is the model for the flight system. The model includes all the essential data to simulate flight, such as the mathematical model which solves the full set of the Equations of Motion, aerodynamic and other special characteristics of the aircraft, and various information about the interaction of the aircraft with the environment. The model was constructed using Matlab and Simulink [70]. Matlab is a multi-paradigm numerical computing environment and proprietary programming language developed by MathWorks. It allows matrix manipulations, plotting of functions and data, implementation of algorithms, creation of user interfaces, and interfacing with programs written in other languages. Typical uses include:

- Math and computation
- Algorithm development
- Modeling, simulation, and prototyping
- Data analysis, exploration, and visualization
- Scientific and engineering graphics
- Application development, including Graphical User Interface building

Simulink is an additional package, which adds graphical multi-domain simulation and model-based design for dynamic and embedded systems. It supports system-level design, simulation, automatic code generation, and continuous test and verification of embedded systems. When Matlab and Simulink are used together, textual and graphical programming are combined to design a system in a simulation environment. This is the case of the current thesis, where the

two tools were combined, with the Simulink environment being the major one, and Matlab code completing some of the Simulink blocks. The full Simulink model is presented in **Figure 3.1.**

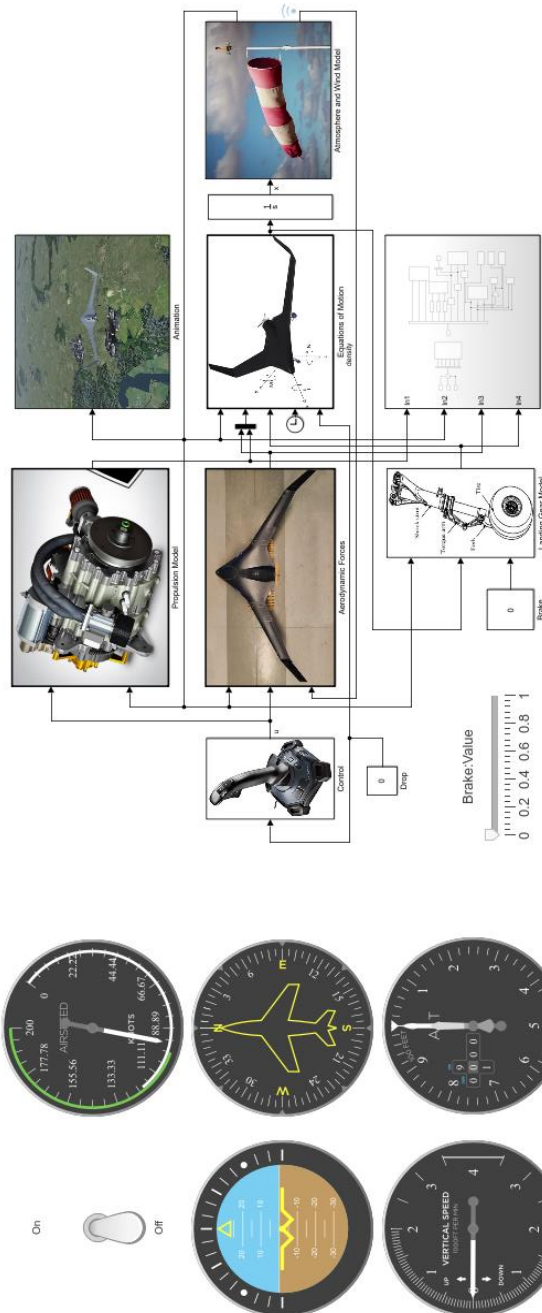


Figure 3.1. Flight Model in Simulink

The model consists of Simulink blocks, with each of them constituting a complete subsystem, playing a specific and different role. The combination of all the subsystems provides the ability to simulate the whole flight envelope. A more extensive description of each subsystem follows.

Control Inputs Model

This is the subsystem that helps the pilot control the aircraft. Inside the block's subsystem, there are two different sets of blocks, with each of them controlling the aircraft in a different way. The first set makes it possible for the aircraft to be controlled via a joystick, using the Pilot Joystick block of the Aerospace Blockset library of Simulink. This block's "inputs" are the joystick commands, with each of them corresponding to a component of the control vector, meaning either a change in throttle or a control surface deflection. In case a specific value is needed for each of the control vector components, such as while testing the aircraft's trim conditions, the second set of blocks can be used. This set consists of Constant blocks for each control vector's component. The constant's value can be changed normally, or by a Slider block connected to it. Multiple Constant blocks can be used for each deflection, one for each mission part, with the right one being enabled by a Switch or Manual Switch block. For instance, while simulating the payload drop phase, there are different trim conditions before and after the payload drop, since the aircraft undergoes various changes in its mass, moments of inertia, and CG location. The simulation starts with the constants corresponding to the pre-drop trim conditions and, using the Switch block, the model automatically changes constants, just by linking it with the Drop Constant. Finally, the change from manual (joystick) to automated flying is achieved with a Manual Switch block.

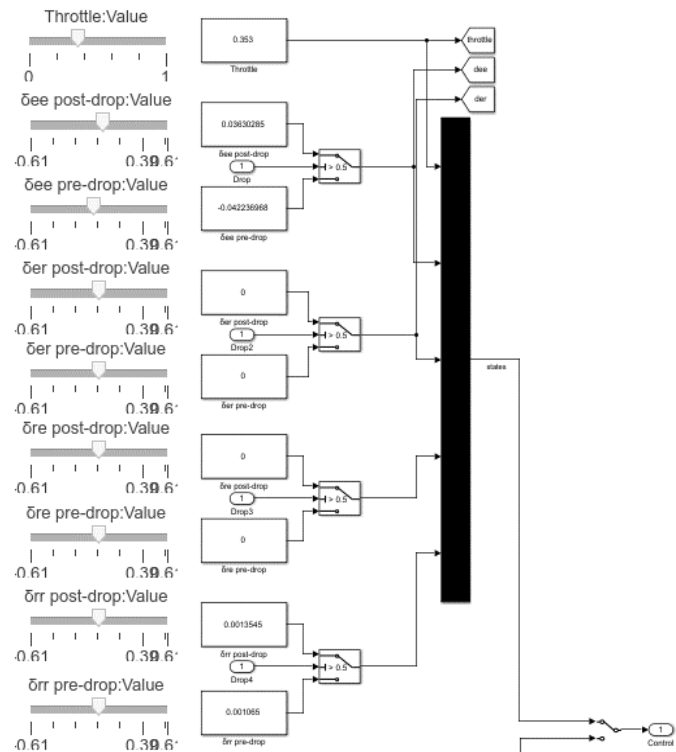


Figure 3.2. Trimmed Flight Control Subsystem

starts with the constants corresponding to the pre-drop trim conditions and, using the Switch block, the model automatically changes constants, just by linking it with the Drop Constant. Finally, the change from manual (joystick) to automated flying is achieved with a Manual Switch block.

Aerodynamic Model

This model uses a Matlab Function Block, provided by the Simulink block library. This kind of blocks contain a function, written in Matlab language code. The function accepts the current state vector, the control vector and the air density as inputs. The function's output is a vector containing the aerodynamic forces and moments on the body coordinate system:

$$y = \begin{bmatrix} X_{aero} \\ Y_{aero} \\ Z_{aero} \\ L_{aero} \\ M_{aero} \\ N_{aero} \end{bmatrix}$$

Each of the aforementioned forces and moments is calculated from each corresponding aerodynamic coefficient, using the equation:

$$F = \frac{1}{2} \rho V^2 C_F S \quad (3.1)$$

for forces, and:

$$M = \frac{1}{2} \rho V^2 C_M S c \quad \text{or} \quad M = \frac{1}{2} \rho V^2 C_M S b \quad (3.2)$$

for moments.

The Aerodynamic Forces block also contains a number of other supplementary functions, in order to compute each of the aerodynamic coefficients, as presented in the polynomial model theory. For instance, the lift coefficient is computed from all the factors that affect it as follows:

$$\begin{aligned} C_L = & C_{L_0} + C_{L_\alpha} \alpha + C_{L_{\alpha^2}} \alpha^2 + C_{L_{\alpha^3}} \alpha^3 + C_{L_{\alpha^4}} \alpha^4 + C_{L_{\alpha^5}} \alpha^5 + C_{L_{\hat{q}}} \hat{q} + C_{L_{\delta_{ee}}} \delta_{ee} \\ & + C_{L_{\delta_{ee}^2}} \delta_{ee}^2 + C_{L_{\delta_{ee}^3}} \delta_{ee}^3 + C_{L_{\delta_{ee}^4}} \delta_{ee}^4 + C_{L_{\delta_{re}}} \delta_{re} + C_{L_{\delta_{re}^2}} \delta_{re}^2 \\ & + C_{L_{\delta_{re}^3}} \delta_{re}^3 + C_{L_{\delta_{re}^4}} \delta_{re}^4 \end{aligned} \quad (3.3)$$

The derivatives such as C_{L_α} , $C_{L_{\hat{q}}}$ etc have been taken from tables and curves, resulted from the combination of CFD analysis and the procedures presented in Ref. [31]. The polynomials cover the whole range of control surfaces' deflection from -35° to 35° . No compressibility effects are considered, since the aircraft's mission lies in the low Mach subsonic regime of around 0.15 M. The model could be more complicated, including more terms, especially coupled ones like C_{L_B} etc, but that was deemed unnecessary for the goals of the current thesis. The effects of those terms are small in comparison with the ones presented in the model,

meaning the resulting deviation from reality will be negligible. The aerodynamic model is accurate for the whole range of angles of attack. In order to simulate and visualize stall, an assumption of loss of lift and an increase in pitching moment has been made, following the theoretical stall behavior from C_L and C_m curves. The stall regime is triggered when the angle of attack becomes greater than the stalling angle of attack.

There are also functions computing the angle of attack and the sideslip angle values from the state vector velocity components u , v , and w . The angle of attack and the sideslip angle are needed in order to transform lift and drag forces from wind to body axes using the transformation matrix:

$$\begin{bmatrix} X_{aero} \\ Y_{aero} \\ Z_{aero} \end{bmatrix} = \begin{bmatrix} \cos\alpha\cos\beta & -\cos\alpha\sin\beta & -\sin\alpha \\ 0 & 1 & 0 \\ \sin\alpha\cos\beta & -\sin\alpha\sin\beta & \cos\alpha \end{bmatrix} \begin{bmatrix} -D \\ Y \\ -L \end{bmatrix} \quad (3.4)$$

Flight Dynamics Model

This model also uses a Matlab Function Block, containing code to solve the full set of equations of motion. It accepts the state vector, the aerodynamic forces and moments vector, the propulsion forces and moments vector, the landing gear forces and moments vector, the current simulation time and a constant which is connected to an on/off switch, as inputs, and outputs the time derivatives of the state vector. These derivatives are then integrated via an integrator block in order to get the new values of the state vector for the next step of the simulation.

The computation of the state derivatives is performed by solving the complete set of equations of motion as shown in the Theoretical Background chapter. The total force and moment in each body axis is computed by summing the forces and moments from the different components on the corresponding axis:

$$F = F_{aero} + F_{prop} + F_{LG} \quad (3.5)$$

$$M = M_{aero} + M_{prop} + M_{LG} \quad (3.6)$$

Moreover, the current block includes the code needed for the case of the payload drop. After releasing the payload, the aircraft undergoes a number of changes. These changes include the reduction of its weight, the relocation of its CG further aft, and new values of its moments of inertia. The on/off switch changes the value of the Drop Constant from 0 to 1, which triggers the aforementioned changes.

Propulsion Model

This is another Matlab Function model, including the code needed to compute the thrust force. The block's inputs are the state vector and the control vector, and the only output is the propulsive forces and moments vector. As a complete modeling of the engine with the propeller is beyond the scope of this thesis, a simplified modeling of the thrust generated is given as follows. The propulsion model is using a polynomial, which was extracted from curves of the engine's power for different values of throttle. Using the throttle value at an instant in time, power is calculated. Then the total thrust is computed with the equation:

$$T = \frac{P\eta_p}{V} \quad (3.7)$$

After an altitude correction is applied, thrust components in body axes are calculated using the propeller's shaft angle from x_B , ε_t :

$$\begin{bmatrix} T_X \\ T_Y \\ T_Z \end{bmatrix} = \begin{bmatrix} T \cos \varepsilon_t \\ 0 \\ T \sin \varepsilon_t \end{bmatrix} \quad (3.8)$$

Finally, thrust's contribution to pitching moment is calculated:

$$M_T = x_T T_Z + z_T T_X \quad (3.9)$$

where x_T and z_T are the coordinates of the thrust vector's origin ($y_T = 0$ since the vector lies on the aircraft's plane of symmetry). Propeller torque is neglected, as its effect is relatively minor.

Landing Gear Model

This is the last Matlab Function model. This one consists of a function which computes the forces and moments, acting on the landing gear, when it is in touch with the ground during take-off or landing. The block accepts the state vector, its time derivative, and a constant as inputs. This constant can take values from 0 to 1, via a slider block, and corresponds to the brake pedal deflection. The block outputs the landing gear forces and moments vector. Using an "if" statement, the current case is determined, in order to compute the forces and moments acting on each gear. The three cases are defined in the Theoretical Background chapter. Then forces and moments are transformed into the body fixed ones:

$$\begin{bmatrix} F_X \\ F_Y \\ F_Z \end{bmatrix} = \begin{bmatrix} -\cos\theta & 0 & -\sin\theta \\ -\sin\theta \sin\varphi & -\cos\varphi & -\cos\theta \sin\varphi \\ -\sin\theta \cos\varphi & \sin\varphi & -\cos\theta \cos\varphi \end{bmatrix} \begin{bmatrix} F_\mu \\ 0 \\ F_V \end{bmatrix} \quad (3.10)$$

$$\begin{bmatrix} L_{LG} \\ M_{LG} \\ N_{LG} \end{bmatrix} = \sum \begin{bmatrix} 0 & -(z_g - \delta_g) & y_g \\ z_g - \delta_g & 0 & x_g \\ -y_g & x_g & 0 \end{bmatrix} \begin{bmatrix} F_X \\ F_Y \\ F_Z \end{bmatrix} \quad (3.11)$$

where depending on the active case:

1. $F_V = 0$
2. $F_V = P \frac{\delta_g}{\delta_{t_P}}$
3. $F_V = P \frac{\delta_{g_{max}}}{\delta_{g_{max}} + \delta_{t_P} - \delta_g} + F_D \quad \text{and} \quad F_D = c_v \dot{\delta}_g$

and:

$$F_\mu = F_V \mu$$

The total force or moment on each axis is the sum of the forces or moments accordingly on every gear:

$$F_{LG} = (F)_{left} + (F)_{right} + (F)_{front} \quad (3.12)$$

$$M_{LG} = (M)_{left} + (M)_{right} + (M)_{front} \quad (3.13)$$

The values for the constants and factors used in the landing gear model have been taken from the manufacturer, in the case of the landing gear parts, and from Ref. [33], in the case of the rolling friction coefficient.

Atmosphere and Wind Model

This model consists of a number of fixed blocks from the Aerospace Blockset library and is presented in **Figure 3.3**. The model requires one single input, which is the state vector. More specifically, it uses the aircraft's position in the earth-fixed z-axis, calculates the current flight altitude and feeds it in the International Standard Atmosphere Model block, which outputs the current temperature, speed of sound, pressure and density at that altitude. As for the wind model, it uses the body velocity components u, v, w , in order to evaluate the current airspeed and feed it in the Discrete Wind Gust Model block. This block generates a gust with a "1-cosine" profile and outputs its velocity. The block's parameters include the gust's direction, starting time, length and amplitude in each axis. Moreover, there is the Wind Shear Model block which takes the current altitude and orientation of the aircraft and calculates the wind's velocity and direction at that height, with respect to the wind's velocity and direction at 6 meters height. Finally, the model includes the Dryden Wind Turbulence Model block, which accepts the current height, airspeed and orientation as inputs, in order to

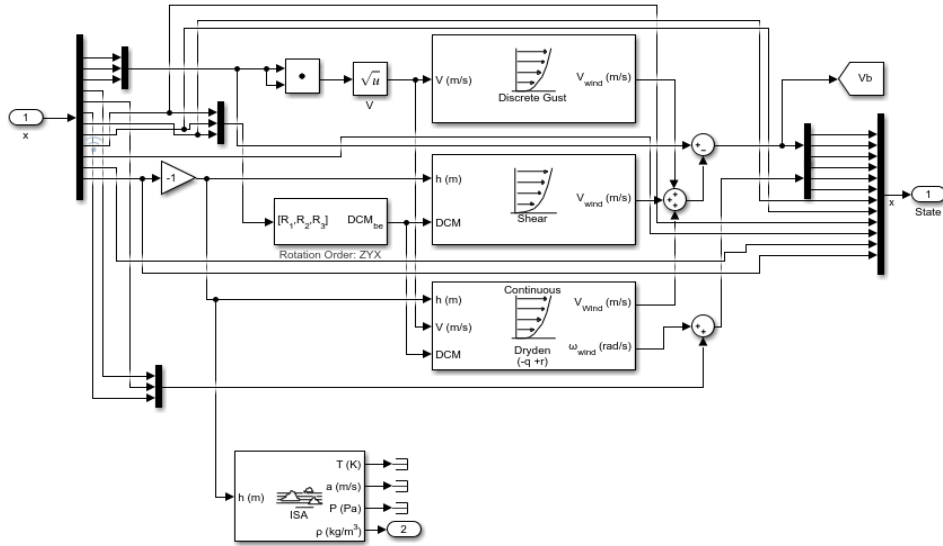


Figure 3.3. Atmosphere and Wind Model

generate atmospheric turbulence. White noise is passed through a filter to give the turbulence the specified velocity spectra, as mentioned in the Theoretical Background chapter. The block's parameters consist of the wind speed and direction at 6 meters height, a scale length at medium/high altitudes, the aircraft's wingspan, a band limited noise sample time, and noise seeds for each velocity component. Since both the Wind Shear Model block and the Dryden Wind Turbulence Model block need the Direction Cosine Matrix as the orientation input, the Rotation Angles to Direction Cosine Matrix block was used to transform the state vector's Euler angles. All the wind model blocks output wind velocities, which are finally summed with the aircraft's translational and angular velocity components, in the body-fixed reference frame, to compute the new ones including the wind effect. The complete atmosphere and wind model outputs the new state vector and airspeed, including the wind effect and the air density at the current altitude.

Auxiliary Blocks

The six aforementioned models constitute the major part of the flight system, forming the main loop of the dynamic model. However, the full model includes a number of auxiliary blocks which contribute in the visualization sector.

Firstly, there are five Flight Instruments blocks. The first one is the Airspeed Indicator. This is another Aerospace Blockset block, which is linked to the airspeed value. Since the block displays velocity in knots, the airspeed must be converted to knots before it is linked to the Airspeed Indicator. The block's role is to make the airspeed's current value visible to the pilot.

at any time during the simulation. Then there are two orientation instruments, the Artificial Horizon and the Heading Indicator blocks. The Artificial Horizon displays θ and ϕ angles, i.e. the pitch and roll orientation of the airplane. The Heading Indicator displays ψ angle, i.e. the yaw orientation. All angles are displayed in degrees. The Flight Instruments group is completed by the Climb Rate Indicator and the Altimeter blocks, showing the airplane's current climb rate and altitude. Each block is linked to its corresponding signal in the model, in order to display the appropriate value.

Additionally, there is the Plots block, where the plots for all the essential variables are created during the simulation. The most important plots will be given in the "Results" chapter for all the phases of the mission.

Finally, the most important auxiliary block is the Animation block. This block also accepts the state vector as input, and through the transformation of the aircraft's position from the earth-fixed coordinate system to latitude, longitude and altitude, it feeds the FlightGear Preconfigured 6DoF Animation block, which is also an Aerospace Blockset block. This block's purpose is to visualize the aircraft's flight in FlightGear, a flight simulator software which will be discussed below.



Figure 3.4. Flight Instruments and Drop Switch

Flight Visualization

Apart from a complete mathematical model, in order for a flight simulator to be functional and useful to the pilot, a realistic visualization of the aircraft and its environment is essential. In order to watch the aircraft in action, FlightGear, an open-source flight simulator software, is used [71]. There is a number of well-known flight simulators in the worldwide industry. However, FlightGear was preferred for the main reason that it has good synergy with Simulink, where the flight simulation model is constructed. This synergy emerges from the FlightGear Preconfigured 6DoF Animation block, making the connection of the two platforms really simple. The whole process of starting FlightGear, selecting a specific aircraft, establishing a UDP connection, identification, and following a reference trajectory is fully automated by a Matlab script.



Figure 3.5. The DELAER RX-3 in FlightGear

FlightGear comes with a library of aircraft models, scenery, environmental conditions, and a variety of other settings for the pilot to customize the flight conditions of his mission. However, in the case at hand, FlightGear's flight system is completely substituted by the Simulink model, meaning that its purpose is a clear, realistic, real-time visualization of the

flight. Real-time visualization is really valuable in understanding the aircraft's behavior. Moreover, the "cockpit" display shown in **Figure 3.6**, provides a lot of useful information, such as longitude, latitude, altitude, pitch angle etc. These data are essential for the pilot during flight, having a major part at the aircraft control. A notable detail is that not only Simulink feeds FlightGear with information, but also FlightGear sends data back to the Simulink model. For instance, FlightGear's ground elevation is essential for the correction of the aircraft's current altitude in the Landing Gear model, so that the aircraft, in the visualization, lands on the ground and not below it. All the aforementioned advantages make FlightGear a very valuable tool for testing and understanding the behavior and performance of an aircraft as well as its interaction with the environment during a computer simulation.

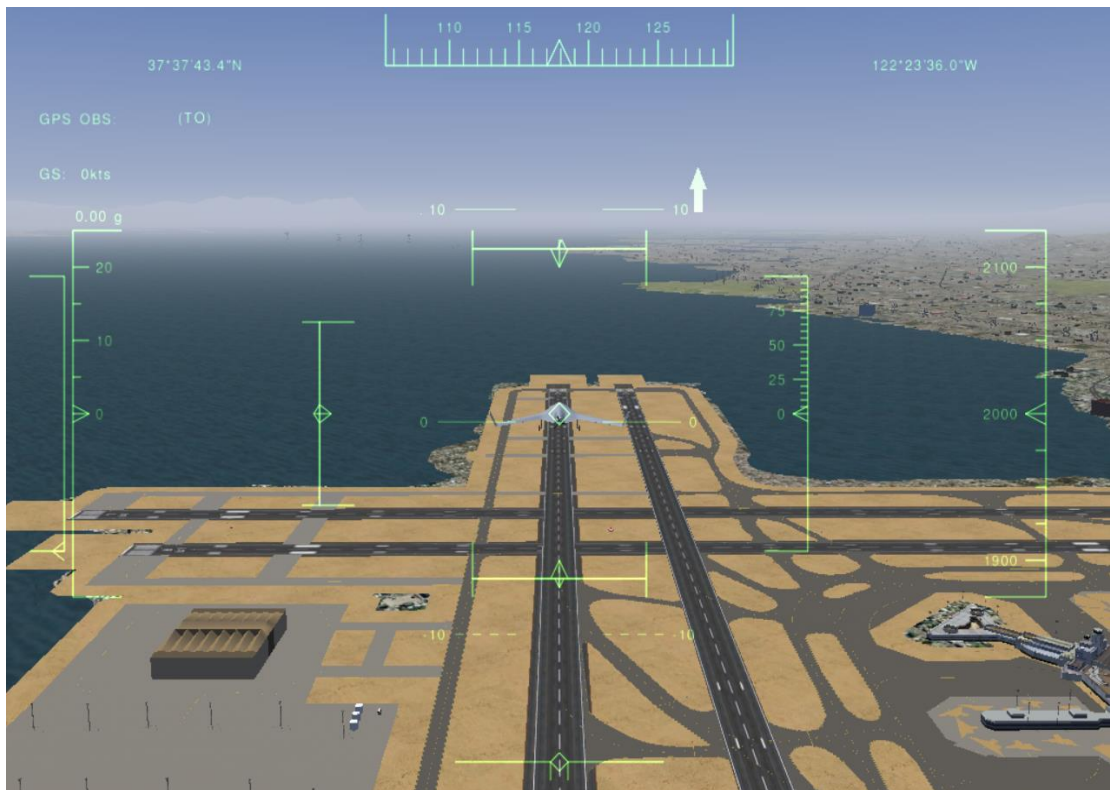


Figure 3.6. FlightGear "Cockpit" Display

Another characteristic of FlightGear is that it accepts custom aircraft models, apart from the ones already installed. The only restriction is that the aircraft model file needs to be in AC3D format. This means that any 3D-CAD model can be inserted in FlightGear, after it is transformed into an AC3D file. A very useful tool for this purpose is Blender [72]. A variety of file formats can be imported, such as object files in the case at hand, in order to be exported in another format. Moreover, Blender has plenty of customization options for the imported model, including positioning, orientation, scaling, materials, textures etc.

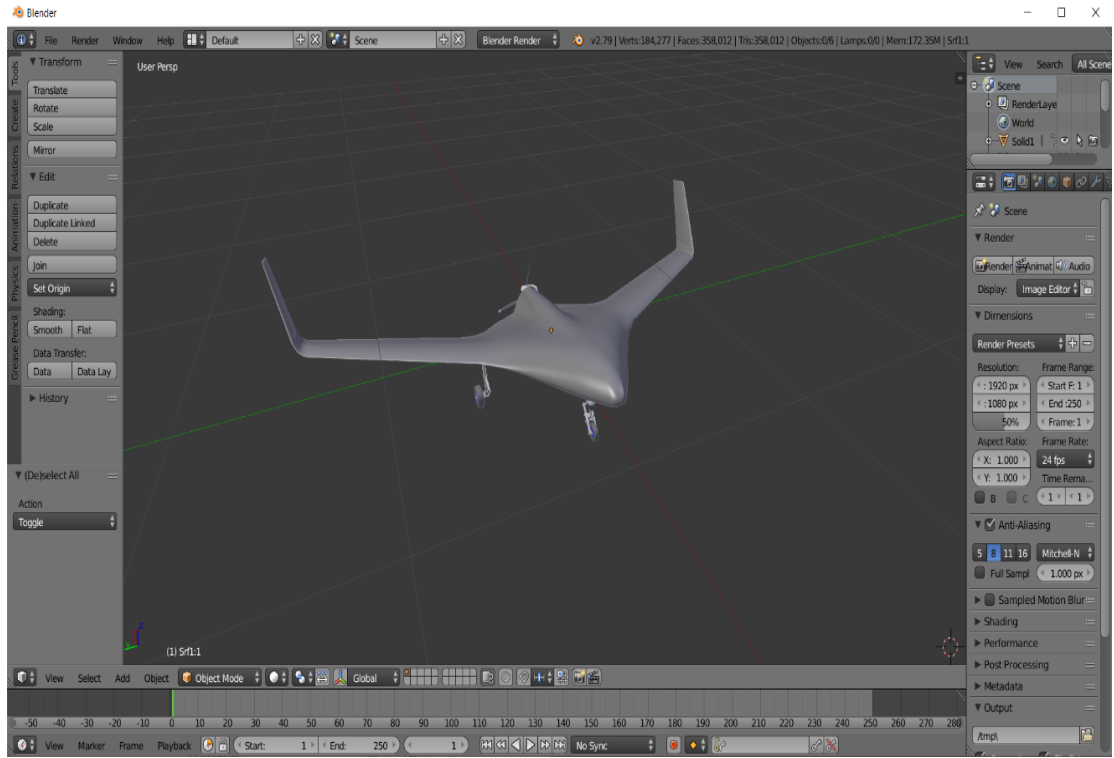


Figure 3.7. The DELAER RX-3 in Blender

Leading-Edge Vortices

Experimental Results

The LEV phenomenon has been investigated experimentally on a BWB configuration similar to the DELAER RX-3, in a closed-circuit, low-speed wind tunnel facility, at the Laboratory of Fluid Mechanics and Turbomachinery (LFMT), at the Mechanical Engineering Department of the Aristotle University of Thessaloniki (AUTH) [20]. In order to examine this phenomenon, a combination of flow visualization studies and velocity point measurements (LDA) were employed. **Figure 3.8** presents the surface oil visualization results at various angles of attack. This technique provides limited information regarding the flow over the wing, such as the flow separation regions, however, it yields clear evidence of the existence of leading-edge separation over the center body. That can be clearly seen for angles of attack larger than 10° , where both the primary attachment line (A1) and separation line (S1) can be identified. Hence, it appears that the flow over the BWB surface combines the conventional flow development over a wing with the leading-edge separation phenomena, similar to the ones encountered over Delta Wing configurations.

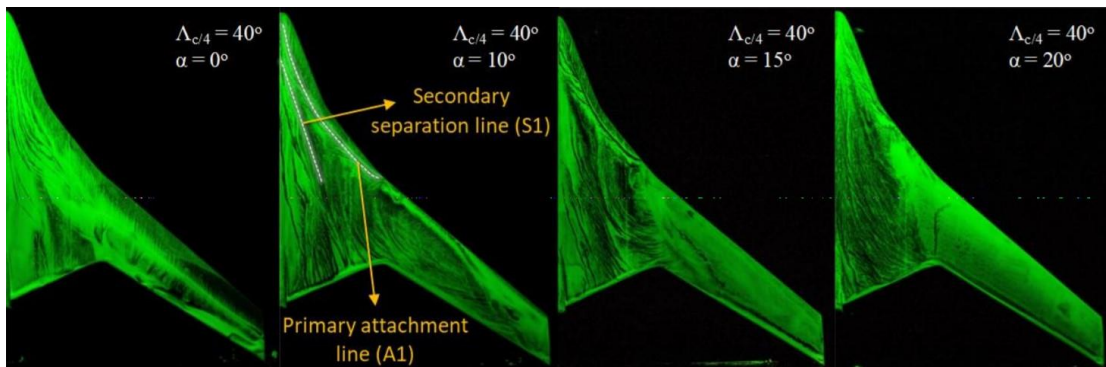


Figure 3.8. Surface Flow Visualization on the 40° Sweep Angle BWB Configuration [20]

By intersecting the smoke wire trails with a laser sheet on the YZ plane, valuable information was extracted regarding the presence of vortical structures around the BWB configurations. The visualizations presented in **Figure 3.9** are in agreement with the findings of the surface visualizations, proving the existence of a well-defined pair of vortices that are a result of the leading-edge separation. In a similar fashion to the vortices encountered over a double delta wing, there is a primary, larger in size and more robust vortex, and a second, rapidly oscillating secondary vortex that could only be seen in the high-speed images.

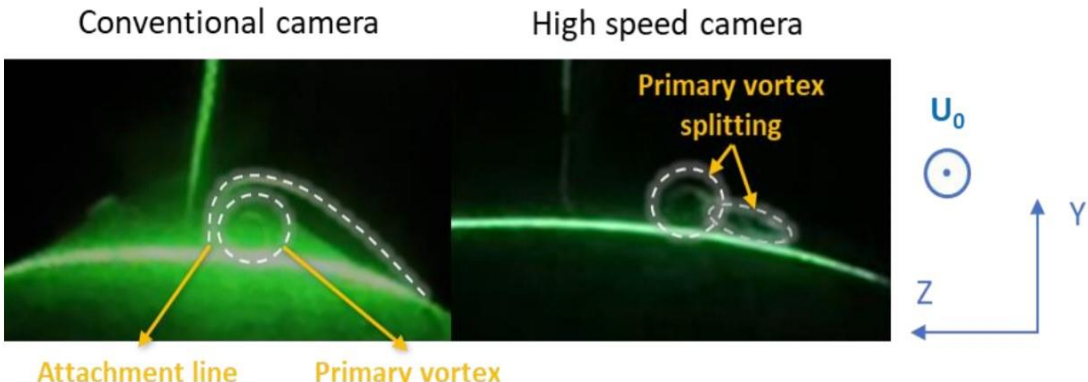


Figure 3.9. Annotated Smoke Wire/Laser Sheet Visualization over the Center Body at $\alpha = 10^\circ$ ($\Lambda_{c/4} = 40^\circ$) [20]

The LDA measurements were focused at two locations, i.e. downstream of the wingtip and over the center body, to investigate the wingtip vortex and the leading-edge separation, respectively (Figure 3.10). Regarding the wingtip investigations, the corresponding measurement plane was located one tip chord downstream of the wingtip. Both the streamwise and normal velocity components, measured at the tip vortex plane, are presented in Figure 3.11. The freestream velocity and the model's tip chord are used to normalize the axes of the figure. Furthermore, in Figure 3.11 the axial vorticity is presented, as calculated from the measured swirl velocity components (Equation 3.14).

$$\Omega = \frac{dW}{dY} - \frac{dV}{dZ} \quad (3.14)$$

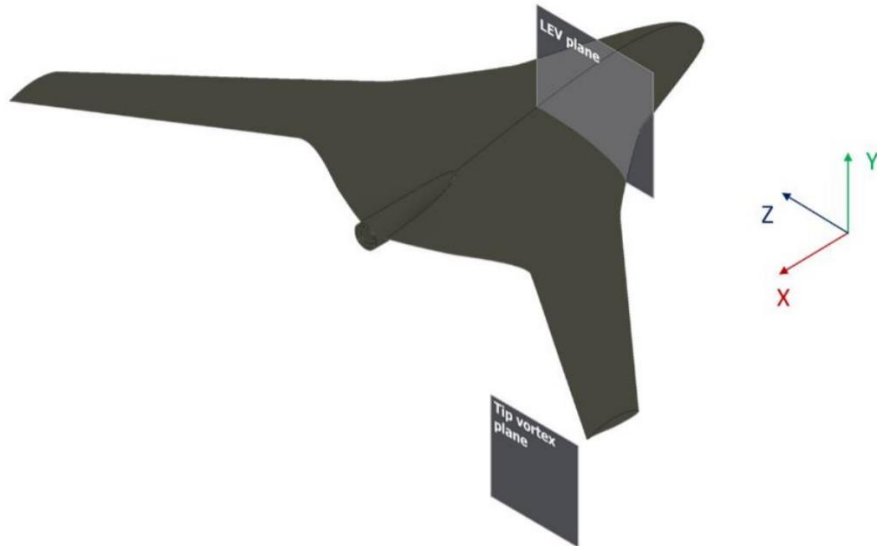


Figure 3.10. Topology of the LDA Measurement Grids [20]

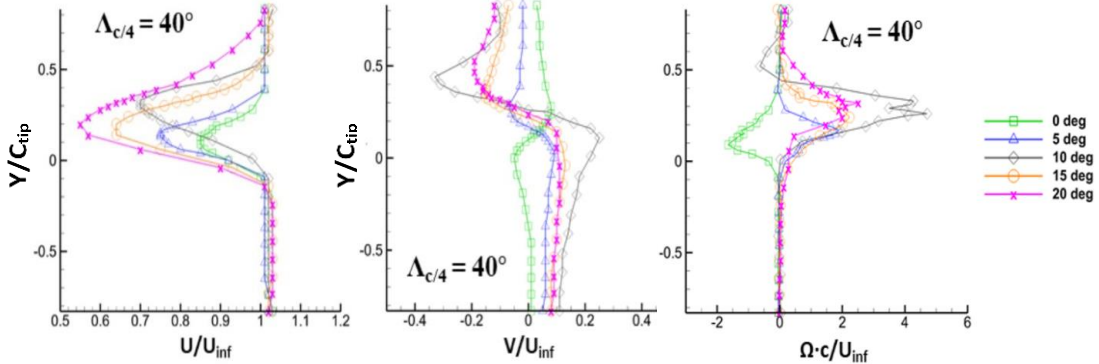


Figure 3.11. Line Plots of Time-Averaged Axial (left) and Normal (middle) Velocity and Axial Vorticity inside the Vortex, at $X/C = 1$ and Various Angles of Attack [20]

Figures 3.12 and 3.13 present the complete set of measurements in contour plots, more specifically the time-averaged streamwise and normal velocity components at an angle of attack of 10° . The measurements begin 1.8 mm away from the model surface, since moving closer hampered the signal acquisition, due to inadequate seeding [20]. A clearly defined vortical structure can be observed over the model. In contrary to the laser sheet visualizations though, only one vortical structure is observed, which can be attributed to the fact that the values presented in this work are time-averaged quantities and, therefore, the oscillations cannot be captured by the velocity measurements. These contour plots will be extracted from the CFD simulations to compare the aforementioned turbulence models, along with the line plots in **Figure 3.11**. It should be noted at this point that the y and z axes of the CFD coordinate system are reversed compared to the experiment. Hence, the y axis of the experiment corresponds to the z axis of the CFD, and vice versa.

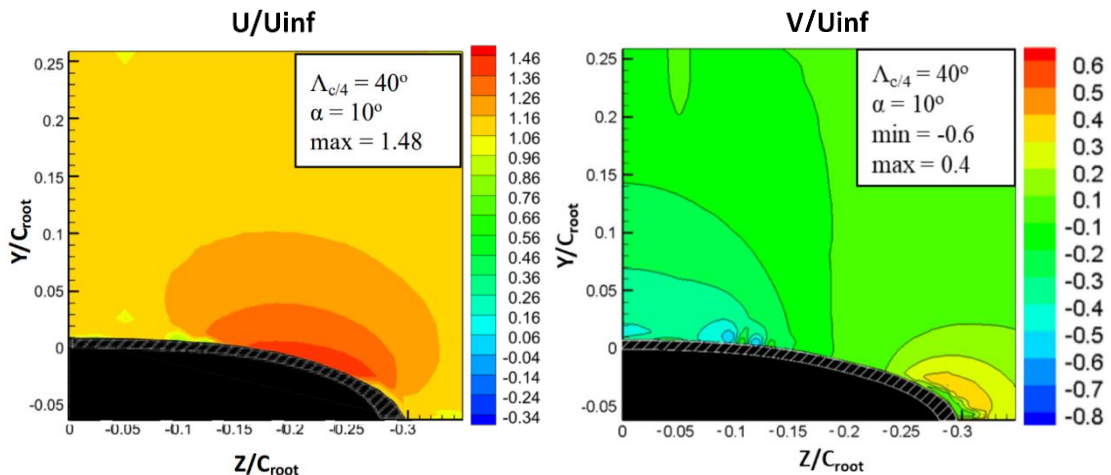


Figure 3.12. Time-Averaged Streamwise (left) and Normal (right) Velocity at $X/C_{root} = 0.5$ [20]

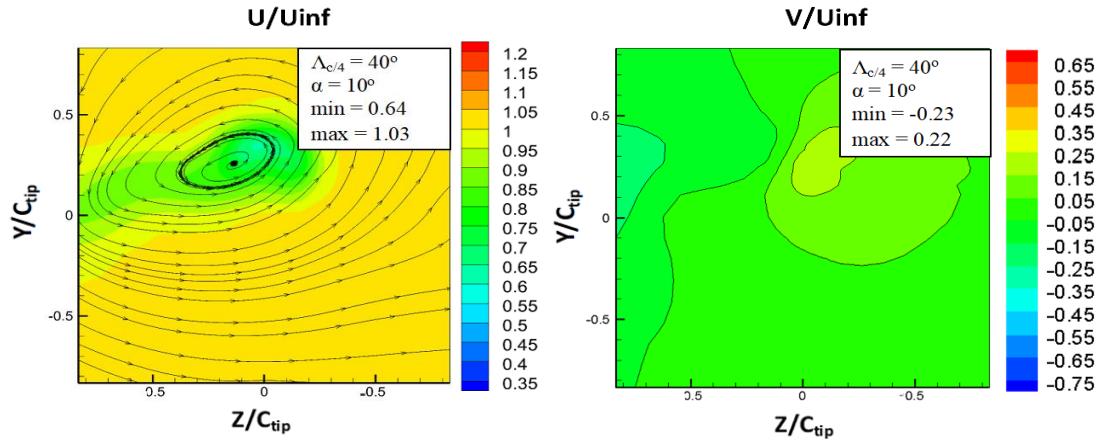


Figure 3.13. Time-Averaged Streamwise (left) and Normal (right) Velocity at the Tip Vortex Plane [20]

CFD Analysis

CFD simulations were carried out at an angle of attack of 10° , using four different turbulence models, namely Menter's SST, Transition SST ($y\text{-}Re_\theta$), Spalart Allmaras with rotation curvature correction (SA-RC) and Reynolds Stress Model (RSM), in order to decide which one presents the vortical structures over a BWB configuration with higher accuracy, compared to the experiment outputs. This model will be used later to simulate the vortical flow over the DELAER RX-3.

Mesh and Computational Setup

First, a mesh of 13,925,904 computational nodes was generated with ANSA 19.0.1. 18 inflation layers were generated, with a growth rate of 1.2, with the first one having a thickness of 0.0013 mm, resulting in a maximum y^+ around 0.345 (Figure 3.14), which ensures that low-Reynolds number effects inside the boundary layer regions will be modeled with high accuracy. It should be noted that, in order to increase the accuracy,

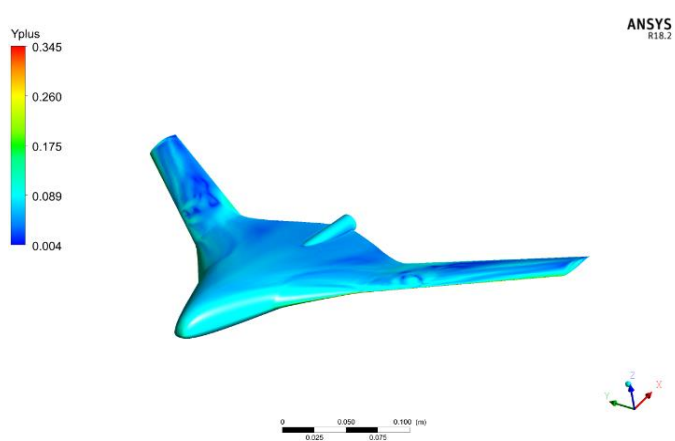


Figure 3.14. y^+ on the BWB Configuration

the grid is denser at the locations of the tip vortex and the leading-edge vortex. The inlet conditions correspond to the wind tunnel conditions, i.e. a freestream velocity of 13.4 m/s and a pressure of 1 atm. The length of the computational domain is 1810 mm long, 600 mm wide and 600 mm high (**Figures 3.15 and 3.16**), which corresponds to the wind tunnel's test section geometry. Besides the BWB configuration, the top, bottom and side far-field faces were treated as a no-slip wall. Menter's SST and RSM were used as turbulence models in ANSYS CFX 18.2, while Transition SST and SA-RC were solved using Fluent 18.2.

ANSYS
R18.2

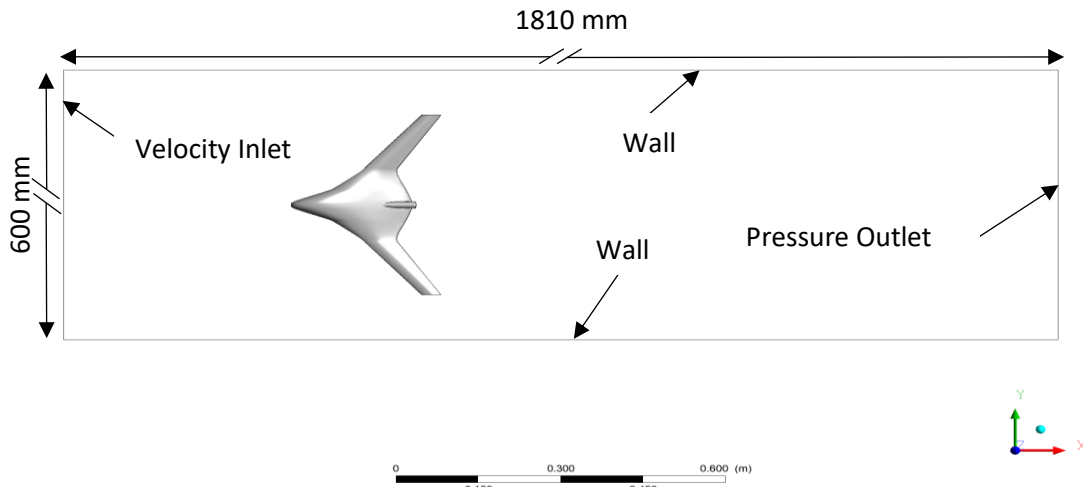


Figure 3.15. Computational Domain around the Experimental BWB Configuration (Top View)

ANSYS
R18.2

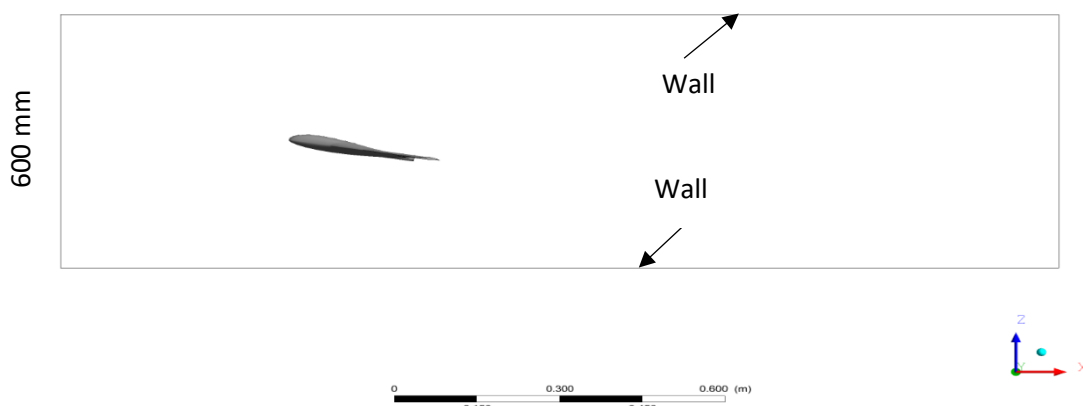


Figure 3.16. Computational Domain around the Experimental BWB Configuration (Side View)

Grid Sensitivity Study

Concerning the DELAER RX-3 model, a grid sensitivity study was conducted at an angle of attack of 8°. The purpose of this study was to determine the optimal density of nodes required around the aircraft and surrounding far-field volume. The grid becomes less dense with decreasing the number of nodes, however, it should be noted that the initial cell height remained the same across all grid geometries to ensure that the y_{avg}^+ will be maintained around 1, which ensures that low-Reynolds number effects inside the boundary layer regions will be modeled with high accuracy. 18 inflation layers were generated, 15 of which with a growth rate of 1.2 and 3 additional layers (**Figure 3.17**). A total of six different grids were examined. **Table 3.1** shows the total elements, nodes, the initial cell height and the initial average first wall spacing y_{avg}^+ for each grid.

Table 3.1. Grid Statistics at $\alpha = 8^\circ$

Grid Name	Grid Quality	Elements (10^6)	Nodes (10^6)	Initial Cell Height [m]	y_{avg}^+
I	Most Coarse	11.24	3.92	1×10^{-5}	1.087
II	Coarser	16.72	5.84		1.101
III	Coarse	22.17	7.89		1.111
IV	Fine	34	12.25		1.125
V	Finer	45.12	16.22		1.131
VI	Most Fine	52.14	19		1.132

Figure 3.18 presents the examined computational grids at the aircraft's nose. Concerning the simulation, the inlet conditions correspond to the reference conditions, i.e. a freestream velocity of 50 m/s and a flight altitude of 2000 m. The length of the computational domain

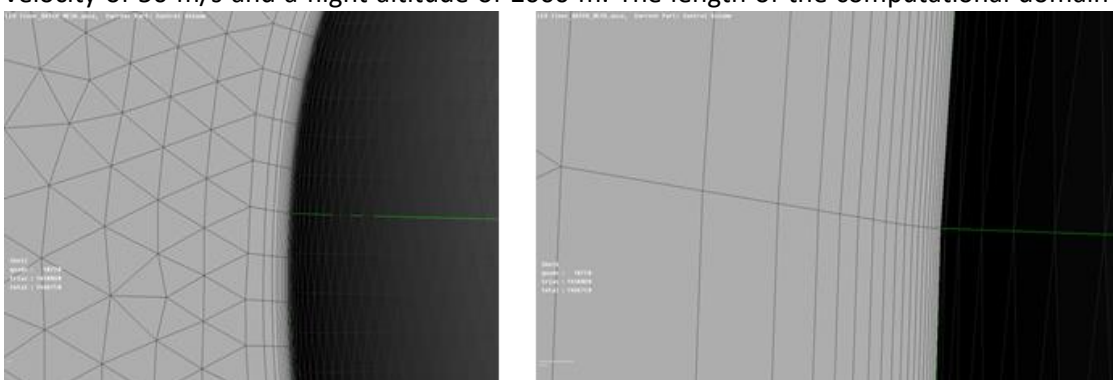


Figure 3.17. Detail View of the Generated Inflation Layers of the Computational Grid around the DELAER RX-3

along with the boundary conditions is illustrated in **Figures 3.19** and **3.20**. For time saving, half of the UAV was modeled. As for the turbulence model, the Spalart-Allmaras was adopted.

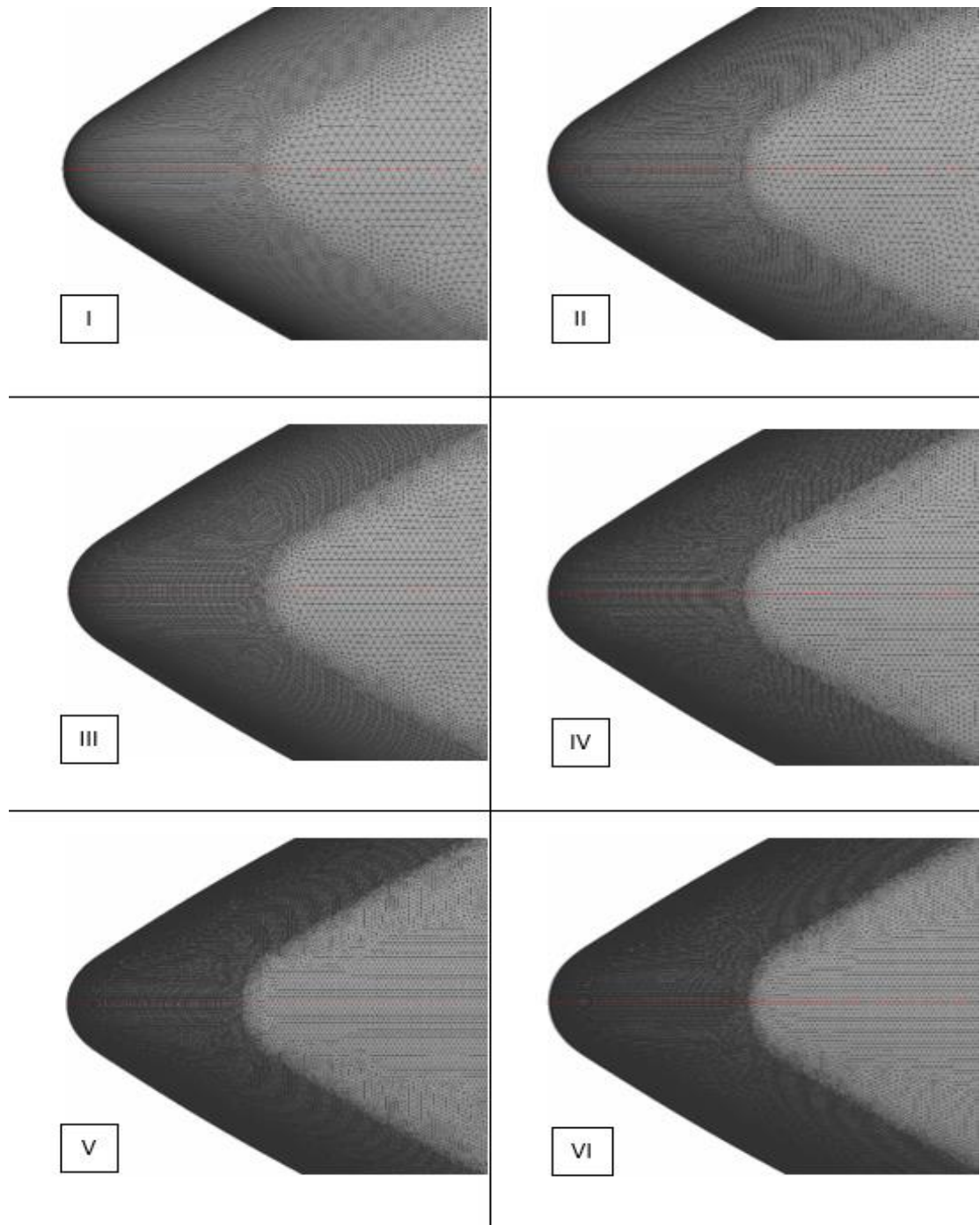


Figure 3.18. Comparison of the Examined Computation Grids (Nose Region)

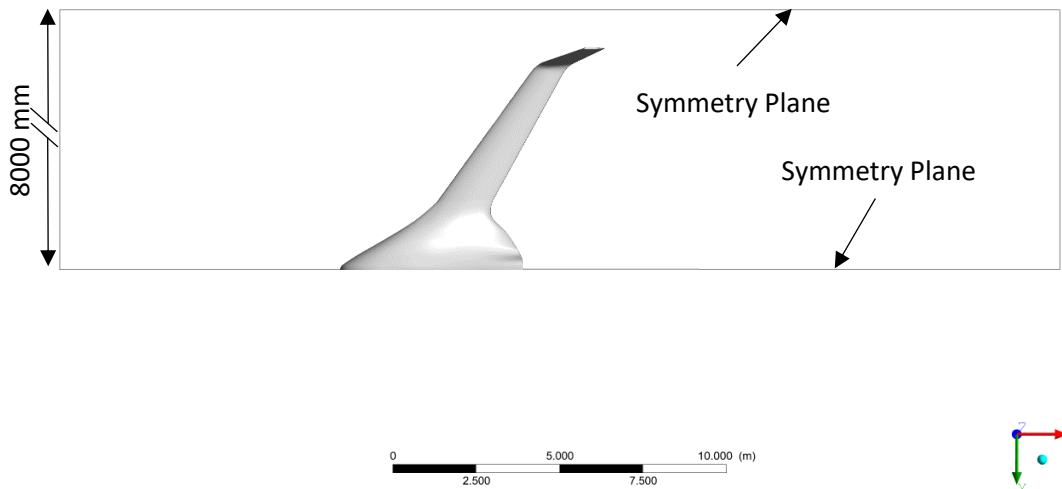


Figure 3.19. Computational Domain around the DELAER RX-3 (Top View)

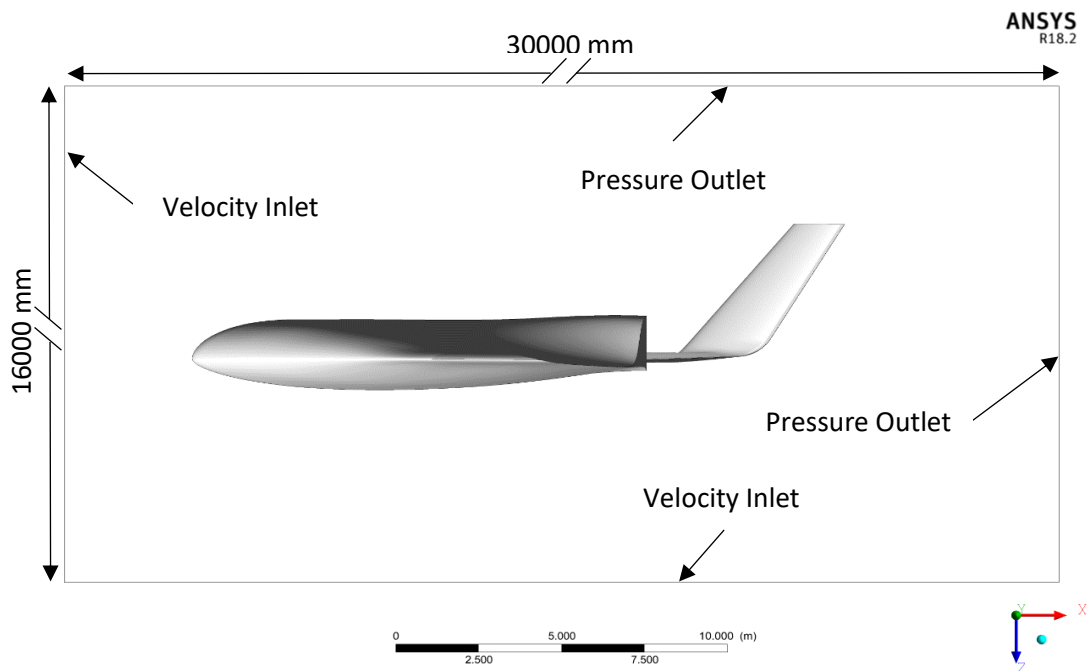


Figure 3.20. Computational Domain around the DELAER RX-3 (Side View)

In order to choose the ideal grid for the current study and examine the grid independency of the solution, drag, lift and pitching moment at two different points were collected (**Table 3.2**). The absolute relative errors between the developed grids are presented in **Table 3.3**.

Table 3.2. Forces and Moments at $\alpha = 8^\circ$

Grid Name	Grid Quality	Drag [N]	Lift [N]	Pitching Moment at 1900 mm [Nm]	Pitching Moment at 2008 mm [Nm]
I	Most Coarse	180.43	2761.49	-152.70	145.34
II	Coarser	173.18	2821.73	-188.16	116.22
III	Coarse	168.31	2861.41	-212.79	95.76
IV	Fine	163.18	2902.40	-236.11	76.75
V	Finer	161.86	2923.93	-249.86	65.28
VI	Most Fine	160.60	2929.55	-253.51	62.21

Table 3.3. Absolute Relative Errors at $\alpha = 8^\circ$

Grid Name	Grid Quality	Drag [%]	Lift [%]	Pitching Moment at 1900 mm [%]	Pitching Moment at 2008 mm [%]
I	Most Coarse	4,015	2,18	23,22	20,04
II	Coarser	2,81	1,40	13,08	17,60
III	Coarse	2,67	1,43	10,96	19,85
IV	Fine	1,19	0,74	5,82	14,94
V	Finer	0,77	0,19	1,46	4,70
VI	Most Fine	-	-	-	-

Based on the grid sensitivity study, evaluating the lift, drag and pitching moment versus grid size, the conclusion is that the use of Grid V is the appropriate one to represent the flow physics at the full range of angles of attack and give an accurate grid-independent solution. As it can be observed, the absolute relative error of the finer grid is less than 1%. Therefore, this grid, with 16.22 million nodes, will be used in this research. The aforementioned quantities are presented in the following figures, as a function of grid nodes.

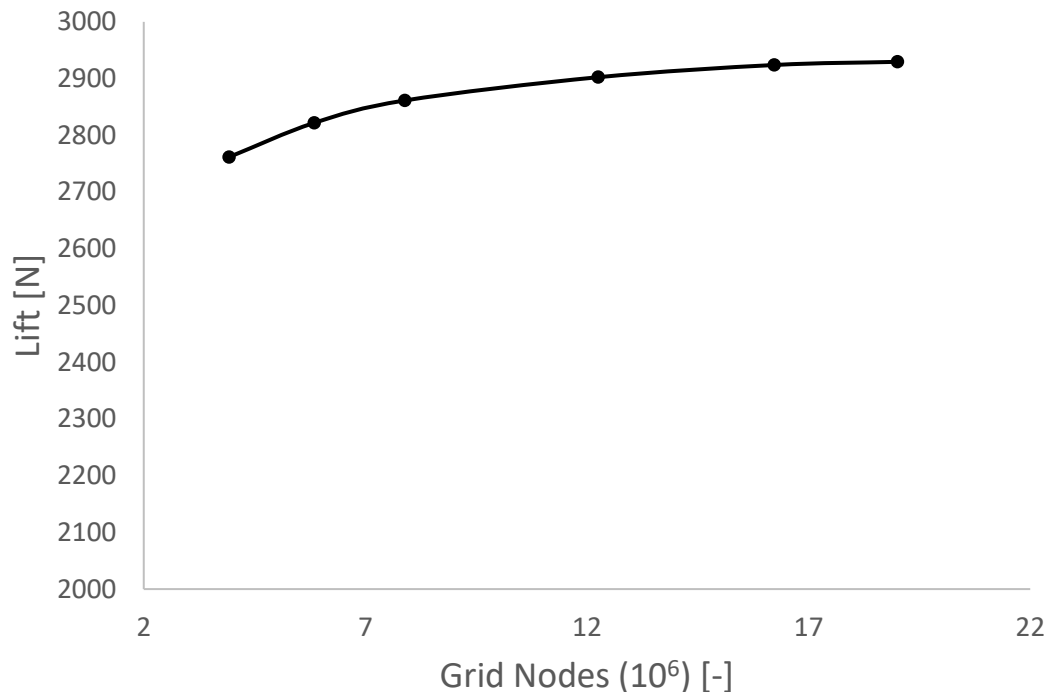


Figure 3.21. Lift as a Function of Grid Nodes

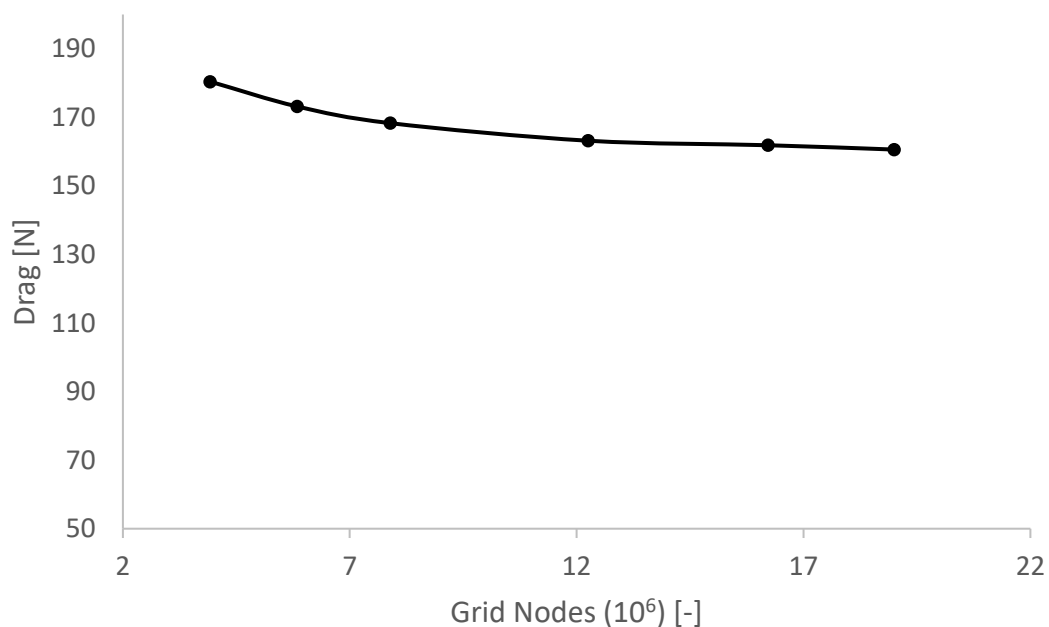


Figure 3.22. Drag as a Function of Grid Nodes

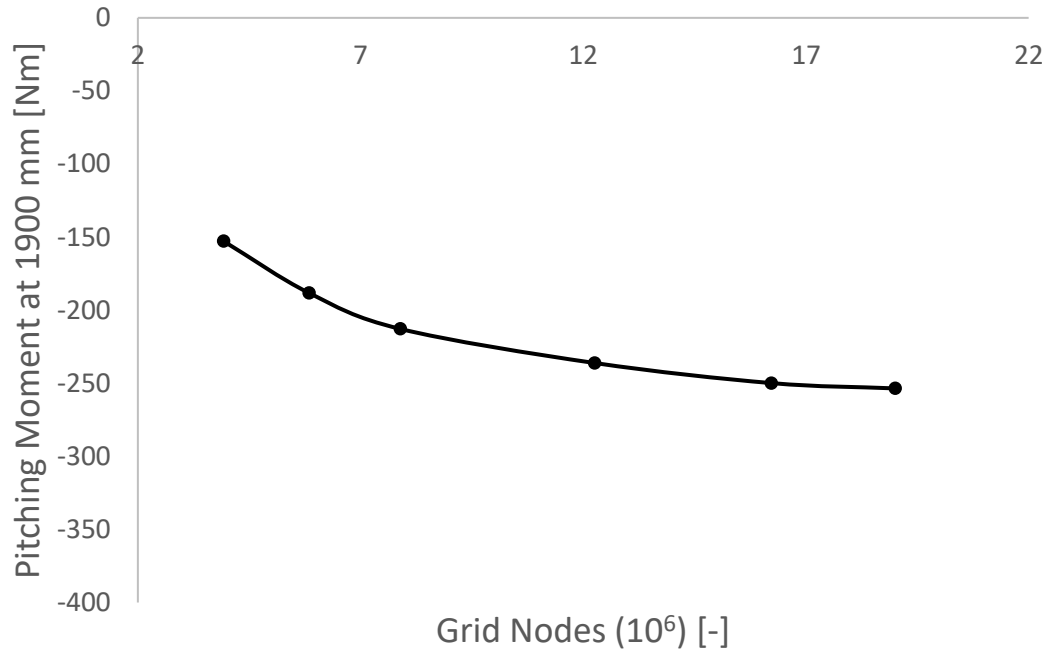


Figure 3.23. Pitching Moment (at 1900 mm) as a Function of Grid Nodes

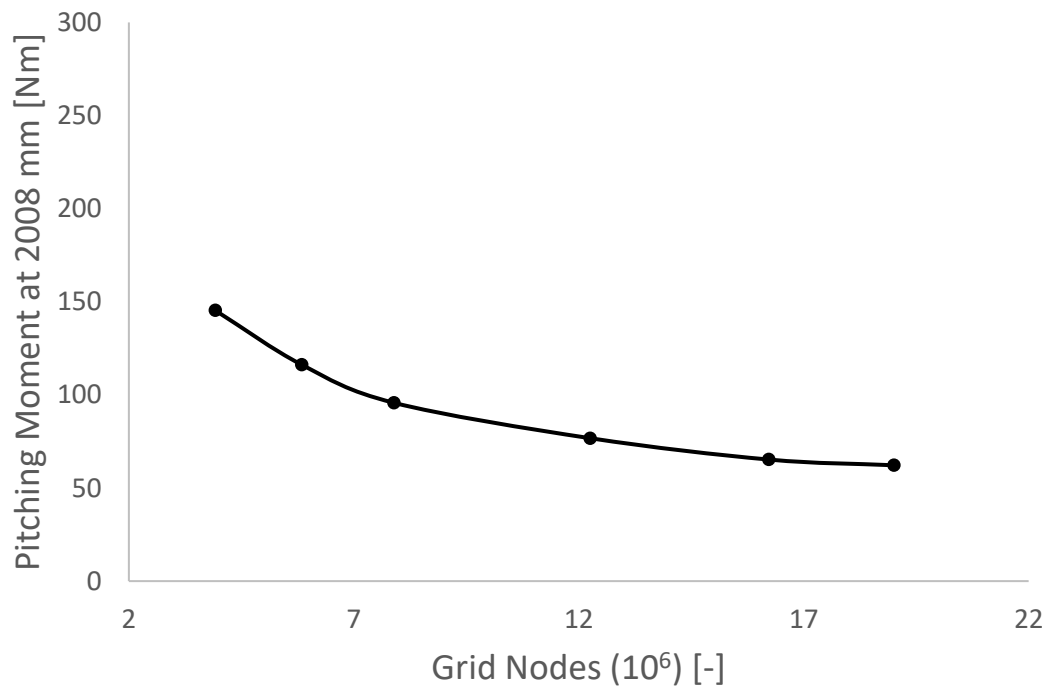


Figure 3.24. Pitching Moment (at 2008 mm) as a Function of Grid Nodes

CHAPTER 4

RESULTS

Flight Simulator

Cruise

The biggest part of the mission is the cruise part, when the aircraft flies in equilibrium. The results of the simulation for the major variables of the cruise part are presented below. It is crucial for an aircraft to be trimmed, so that the least amount of effort is required by the pilot and drag is kept to a minimum. The longitudinal trim conditions for the cruise part before the payload drop, at an altitude of 2 km, are presented in **Table 4.1**.

Table 4.1. Pre-Drop Cruise Trim Conditions

Throttle	35.3%
Thrust	176 [N]
Elevon Deflection as Elevator	-2.42 [deg]
Angle of Attack	2 [deg]
Airspeed	50 [m/s]

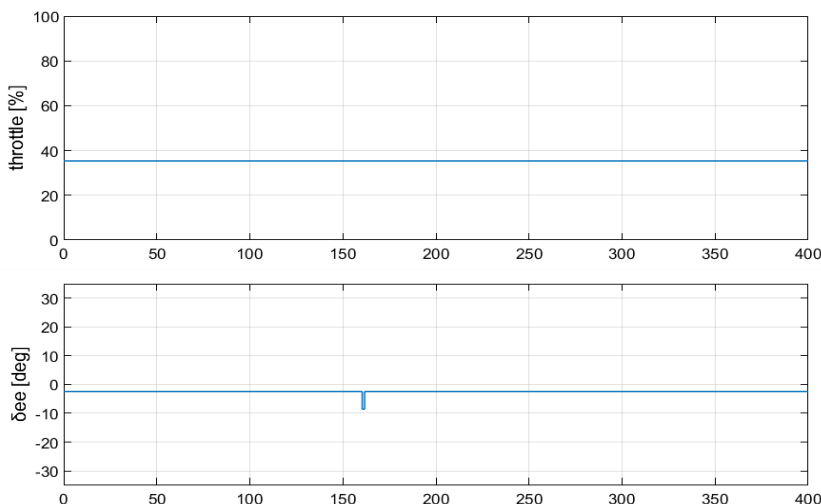


Figure 4.1. Throttle and Elevon Deflection as Elevator for Pre-Drop Cruise

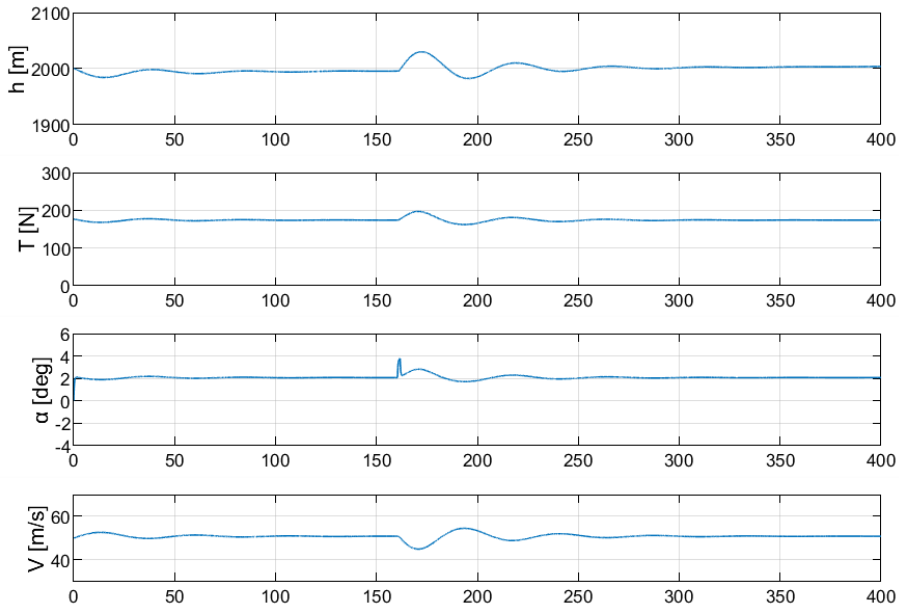


Figure 4.2. Trim Conditions for Pre-Drop Cruise

Those trim conditions resulted from detailed study of the aircraft's performance. Then, the values for throttle and elevon deflection were applied to the simulator, in order to visualize cruise and check the values of the rest of the variables. These values are presented in **Figure 4.2**. From the graphs it becomes clear that the aircraft has the expected behavior, performing a straight level flight. It is obvious that the trim conditions match those of **Table 4.1**, produced from other tools, a fact that validates the model's accuracy. At a point during the simulation, a forced change in elevon deflection is applied, and it is instantly returned to the trim value. This deviation results in an aircraft motion called phugoid. The phugoid mode is an oscillatory mode, characterized by a repeated exchange in altitude and velocity. As the aircraft gains altitude, velocity decreases and the nose drops. When the pitch angle becomes negative, the aircraft starts losing height and velocity increases. With increasing velocity, the nose rises again, and the motion is repeated. This behavior becomes clear in **Figures 4.2** and **4.3**. Since the oscillation dampens, the aircraft is statically and dynamically stable at the longitudinal plane and continues in a trimmed flight. The phugoid's period is approximately 45 s.

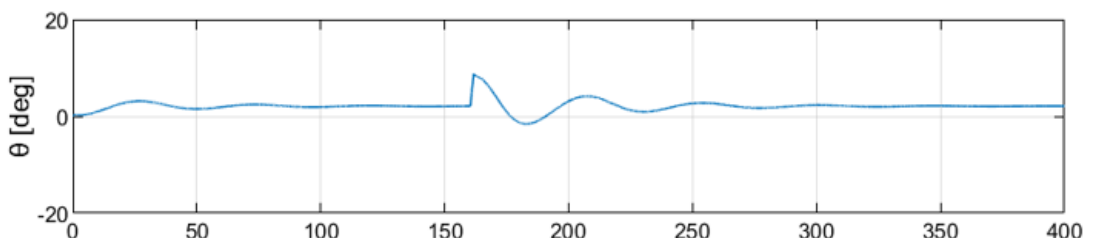


Figure 4.3. Pitch Angle for Cruise

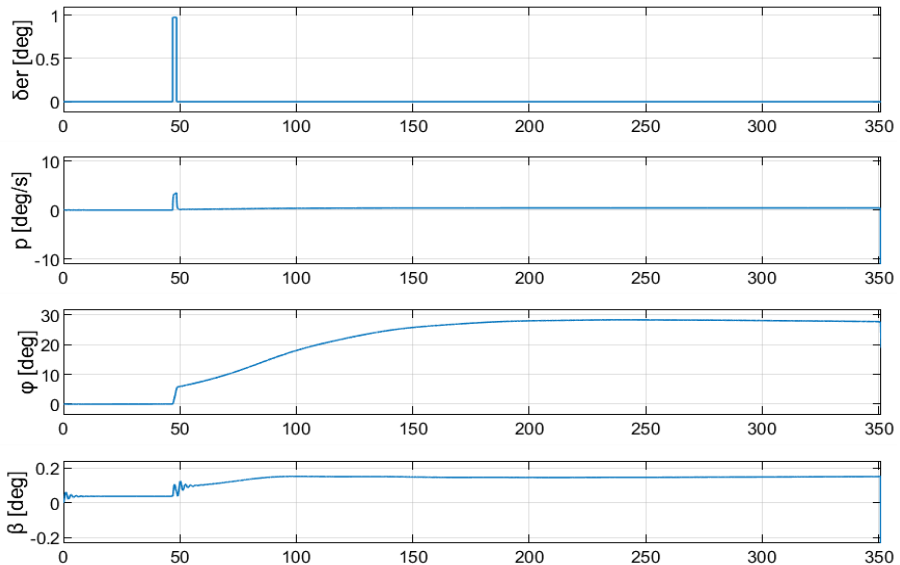


Figure 4.4. Spiral Mode Characteristic Variables

As for the aircraft's lateral-directional stability during straight level flight, a deflection of the aileron is applied this time, leading to the so-called spiral mode. The spiral mode is usually excited by a disturbance in sideslip, which typically follows a disturbance in roll and causes a wing to drop. From straight level flight, with the aileron deflection, a roll angle ϕ is developed. This results in a small sideslip angle β , which produces lift and, in turn, generates a yawing moment to turn the aircraft into the direction of the sideslip. The yawing motion produces differential lift across the wingspan, which in turn results in a rolling moment, causing the starboard wing to drop further thereby exacerbating the situation. The spiral mode in the case at hand is unstable, leading to a slowly divergent spiral descent. However, since the divergence rate is very slow, the phenomenon can be easily avoided by the pilot or an autopilot control system. The spiral mode is described by the time it takes for angle ϕ , which resulted from the aileron deflection, to be doubled. It takes 30 seconds for the ϕ angle to get from 6 to 12 degrees, as shown in **Figure 4.5**, which is long enough to categorize the phenomenon as acceptable.

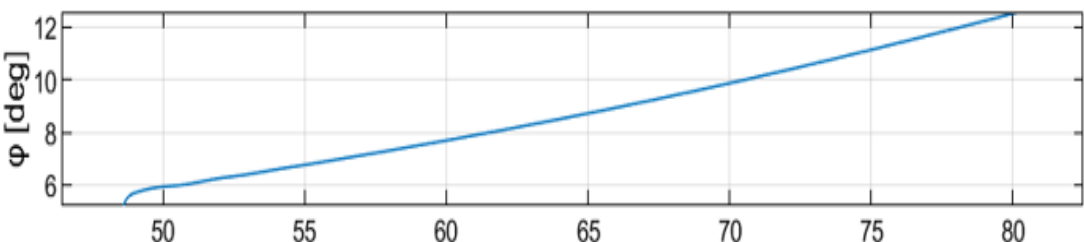


Figure 4.5. Roll Angle Doubling Time

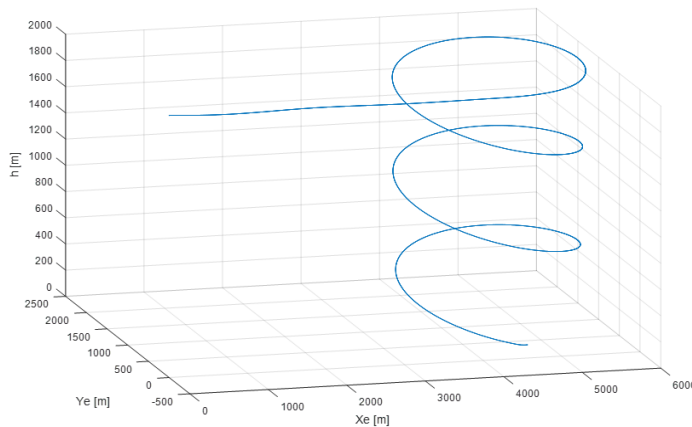


Figure 4.6. Spiral Descent (graph Y-axis is opposite to the simulation Y-axis)

The same procedure was followed for the second cruise phase, after dropping the payload. As already stated, when the payload is removed, the aircraft undergoes changes in its mass, moments of inertia and CG position. This results in changes in the aircraft's behavior, and of course in its trim conditions. The new trim conditions are presented below. The results show that the aircraft continues to be longitudinally stable.

Table 4.2. Post-Drop Cruise Trim Conditions

Throttle	33.3%
Thrust	156 [N]
Elevon Deflection as Elevator	1.85 [deg]
Angle of Attack	1.2 [deg]
Airspeed	50 [m/s]

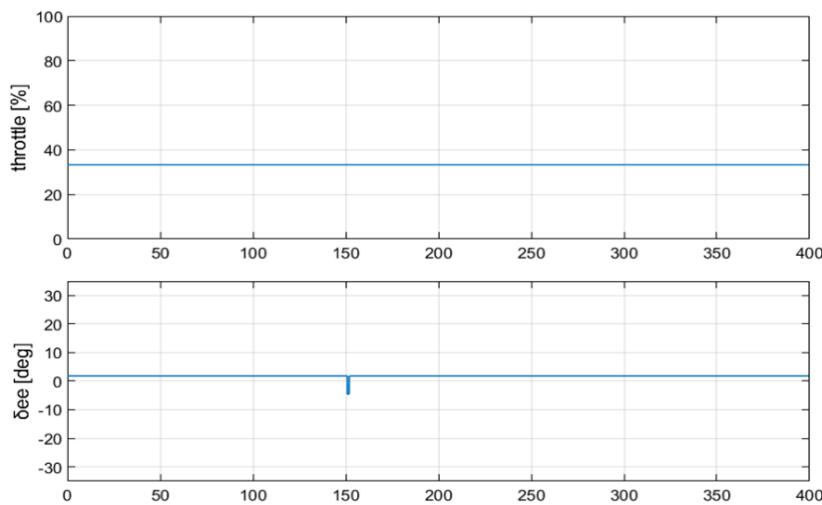


Figure 4.7. Throttle and Elevon Deflection as Elevator for Post-Drop Cruise

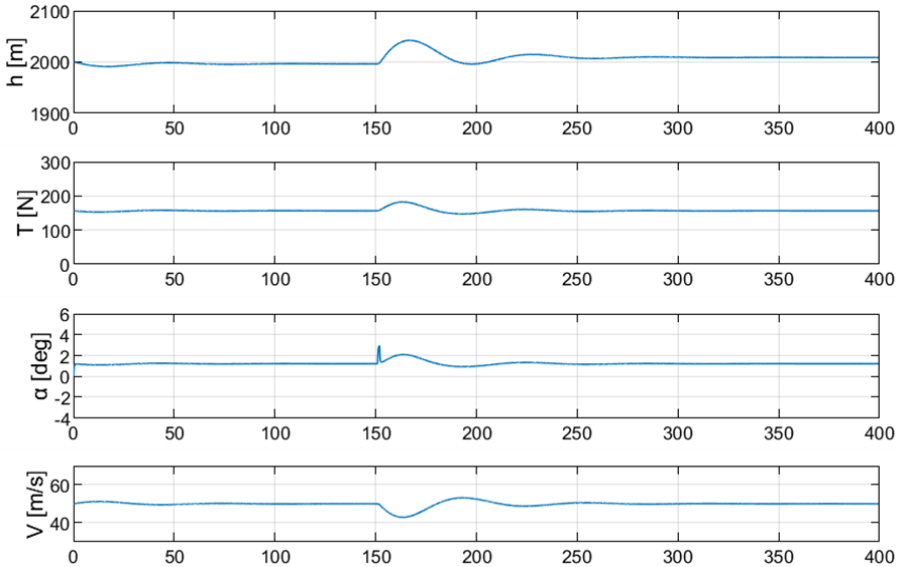


Figure 4.8. Trim Conditions for Post-Drop Cruise

Take-off

The following graphs refer to the start of the mission, when the aircraft takes-off from the runway and then climbs to the cruise altitude of 2 km. The aircraft is aligned with the runway and, by maximizing throttle, it starts accelerating. A -9.8 degrees deflection on both elevons is applied. Throttle and elevon inputs are shown in **Figure 4.9**. When the essential velocity is reached, the aircraft takes-off and starts a trimmed climb.

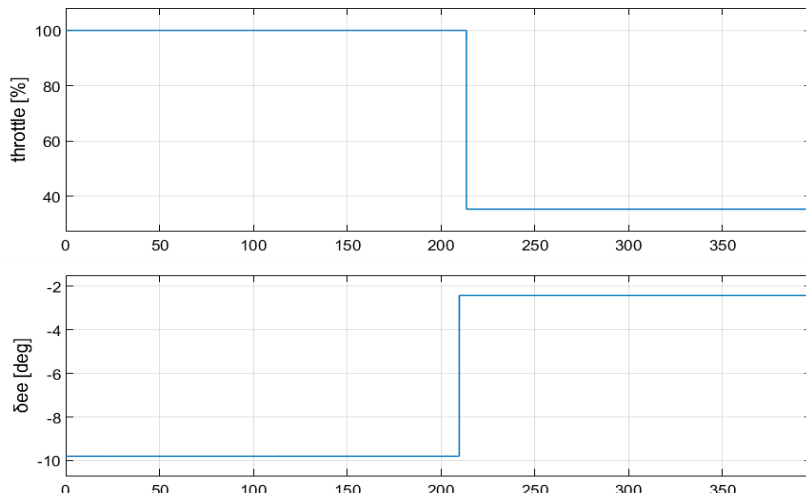


Figure 4.9. Throttle and Elevon Deflection as Elevator for Take-off, Climb and the Start of Cruise

From **Figure 4.11**, it becomes clear that a runway of at least 150 meters length is needed. The essential velocity for the aircraft to leave the ground is 38 m/s. The difference from 0 in the aircraft's altitude while it touches the ground is due to the FlightGear's ground elevation, since the runway is not at sea level.

In **Figure 4.12**, the whole climb is presented, until the aircraft reaches the cruise altitude, when the trim inputs change to the ones given in the cruise subchapter. The aircraft climbs in full thrust, with a climb rate of approximately 600 m/min, an angle of attack of 8 degrees and a mean velocity of 35 m/s. Thrust at the start of the climb is stabilized at 1000 N and decreases as the aircraft gains altitude. This is due to the loss

of effectiveness of the propeller with decreasing air density. Finally, the pitch angle θ is presented in **Figure 4.13**. As for the oscillation at the start of the cruise phase, it is due to the step change in elevon deflection and throttle. The oscillation in all variables damps, meaning that the aircraft is statically and dynamically stable.

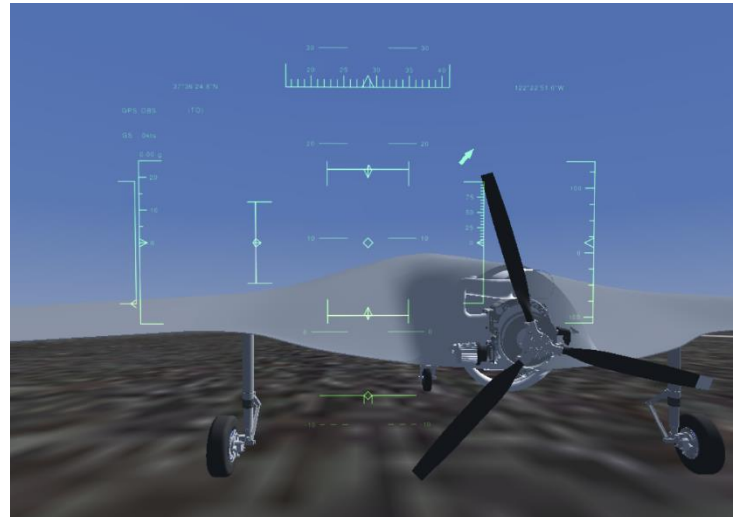


Figure 4.10. The DELAER RX-3 Taking-off

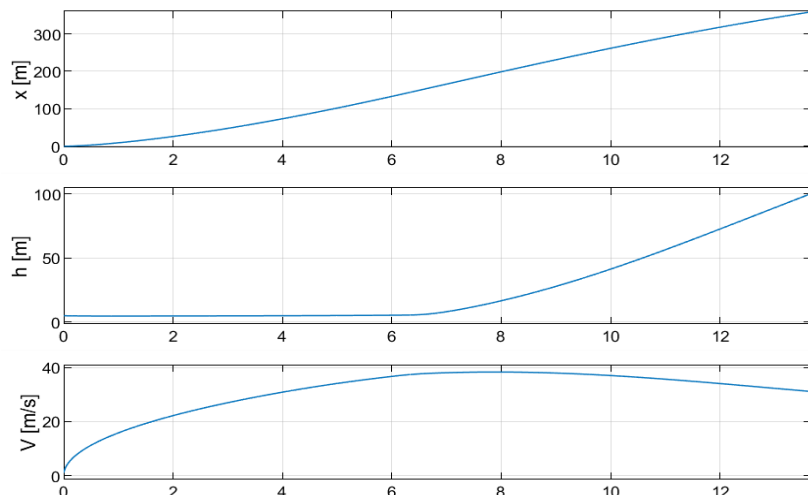


Figure 4.11. Take-off Characteristic Variables

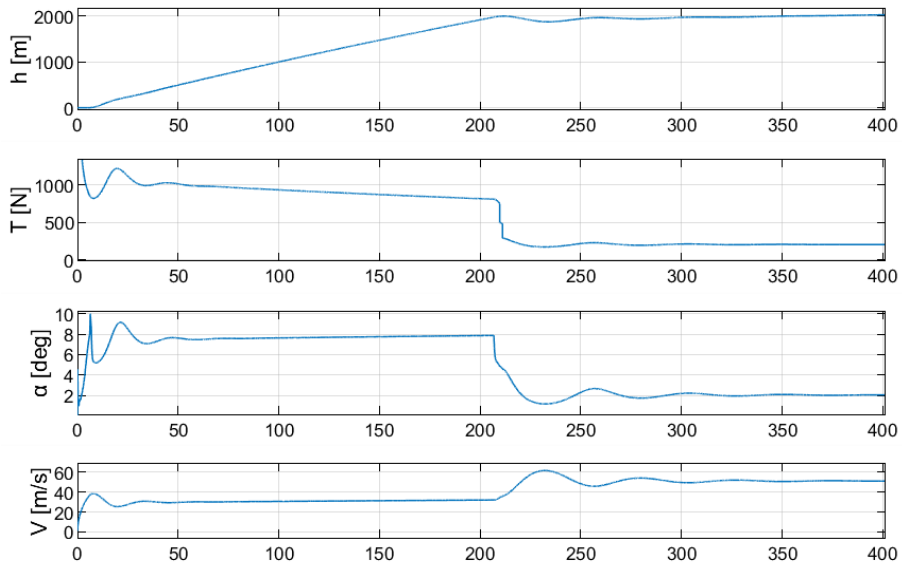


Figure 4.12. Trim Conditions for Climb and the Start of Cruise

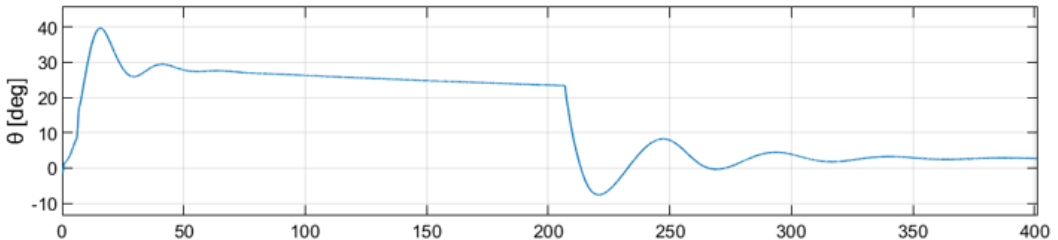


Figure 4.13. Pitch Angle for Take-off, Climb and the Start of Cruise

Payload Drop

The DELAER RX-3's mission profile includes the provision of isolated territories and islands with lifesaving supplies and dedicated equipment, via aerial delivery. In order to drop the payload, the aircraft descends from its cruise altitude to a lower, more appropriate height. It then continues on a new straight level flight at the new altitude and drops the carrying payload at a predetermined point. Since the payload mass is removed from the total aircraft mass, the aircraft undergoes a number of changes. These changes include the reduction of its weight, the relocation of its CG further aft, and new values of its moments of inertia. Since the CG approaches the AC, the platform's stability decreases, meaning that this new state needs to be tested and new trim conditions need to be found. After the drop, the aircraft continues its trimmed flight for a short time and finally climbs back to the cruise altitude. The results are presented below, including descent, drop and climb.

In **Figure 4.14**, the values for throttle and elevon deflection are given, resulting to the corresponding values for the rest of the variables in **Figure 4.15**. Starting from the pre-drop cruise inputs, with a decrease in both of them, the aircraft begins descending. Then an intermediate small change in elevon deflection is applied, followed by the trim value for the new low altitude straight level flight, so that the transition is smoother. A straight transition to the new trim deflection was also tested, leading to the aircraft stalling, since the increase in angle of attack exceeded the limit.

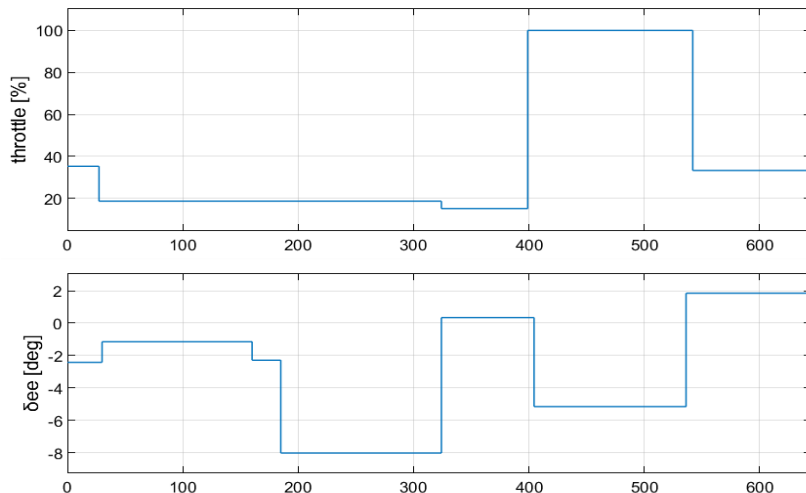


Figure 4.14. Throttle and Elevon Deflection as Elevator for Payload Drop Case

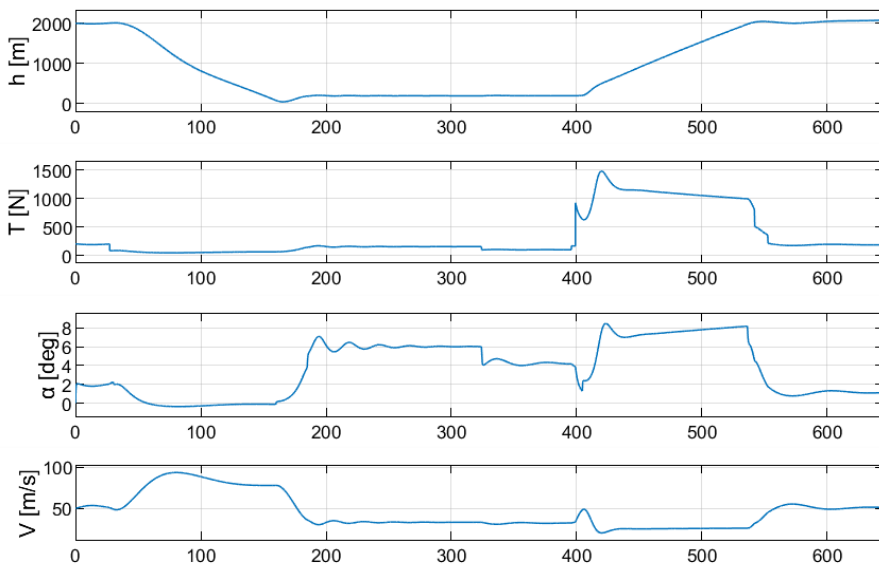


Figure 4.15. Trim Conditions for Payload Drop Case

As for the payload drop specifically, the following tables and graphs give a more detailed description. After the descent, the aircraft stabilizes in the new trim conditions. It then begins flying in equilibrium until it reaches the drop point, where it releases the carrying payload. The drop time is at 325 seconds and the aircraft undergoes the following changes.

Table 4.3. Aircraft Changes due to Payload Drop

	Pre-Drop	Post-Drop
Mass	246.3 [kg]	201.3 [kg]
x_{CG} (from nose)	1.897 [m]	1.9805 [m]
I_{xx}	286.874 [kgm^2]	286.825 [kgm^2]
I_{yy}	134.257 [kgm^2]	126.526 [kgm^2]
I_{zz}	403.862 [kgm^2]	396.15 [kgm^2]

Table 4.4. Pre-Drop and Post-Drop Trim Conditions

	Pre-Drop	Post-Drop
Throttle	18.65 %	15.1%
Thrust	161 [N]	107 [N]
Elevon Deflection as Elevator	-8 [deg]	0.35 [deg]
Angle of Attack	6 [deg]	4.2 [deg]
Airspeed	33 [m/s]	32 [m/s]

From **Tables 4.3** and **4.4**, it is clear that the changes due to payload drop affect the trim conditions notably. The relocation of the CG more aft creates the need for positive trim elevon deflection. Additionally, these changes cause a positive pitching moment, which results to a

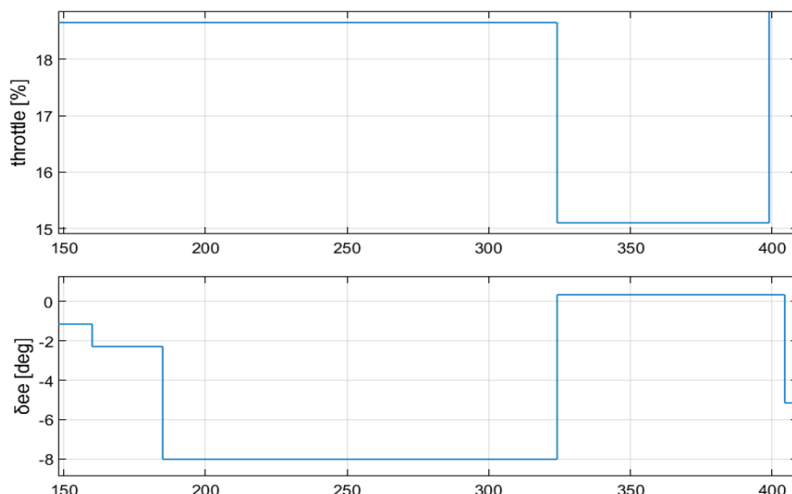


Figure 4.16. Throttle and Elevon Deflection as Elevator Before and After Drop

“nose-up” motion, leading to the oscillation seen in **Figure 4.17**. After stabilizing to the post-drop trim conditions, the aircraft continues on another short straight level flight and finally starts climbing back to the cruise altitude in full throttle.

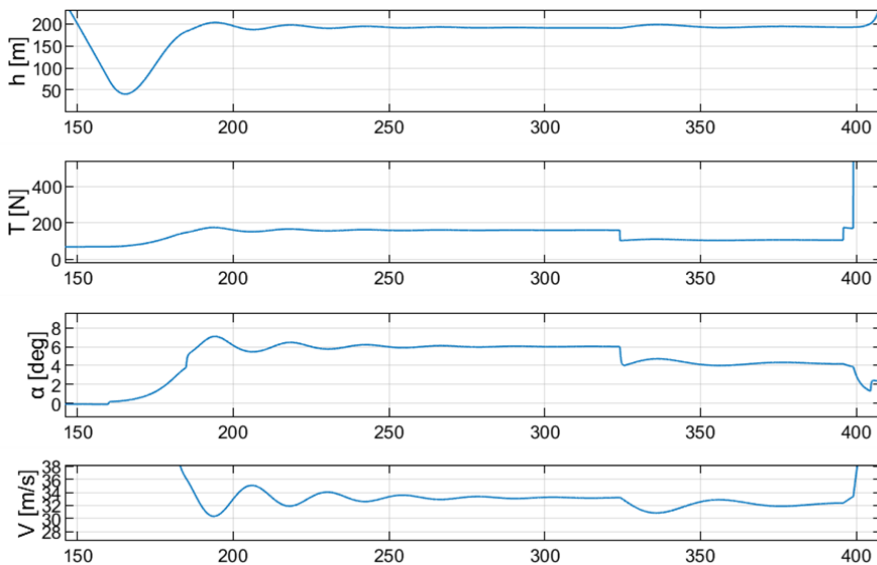


Figure 4.17. Trim Conditions Before and After Drop

Landing

The following graphs present the last part of the mission. The aircraft starts descending from the cruise altitude and approaches the landing runway. At various points during descent, the

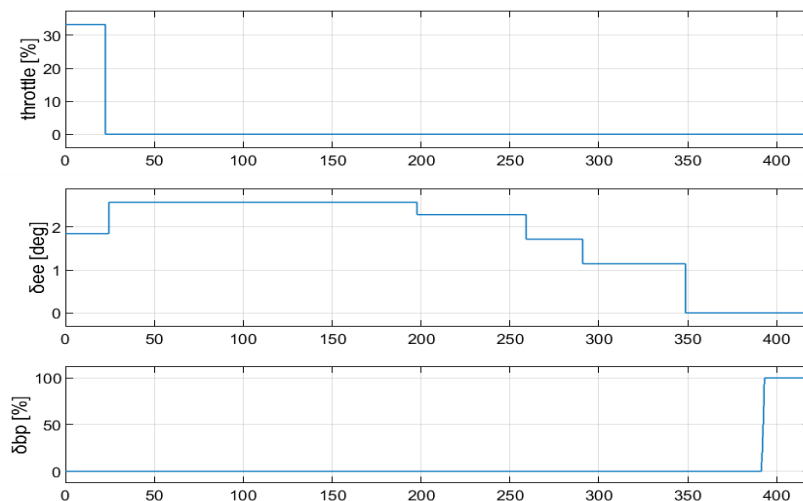


Figure 4.18. Throttle, Elevon Deflection and Brake Pedal Deflection for Descent and Landing

elevon deflection increases in order to decelerate the aircraft and increase its angle of attack to appropriate for landing values. When the airplane touches the ground, the maximum brake pedal deflection is applied via the brake slider, until the airplane is immobilized.

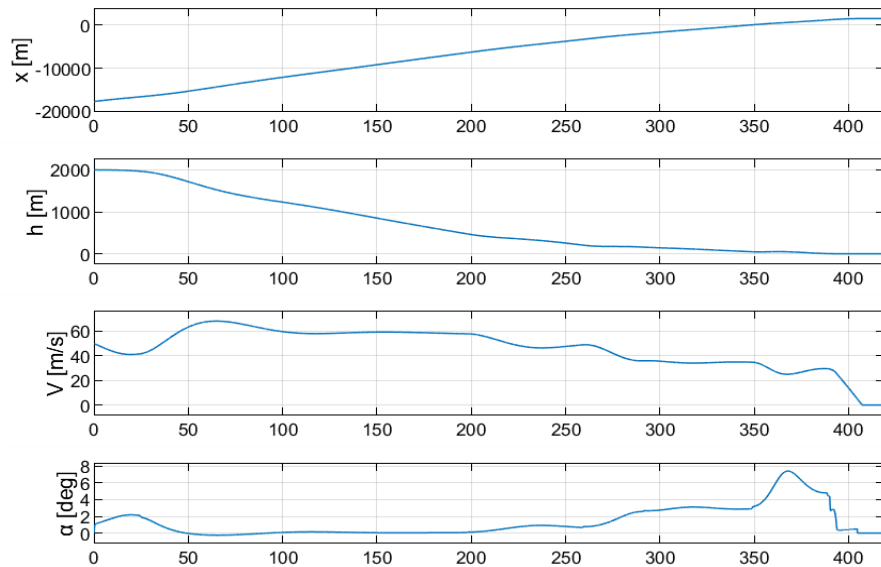


Figure 4.19. Position, Velocity and Angle of Attack for Descent and Landing

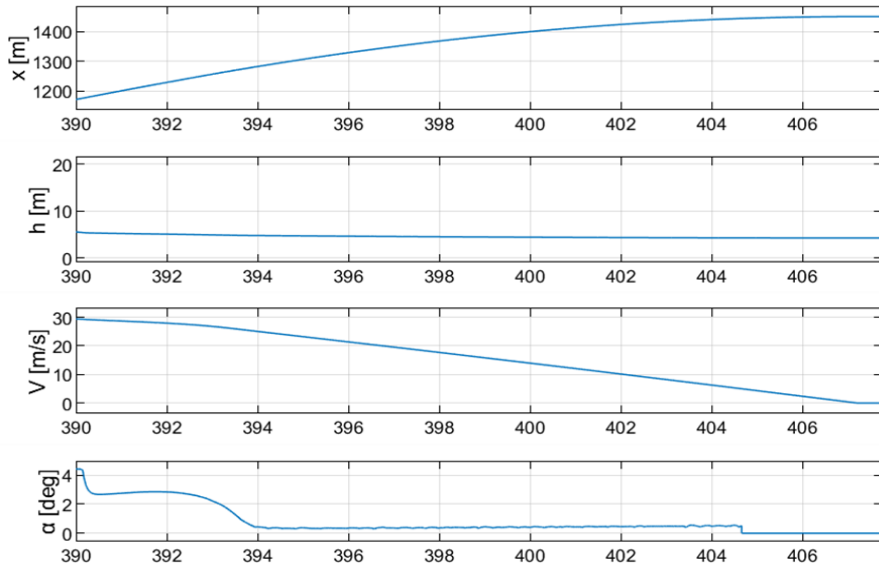


Figure 4.20. Figure 4.19 from Touchdown to Immobilization

As shown in **Figure 4.20**, the aircraft lands with an angle of attack of 4.2 degrees. The main wheels touch the ground first, applying a negative pitching moment, which forces the nose to drop, reducing angle of attack, until the front wheel lands too. The duration between the touchdown and the aircraft immobilization is 17 seconds and the distance travelled during this time is 270 meters. When the aircraft's altitude decreases to the length of its wingspan, which in this case is 7.146 m, ground effect occurs, increasing lift force. This effect is shown in **Figure 4.21**. Lift force is increased by an order of 10%.

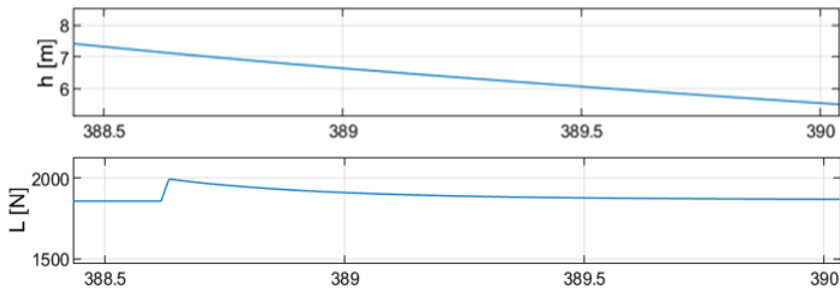


Figure 4.21. Ground Effect

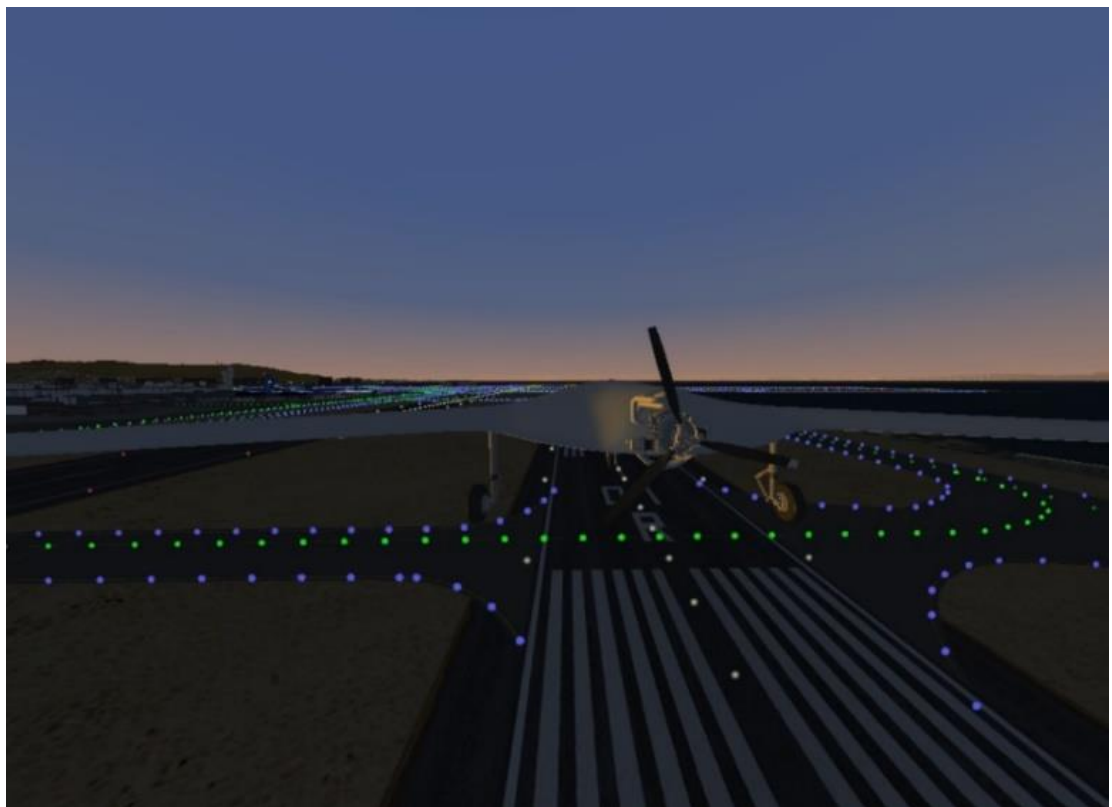


Figure 4.22. The DELAER RX-3 Approaching the Landing Runway

Wind Effect

The Atmosphere and Wind Model is able to simulate the effect of the wind on the aircraft. More specifically, the effects of wind shear, wind turbulence and discrete wind gusts are presented in the following graphs.

The first case consists of the combination of a north wind field, including wind turbulence plus the application of a wind gust. The wind characteristics are given in **Table 4.5**. Velocity is determined for an altitude of 6 m and increasing with altitude due to the wind shear.

Table 4.5. Wind Characteristics

	Wind Field	Discrete Gust
Velocity (at 6 m altitude)	5 [m/s]	20 [m/s]
Direction	From North	Towards y_B -axis
Length	-	100 [m]
Starting Time	0 [s]	100 [s]

The side wind gust acts as a lateral disturbance, leading to a spiral descent (**Figure 4.23**), similarly to the case of the aileron deflection. This time the aircraft path is less smooth, due to the presence of the north wind field, which acts as a headwind, a tailwind or a sidewind, depending on the aircraft's orientation. For instance, when the aircraft points towards north, the wind acts as a headwind, increasing the aircraft's airspeed, which translates to a gain in altitude, or in the case of descent, a decrease in the rate of descent.

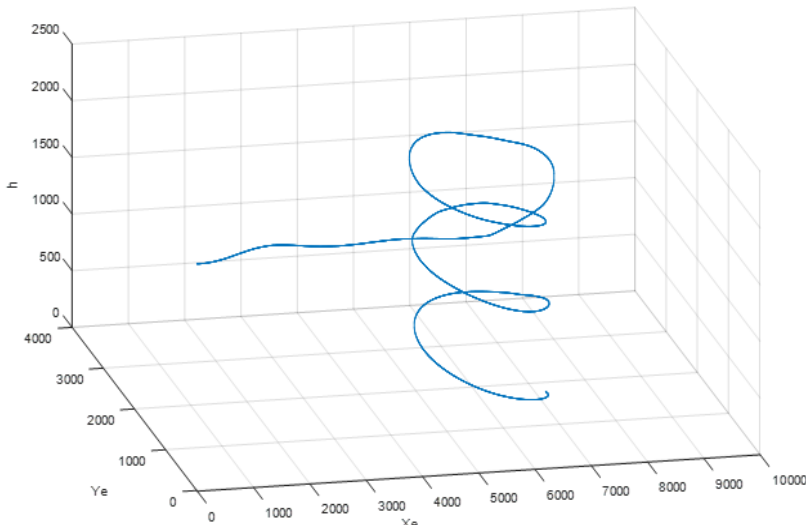


Figure 4.23. Spiral Descent due to Side Wind Gust (graph Y-axis is opposite to the simulation Y-axis)

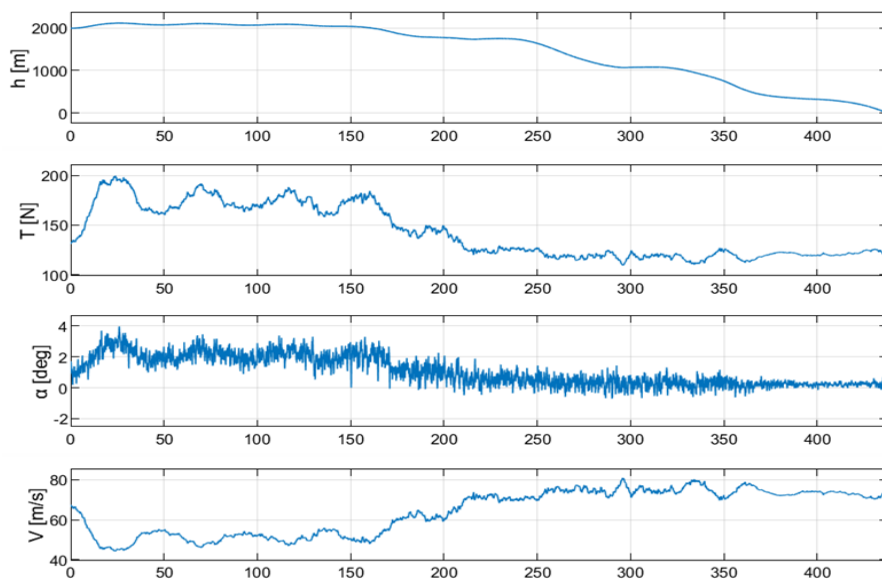


Figure 4.24. The Effect of Wind on Cruise

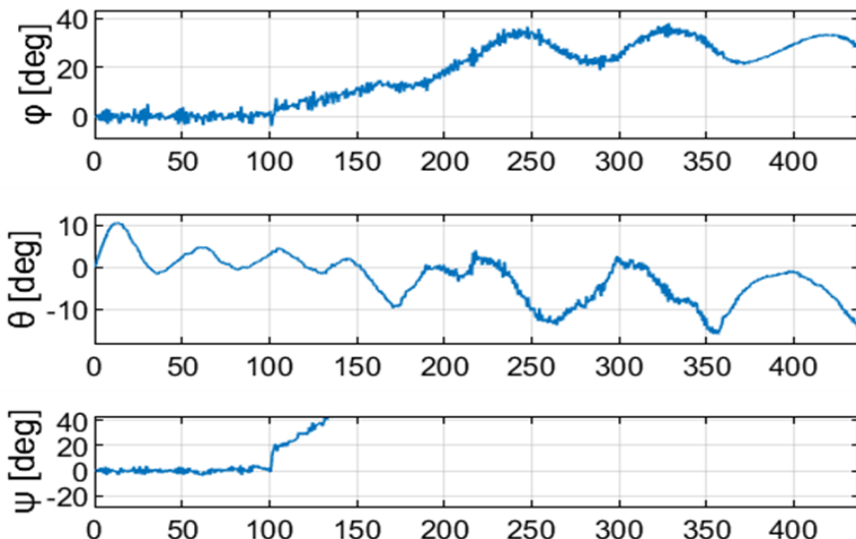


Figure 4.25. The Effect of Wind on Aircraft Orientation

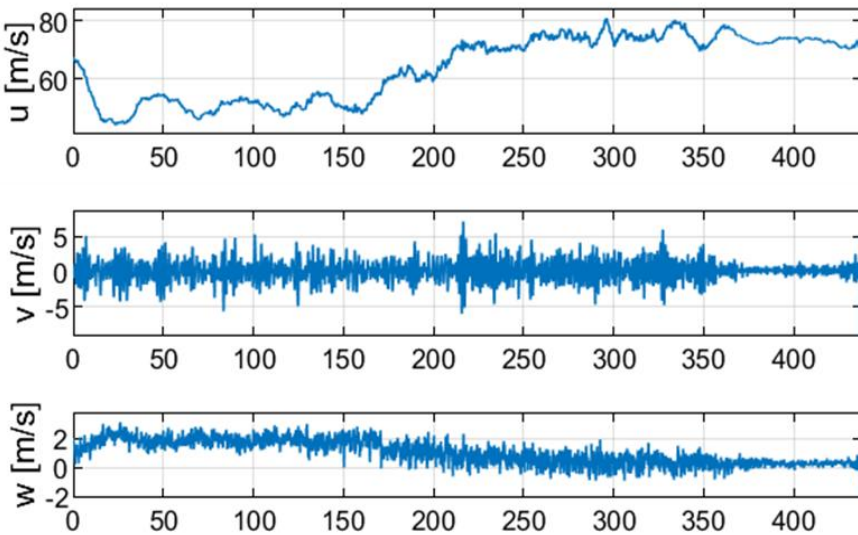


Figure 4.26. The Effect of Wind on Aircraft Body Velocity Components

From the series of figures above, it is clear that the wind turbulence acts on all three axes, and its amplitude is random during the simulation. However, apart from the small disturbances, the aircraft is stable, with all variables having a mean value similar to the corresponding one in absence of wind. Additionally, when the aircraft loses height, the effect of wind shear is clearer, with the wind's velocity amplitude decreasing, following the shape of **Figure 2.19**.

The next case refers to the differences between a headwind and a tailwind. A headwind is a wind blowing to the opposite of the aircraft's direction. This means that the headwind's velocity is added to the aircraft's airspeed. On the contrary, a tailwind "hits" the aircraft from tail to nose, meaning it has the same direction with the aircraft. In this case the wind's velocity is subtracted from the aircraft's airspeed.

The same wind characteristics are applied, as in the previous case, apart from the side wind gust, which is substituted by the headwind gust and the tailwind gust accordingly.

Table 4.6. Wind Characteristics

	Wind Field	Headwind Gust	Tailwind Gust
Velocity (at 6 m altitude)	5 [m/s]	20 [m/s]	20 [m/s]
Direction	From North	From x_B -axis	Towards x_B -axis
Length	-	200 [m]	200 [m]
Starting Time	0 [s]	50 [s]	50 [s]

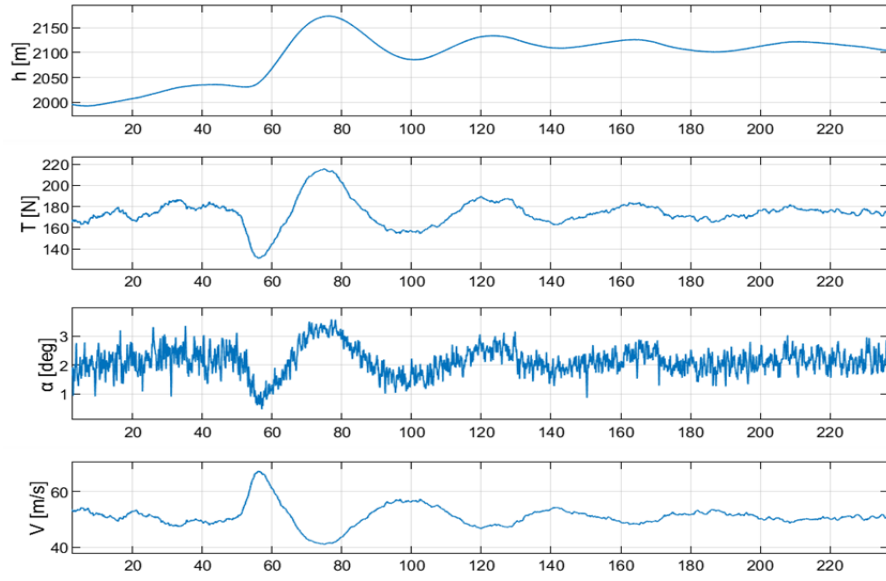


Figure 4.27. The Effect of a Headwind Gust

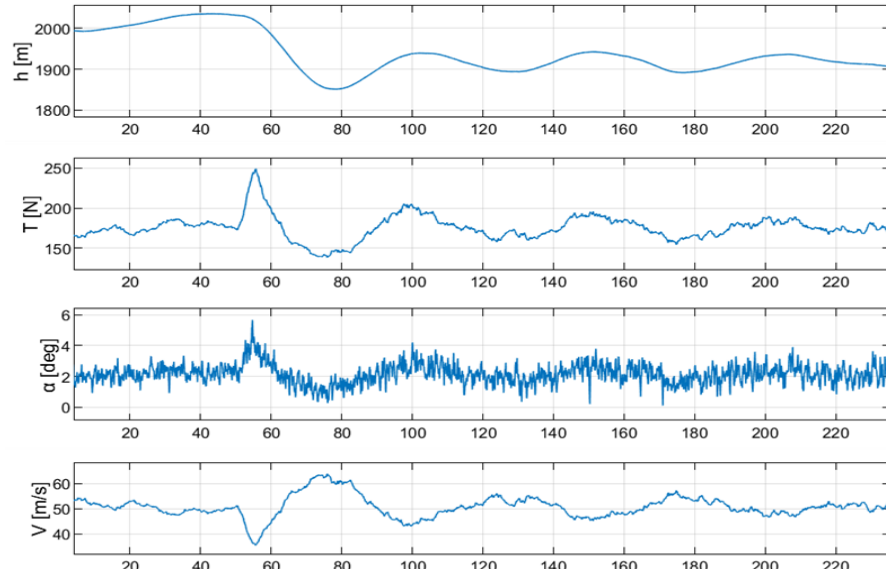


Figure 4.28. The Effect of a Tailwind Gust

Looking at **Figures 4.27** and **4.28**, the difference is obvious. Both wind gusts start at 50 seconds in the simulation and build up in the next few seconds. In the headwind case, the aircraft's airspeed increases while the gust builds up. Then the kinetic energy gained from the headwind is exchanged with an increase in altitude, with the airspeed returning back to its starting mean value of 50 m/s. As for the tailwind, it has the opposite effect, with the airspeed decreasing, resulting to loss of height.

Leading-Edge Vortices

Comparison of the Experimental and Computational Outputs

Regarding the wingtip investigations, the streamwise velocity, normal velocity and axial vorticity curves of the CFD simulations as compared with the experimental ones are presented in **Figures 4.29, 4.30** and **4.31**. As a general observation, the results of the computational simulations are in agreement with the experimental measurement. The streamwise and especially the normal velocity component prediction is far better than the axial vorticity. As shown in **Figure 4.31** the computational models underestimate axial vorticity by a high degree. This deviation of the axial vorticity may be due to a weakness of the turbulence models to compute the velocity derivatives in the vortex region with high accuracy. The superiority of the Transition SST turbulence model, concerning the streamwise velocity can be observed in **Figure 4.29**. RSM and SA - RC have similar behavior, while Menter's SST appears to be the less appropriate for the case at hand. In terms of vorticity, the Transition SST proved to be worse, however, the difference between all models is relatively small. Regarding the plotting location, the lines pass through the point where the vorticity reaches its peak value, which coincides with the point where the streamwise velocity component takes its minimum value.

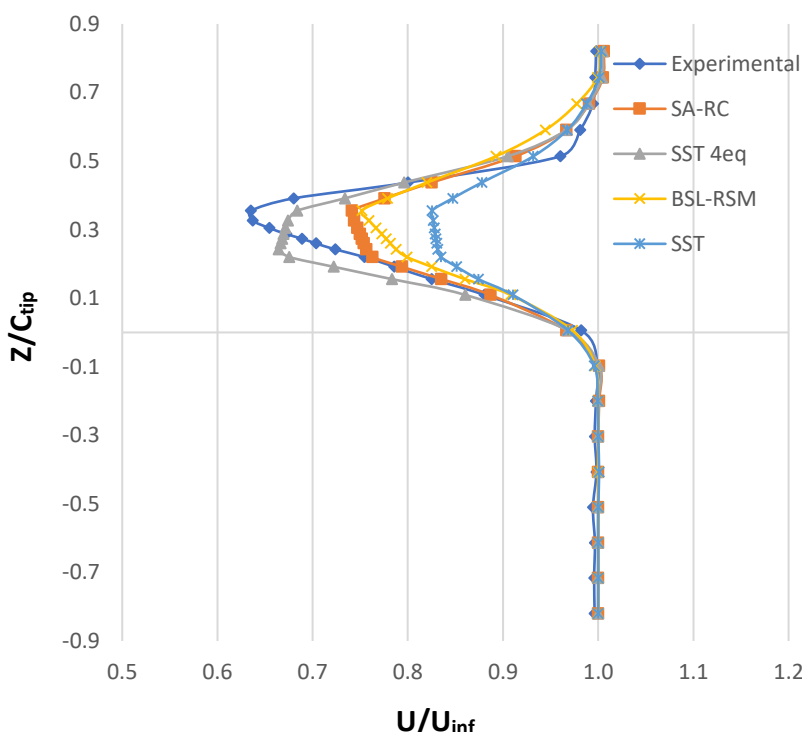


Figure 4.29. Line Plot of Streamwise Velocity Component at the Tip Vortex Plane

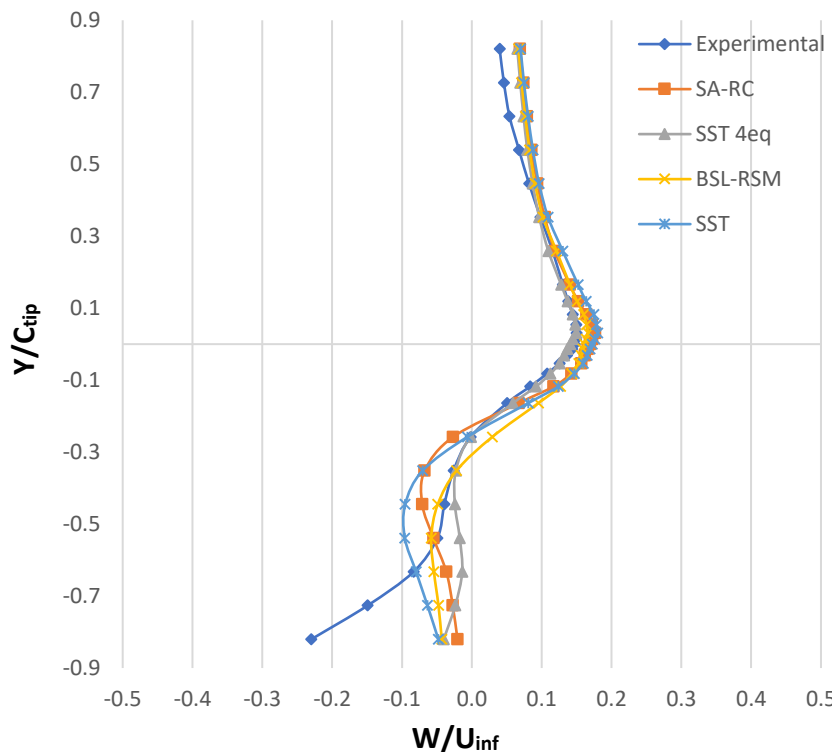


Figure 4.30. Line Plot of the Normal Velocity Component at the Tip Vortex Plane

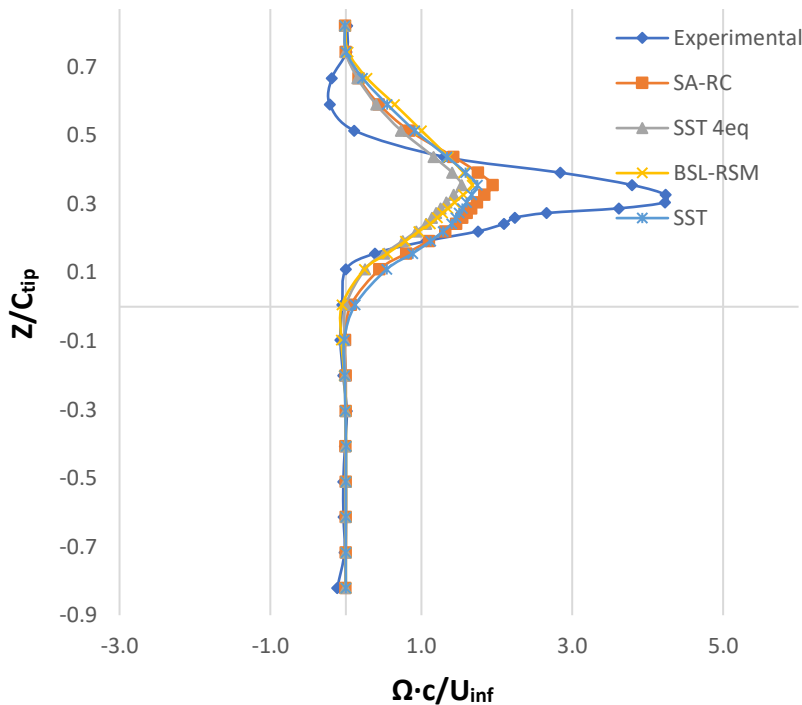


Figure 4.31. Line Plot of the Axial Vorticity Component at the Tip Vortex Plane

Moreover, the contour plots of the velocity components on the LEV plane and the tip vortex plane are illustrated in **Figures 4.32 to 4.35**, along with their minimum and maximum values. It should be noted again that the contour plots on the LEV plane begin 1.8 mm away from the model surface. As shown in **Figures 4.34 and 4.35**, there is a clearly defined vortical structure over the model, while the form of the contour plots compared to the experimental ones are almost identical. **Table 4.7** presents the absolute relative error (%) of the examined velocity components at the LEV and Tip Vortex planes, compared to the experimental outputs, for every turbulence model. Concerning the streamwise velocity component, the percentage error of its maximum value is smaller than 5% for each model. Its minimum value deviates as much as 22%, while the SA - RC and γ - Re_θ proved to be the worst. However, it can be seen that this deviation is due to the flow field far from the wingtip, closer to the wings' inboard region. Besides, **Figure 4.29** validates the accuracy of the SA - RC and γ - Re_θ models at the tip vortex region. Regarding the normal velocity component, the errors enlarge, especially on the LEV plane. In this case, the difference between the experimental and CFD computations is due to some outliers that appear near the boundary layer region. Therefore, it follows that turbulence models can't predict the normal velocity component in vortex regions as accurately as the streamwise ones.

Table 4.7. Percentage Errors of the Velocity Components Compared to the Experimental Results

Plane	Parameter	Limit	RSM	SST	SA - RC	γ - Re_θ
Tip Vortex	u/U_{inf}	min	0,63	7,66	20,78	21,41
		max	1,84	1,94	0,78	1,26
	w/U_{inf}	min	6,96	18,70	20,43	5,22
		max	5,45	6,36	64,09	54,09
LEV	u/U_{inf}	max	2,84	2,30	3,18	4,32
	w/U_{inf}	min	36,33	36,83	38,50	38,67
		max	83,50	85,25	76,25	74,25

A screenshot from the CFD analyses at the BWB configuration is indicatively shown in **Figure 4.36**, where the shear stress visualization over the platform is shown for an angle of attack of 10°, compared to the surface oil visualization results. It seems that γ - Re_θ illustrates the flow over the wing with the highest accuracy compared to the other models. More specifically, both the primary separation line (S1) and the primary attachment line (A1) can be detected, while their positions match exactly with the experimental ones. In the SA - RC model, these lines cannot be detected, whereas the RSM and SST capture the primary separation line adequately. Overall, taking into consideration all of the aforementioned results, the conclusion is that the γ - Re_θ model provides the most accurate results concerning the

developed vortices at the examined planes. Hence, this model should be used to simulate the vortical flow over the prototype geometry of the DELAER RX-3.

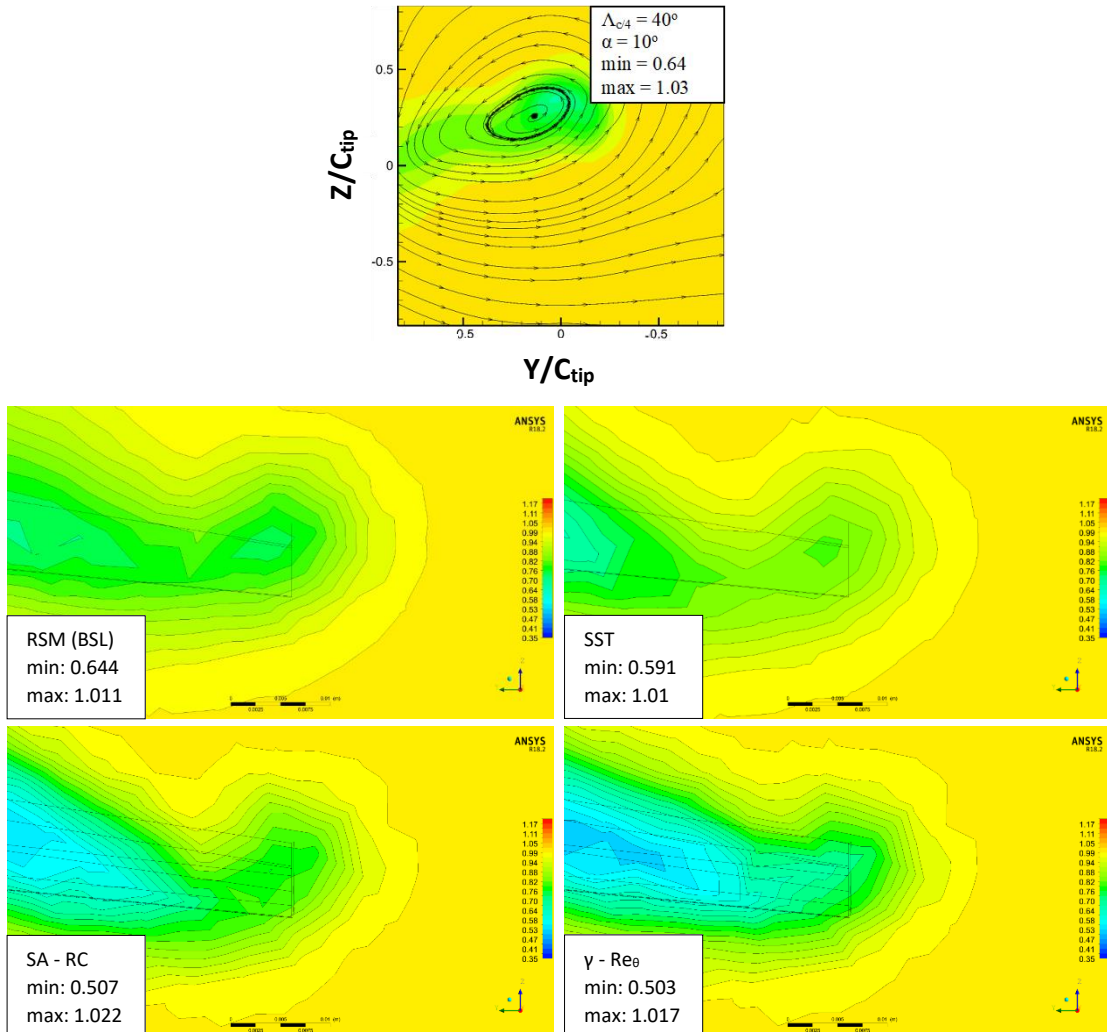


Figure 4.32. Comparison between the Contour Plots of the Streamwise Velocity Component at the Tip Vortex Plane

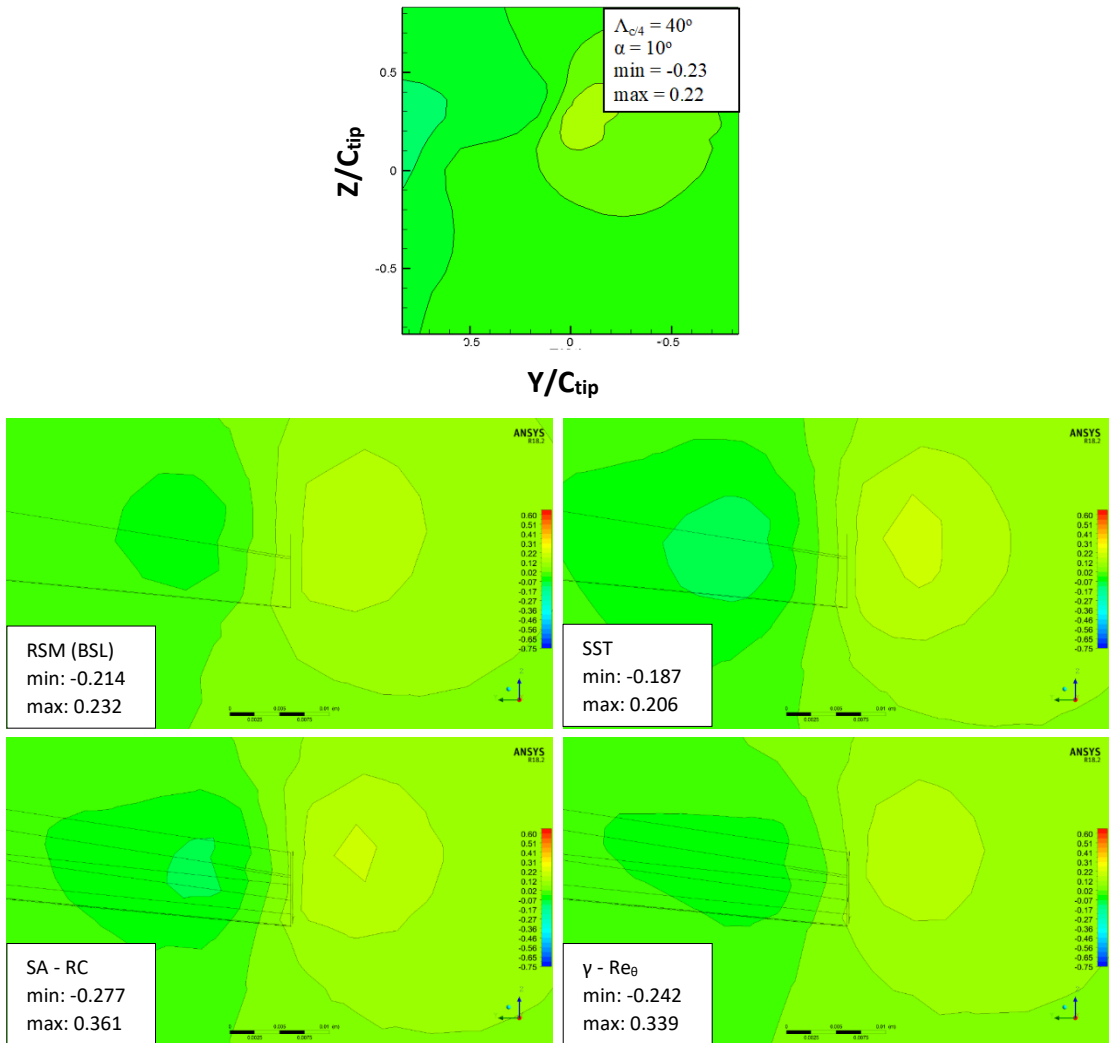


Figure 4.33. Comparison between the Contour Plots of the Normal Velocity Component at the Tip Vortex Plane

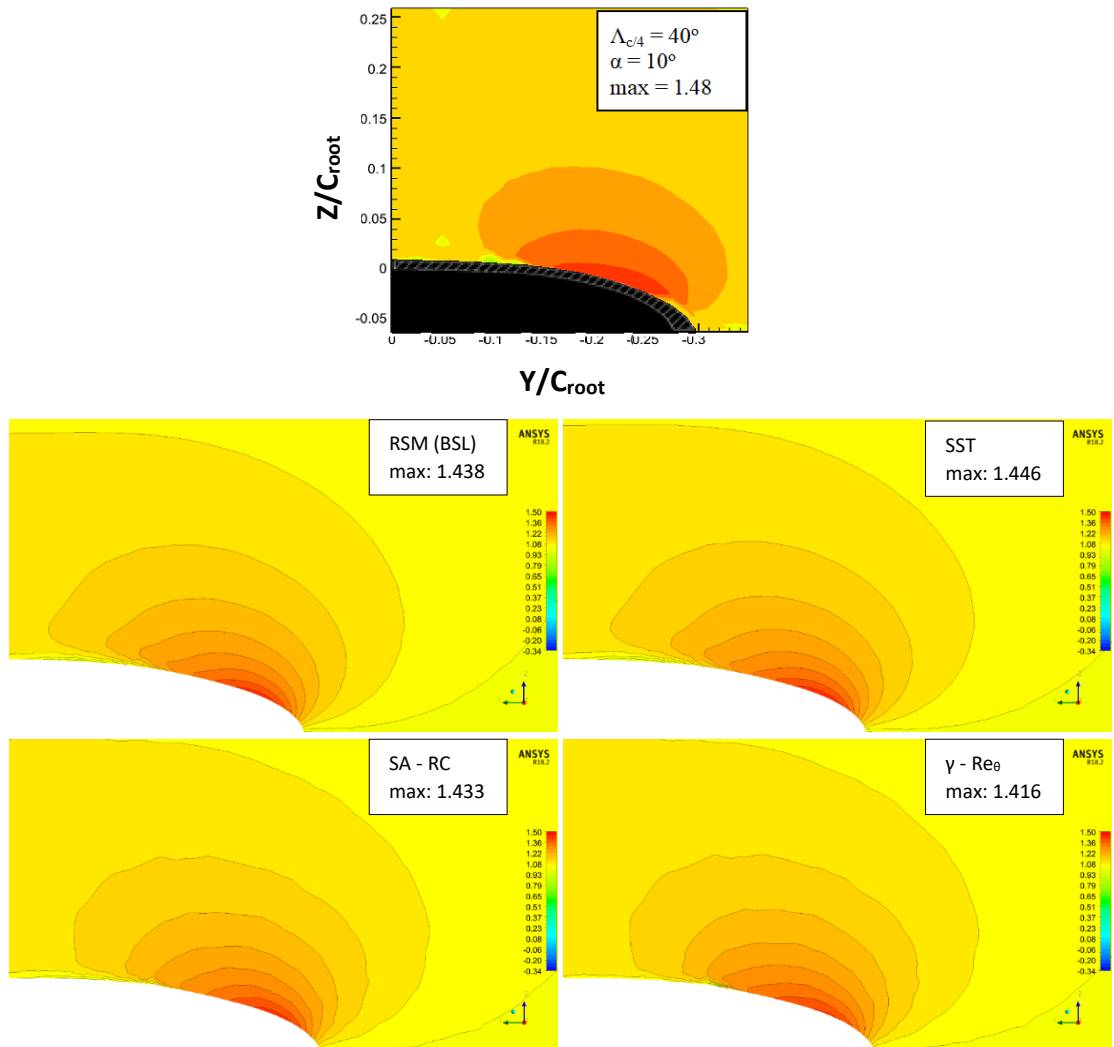


Figure 4.34. Comparison between the Contour Plots of the Streamwise Velocity Component at the LEV Plane

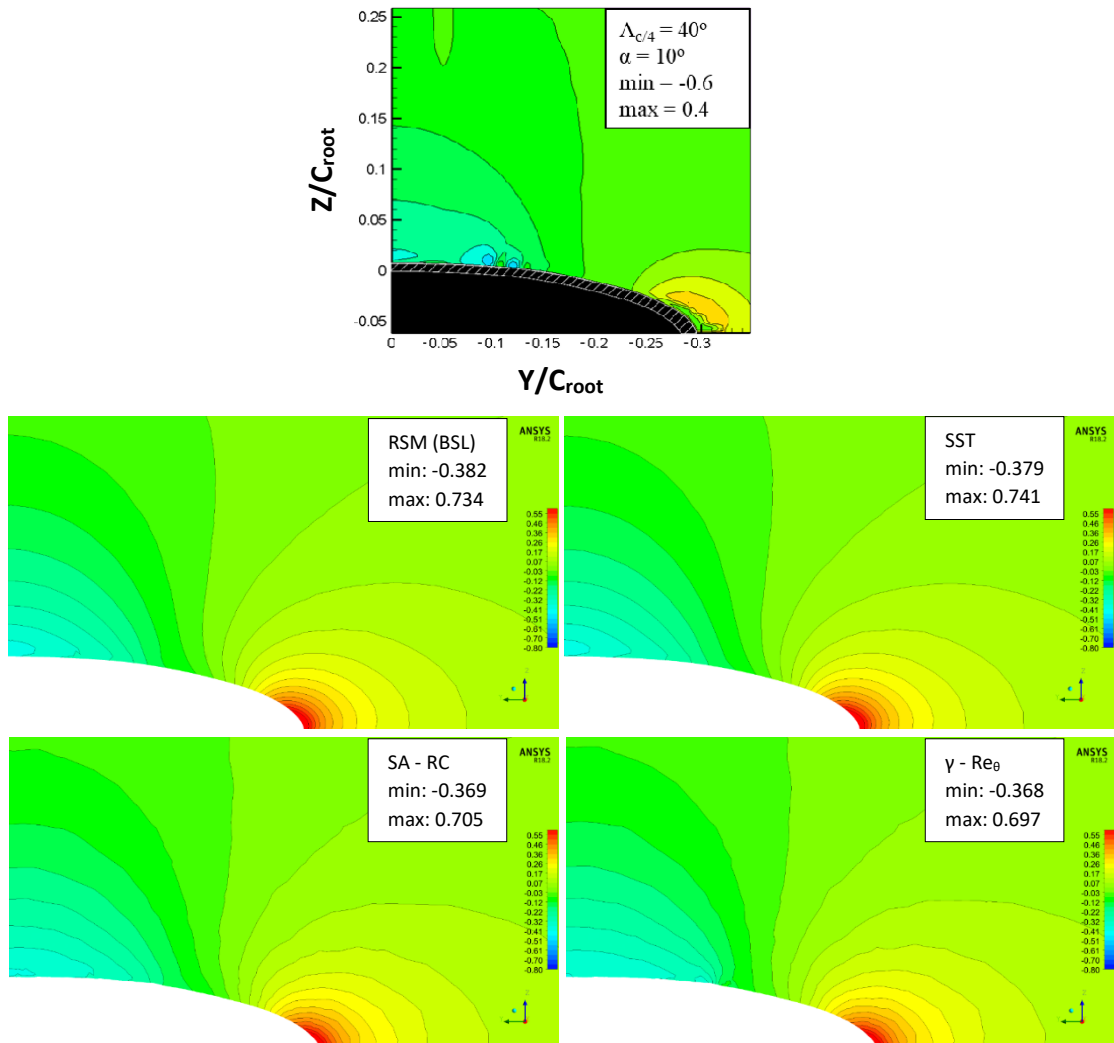


Figure 4.35. Comparison between the Contour Plots of the Normal Velocity Component at the LEV Plane

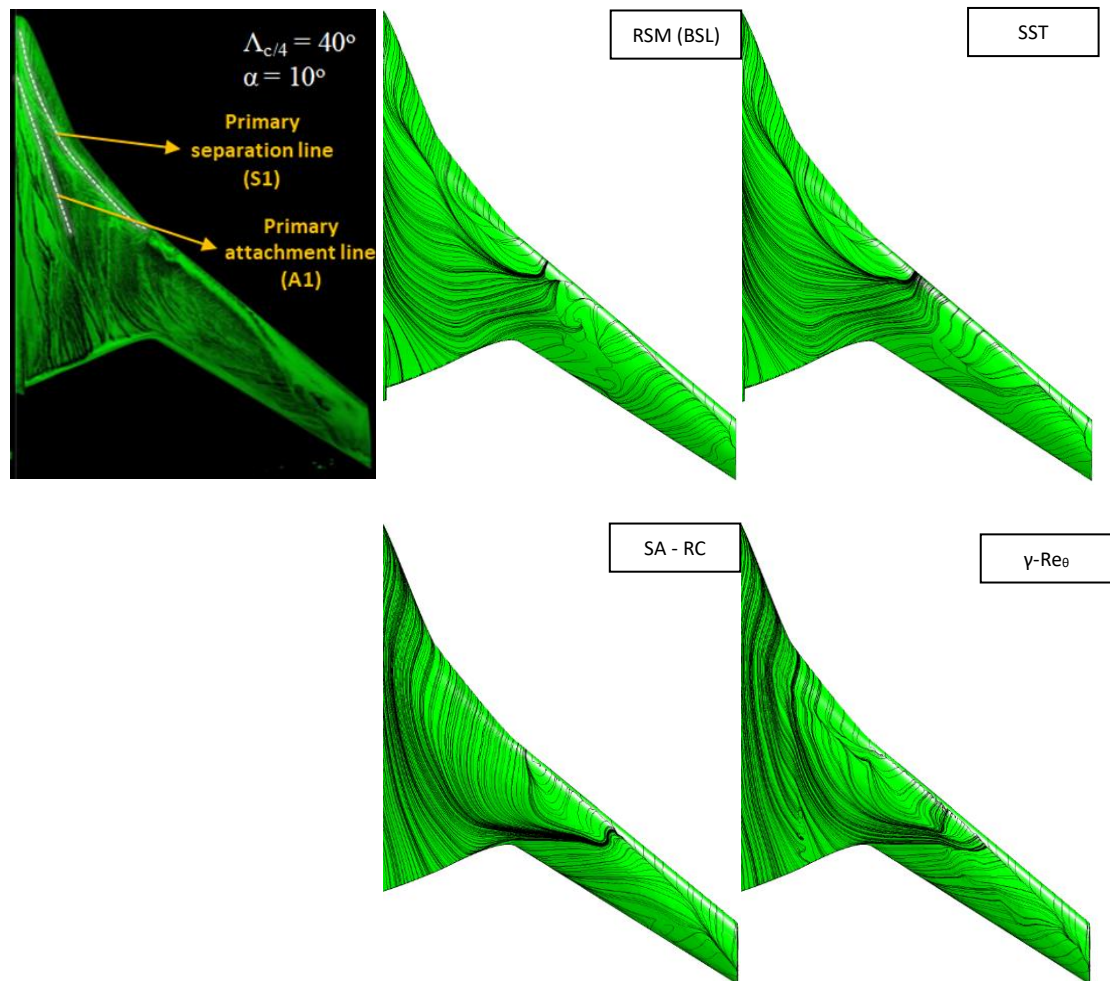


Figure 4.36. Surface Flow Visualization Comparison

The DELAER RX-3 geometry

The comparison of the four different turbulence models leads to the conclusion that the Transition SST (γ -Re θ) model is the most accurate for the simulation of vortical phenomena, as in the case at hand. Thus, this model was chosen for the conduction of CFD analysis on the DELAER RX-3 geometry. The first goal was to investigate the aircraft's performance, by extracting the forces and pitching moment coefficients in a range of angles of attack from -4° to 16° . These curves are presented in the following figures.

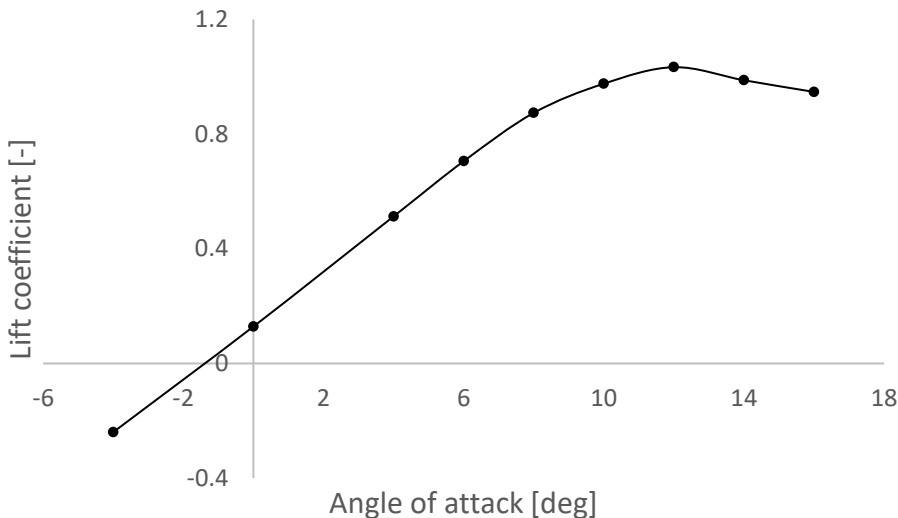


Figure 4.37. Lift Coefficient as a Function of Angle of Attack

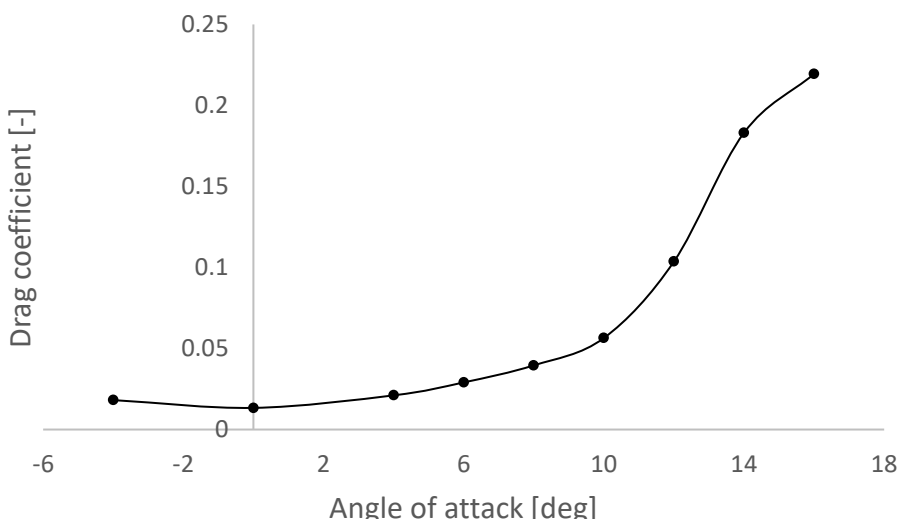


Figure 4.38. Drag Coefficient as a Function of Angle of Attack

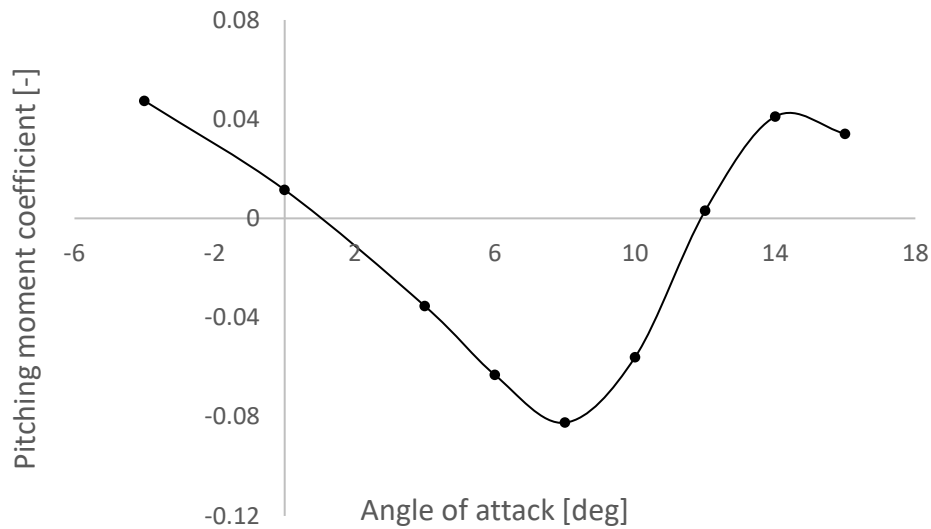


Figure 4.39. Pitching Moment Coefficient as a Function of Angle of Attack

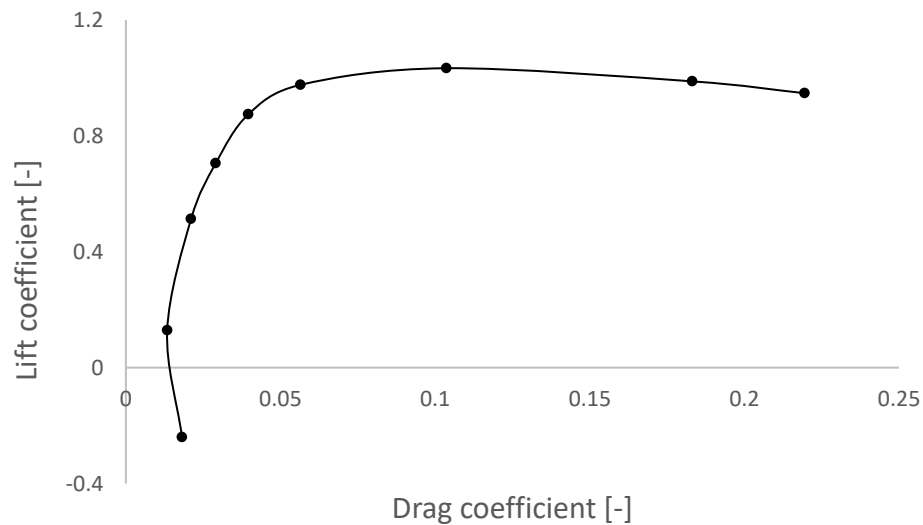


Figure 4.40. Drag Polar

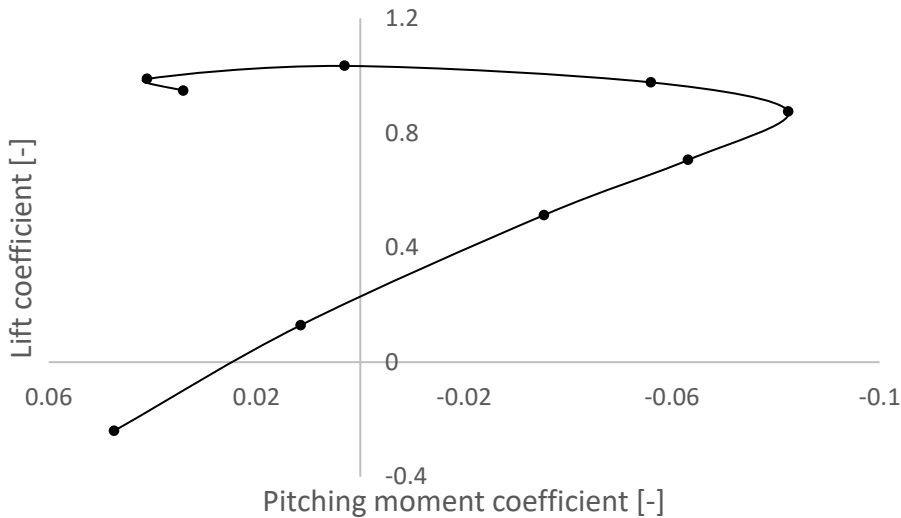


Figure 4.41. Lift Coefficient as a Function of Pitching Moment Coefficient

The evidence of the existence of Leading-Edge Vortices originates from the $C_m - \alpha$ curve, where there is a sudden increase in pitching moment after the angle of attack of 10° . Furthermore, the $CL - C_m$ curve indicates the so-called pitch break phenomenon. Finally, at 16° angle of attack, vortex breakdown occurs, leading to loss of lift at the wing's trailing edge

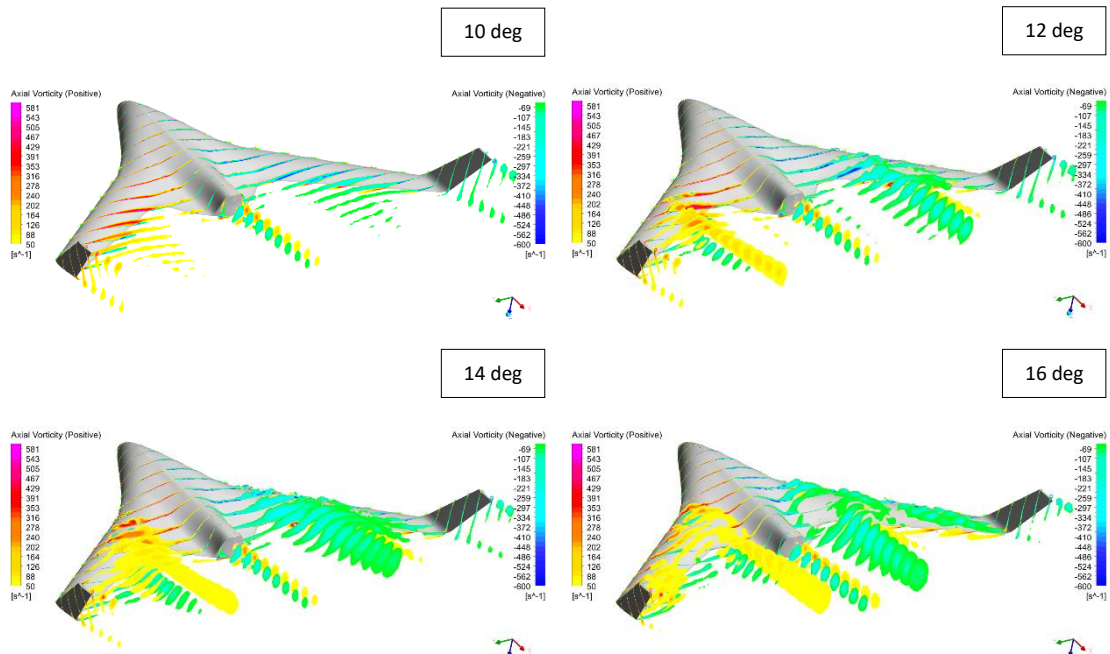


Figure 4.42. Axial Vorticity at various x/c Planes

and consequently to the wing stalling. Therefore, the visualization of the LEVs phenomenon was deemed essential, in order to validate theory and get a better understanding of the flow structure over the aircraft. Since the vortices' effects firstly appear at 10° , it was decided to study the range from 10° to 16° , in order to include the complete evolution of the phenomenon with the increasing angle of attack. In **Figure 4.42**, the vortical flow over the BWB is presented, using a series of axial vorticity contour plots, starting from the aircraft's nose and reaching up to 1 meter distance aft of the winglets. The flow structure over each wing consists of a 'dual' vortex, which appears at the kink region, where it also has its maximum vorticity value. The two vortices of this 'dual' vortical structure appear to have opposite circumferential directions, since the inner and higher one has a positive axial vorticity value, whereas the outer and lower one's axial vorticity is negative. This vortical flow behavior continues aft of the wing at the aircraft's wake region and diminishes as it moves backwards. It is clear that with the increasing angle of attack, the whole phenomenon becomes stronger and wider, while the vortices are moving inboard. The vortical flow is also visualized in **Figure 4.44** using 3D streamlines over the aircraft, colored by the local value of turbulence intensity, which is a variable strongly connected with vortical phenomena.

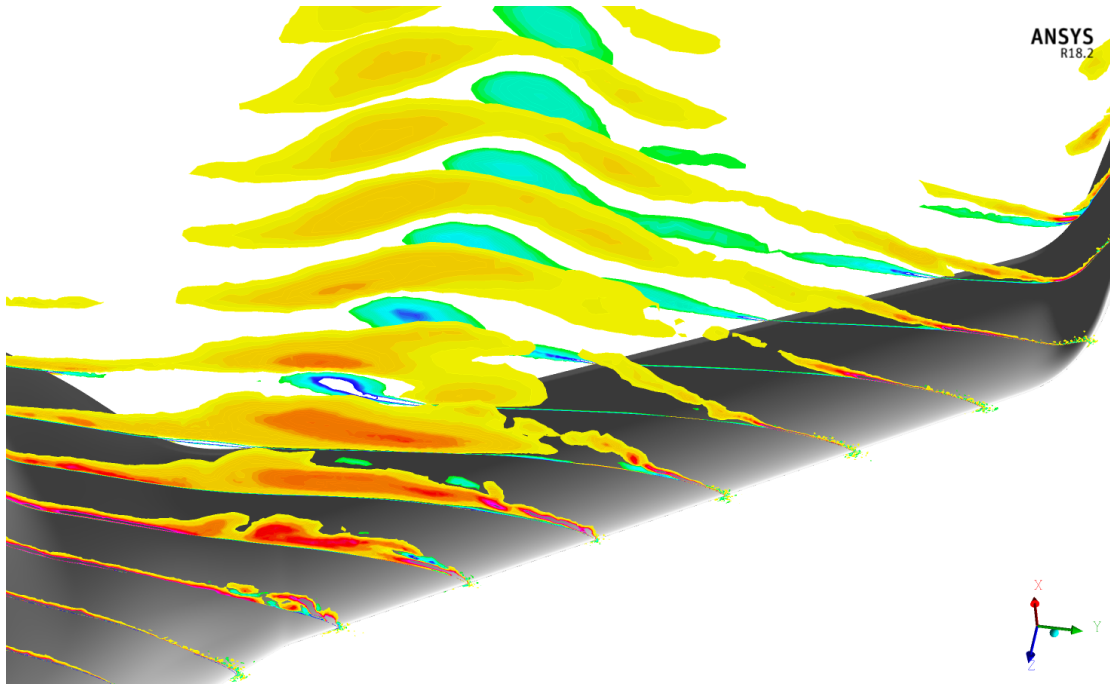


Figure 4.43. Dual vortex structure (Detailed view)

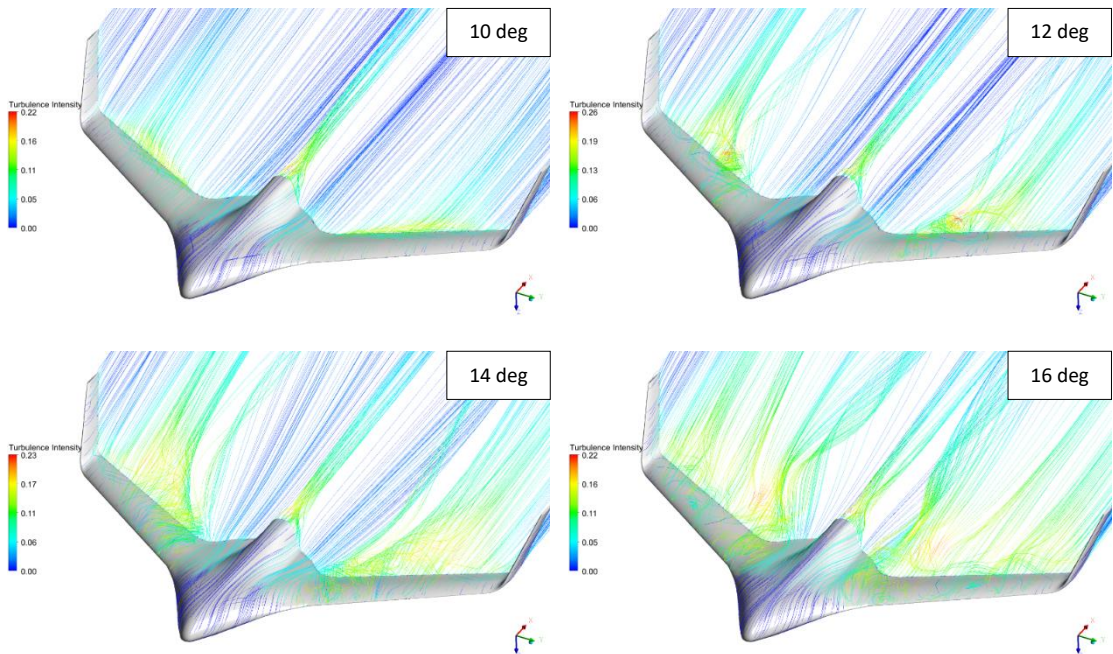


Figure 4.44. Streamlines over the Aircraft, colored by Turbulence Intensity

Additionally, surface flow visualizations were conducted, and the aircraft was colored according to the local pressure coefficient values. As shown in **Figure 4.45**, there is a clear match of the streamlines' behavior with the C_p values. With increasing angle of attack, the flow separation region enlarges, while at $\alpha=16^\circ$, vortex breakdown occurs and the main wing appears to be completely stalled.

As far as the vortex breakdown is concerned, it is depicted in **Figures 4.46** and **4.47**, in vorticity and pressure contours. The contours lie on the $x - z$ plane at the kink region, at 30% length of wing's span, where the main body blends with the wing, since this was the wing position where the vortices were the widest. At 10° and 12° there is still no flow separation, with the vorticity region gaining height but remaining attached on the wing. Then, at 14° , the vortical flow separates once and then is reattached on the wing. Then it separates again and is reattached further back on the wing, forming a much bigger separation bubble. Finally, at 16° , new separation bubbles are formed near the leading edge, with the previous ones moving further back and growing in size. This leads to the vortex breakdown phenomenon, with full separation of the flow at the aft part of the wing, resulting to the aforementioned loss of lift, and consequently wing stalling.

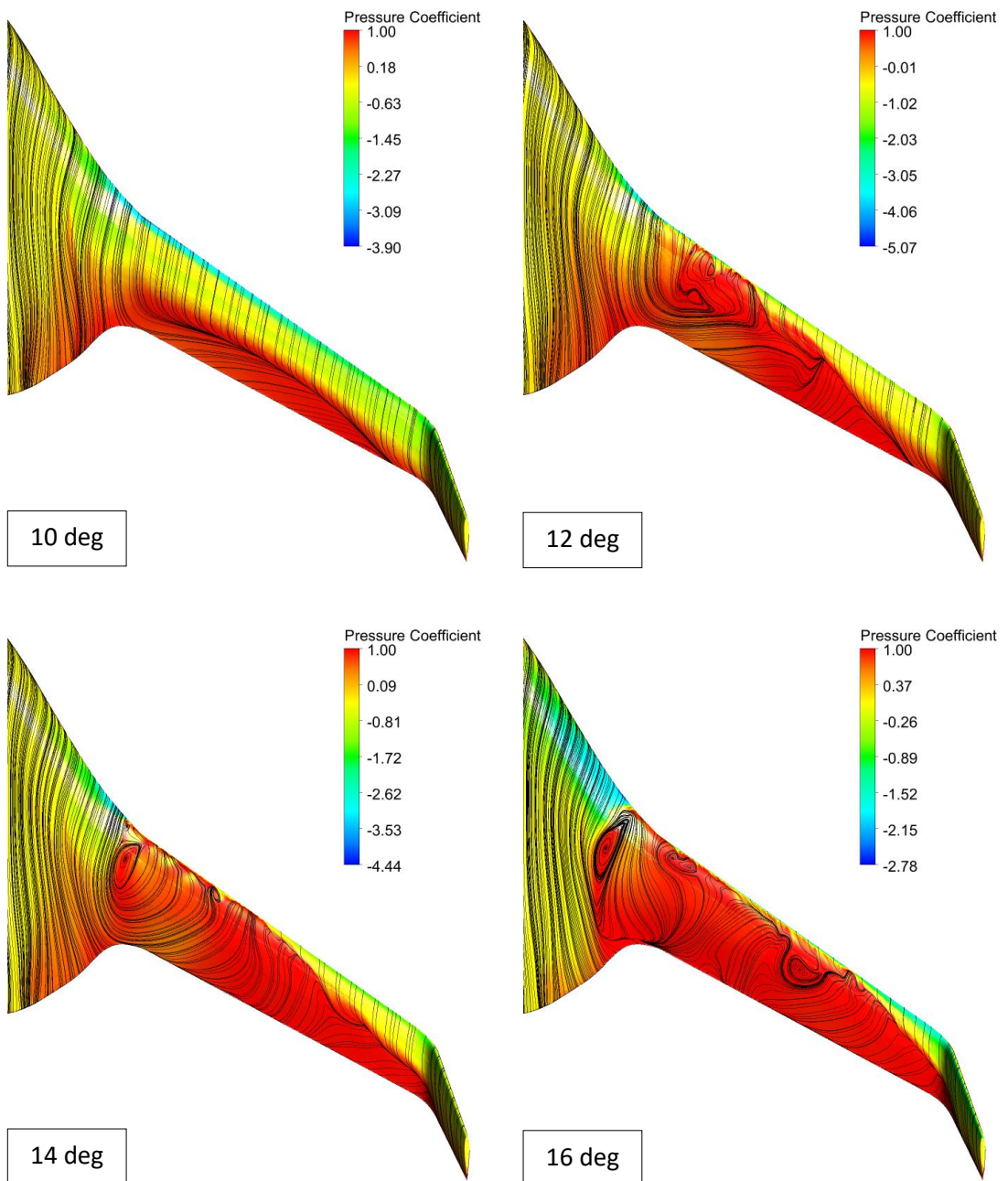


Figure 4.45. Surface Flow Visualization along with Pressure Coefficient

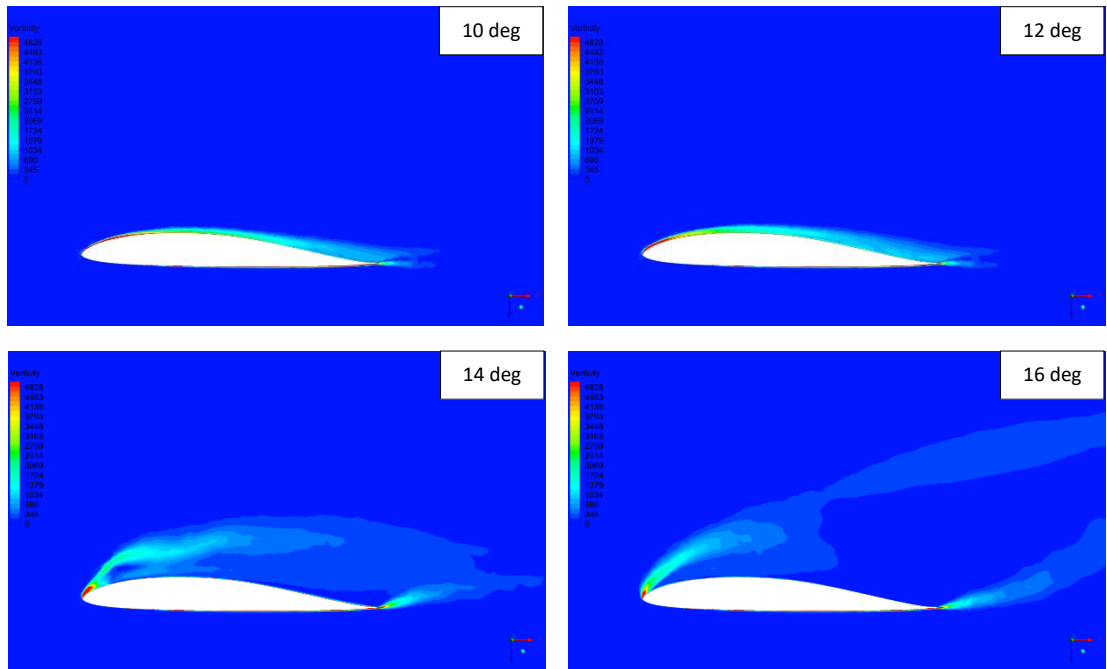


Figure 4.46. Contour Plots of the Vorticity Distribution at $y/s = 0.3$ (Kink Region)

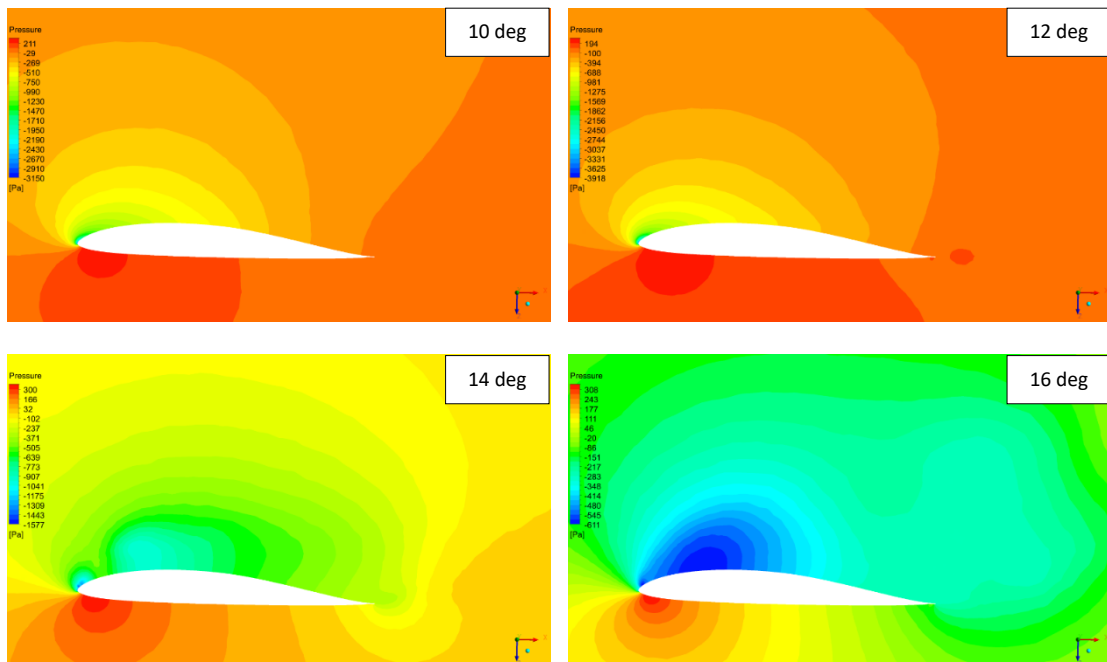


Figure 4.47. Contour Plots of the Pressure Distribution at $y/s = 0.3$ (Kink Region)

The corresponding LEV plane of the previous subchapter for the case of the RX-3 platform is depicted in the following figures. In the same pattern of the experimental case, two contours have been extracted for each angle of attack, one for the streamwise velocity component and one for the normal velocity component on the vertical axis (z-axis). Both contours are similar to the experimental ones, since there are no notable geometry differences in this specific region. Regarding the streamwise velocity component, its peak appears in the leading-edge vortex core and it is higher than the corresponding value of the experimental geometry by approximately 10%. As for the normal velocity component, two opposite velocity direction regions appear, one on the leading edge, with a positive peak, and one on the inner wing, where it has negative values. With the increasing angle of attack, the vortices become stronger, with the velocity peak values increasing accordingly, until the angle of attack of 16°, when the abovementioned vortex breakdown occurs. In this angle, the vortices break down, losing their power and the velocity peak values decrease, from 1.782 at 14° to 1.348 at 16° for the streamwise velocity component and from 2.208 to 1.2 for the normal velocity component.

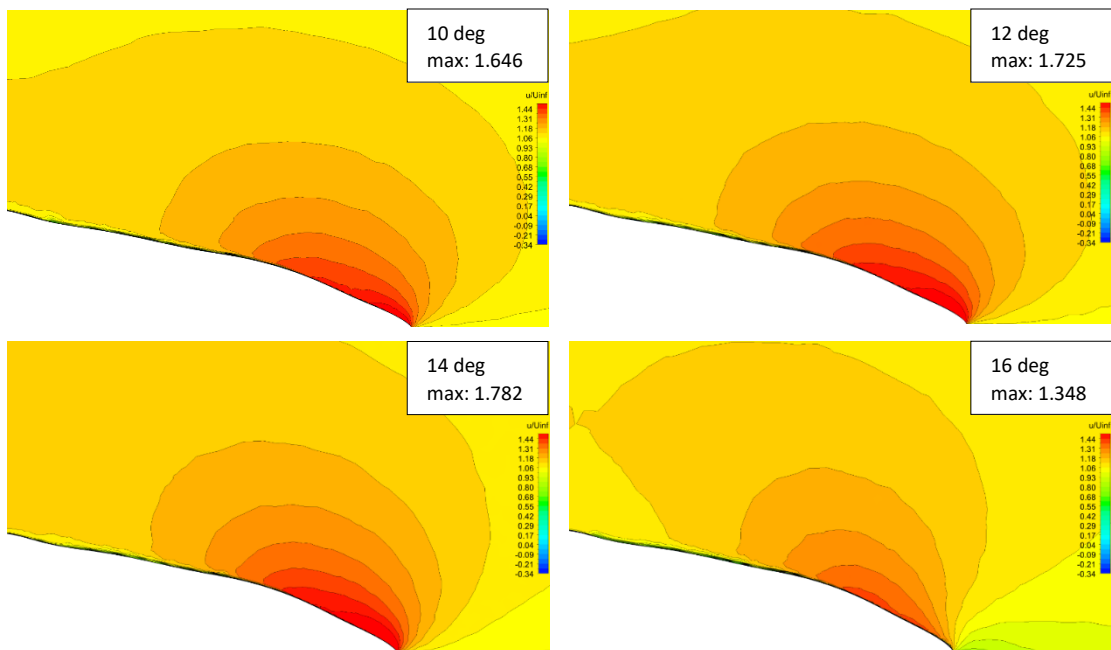


Figure 4.48. Contour Plots of the Streamwise Velocity Component (u/U_{∞}) at $x/C_{\text{root}} = 0.5$

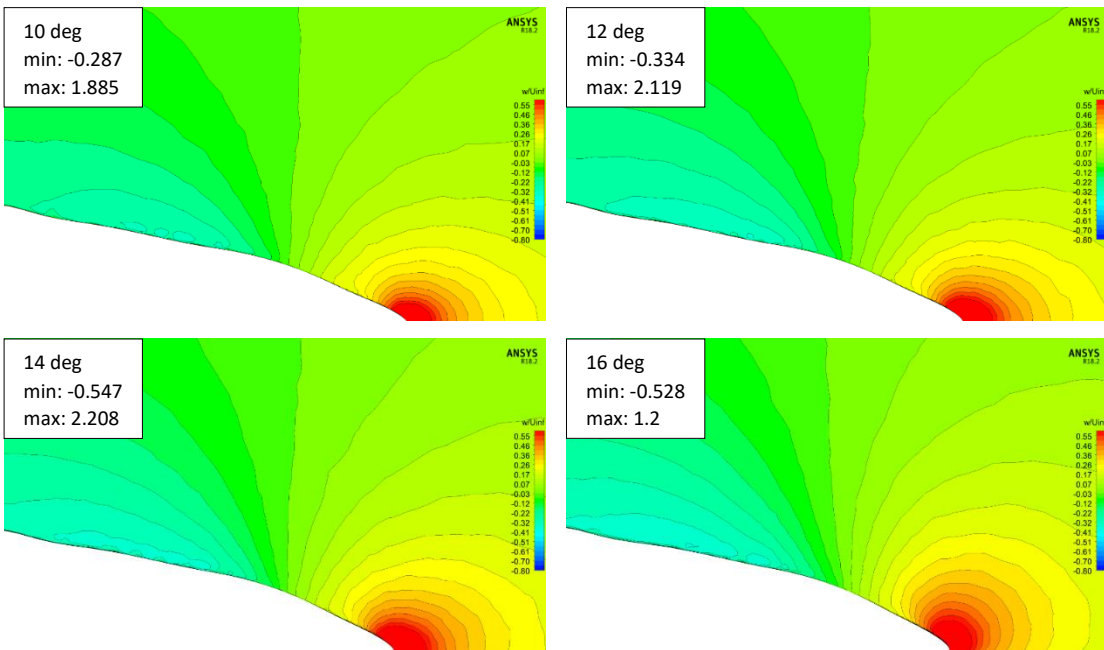


Figure 4.49. Contour Plots of the Normal Velocity Component (w/U_{∞}) at $x/C_{\text{root}} = 0.5$

LEVs in Flight Simulator

The curves presented above, which resulted from the Transition SST turbulence model CFD simulations were finally implemented in the flight simulator in order to test the aircraft's performance once more. The aforementioned curves refer to the take-off phase, when the UAV reaches its highest angle of attack. Thus, this part of the mission was chosen for the simulation. In **Figure 4.50** take-off and climb are shown. The same values with the first case were used for throttle and elevon deflection. The general aircraft behavior is similar to the one presented in the Flight Simulator subchapter, where the Spalart Allmaras model was used, with the main difference being the climb angle of attack which has dropped to approximately 6° and a slight increase in climb velocity. These deviations in trim conditions are due to the different lift, drag and pitching moment values resulted from the new CL, CD and Cm vs α curves. However, the aircraft does not reach angles of attack higher than 10° , where the LEVs appear, and where the differences between the two turbulence models are more important.

As far as the LEVs and the pitch-break phenomena are concerned, an angle of attack higher than 10° is required in order to get an idea of the aircraft's behavior in that regime. Applying a higher elevon deflection during climb, the aircraft's angle of attack surpasses 10° . Following the CL – α and Cm – α curves forms, a sudden increase in pitching moment is expected and then a loss of lift which leads to the aircraft stalling. The simulation of stall is presented in

Figure 4.51. The aircraft takes-off and starts climbing with the same inputs as before, but this time, during climb an increase in elevon deflection leads to the previous discussed series of events, with the final result being the aircraft crushing to the ground.

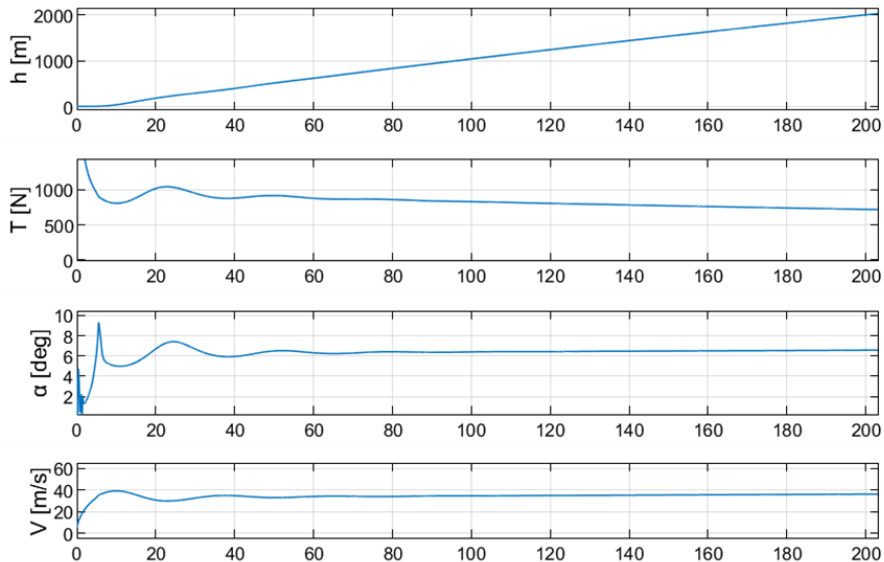


Figure 4.50. Take-off and Climb using the γ -Re θ Curves

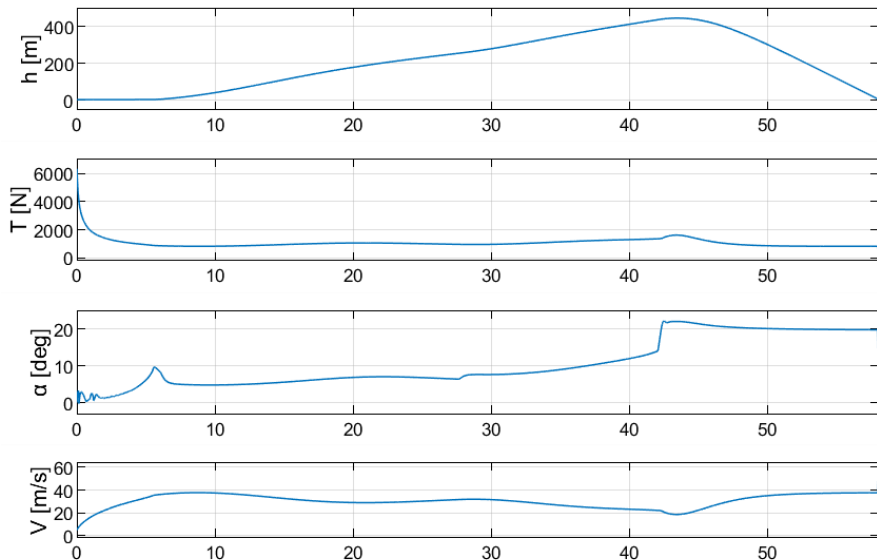


Figure 4.51. Aircraft Stall

CHAPTER 5

CONCLUSIONS

This thesis contributes with its outputs to some key issues, which may come across at the preliminary design phase of a BWB MALE UAV. A variety of tools were created and utilized, in order to get the final results. Regarding the first part of the thesis, a pilot-in-the-loop dynamic simulation model was built, using a combination of MATLAB and Simulink software. The model was also connected to the FlightGear flight simulator in order to get a real-time visualization of the aircraft's performance during its mission. The model includes all the essential subsystems for the simulation of the complete flight envelope, i.e. aerodynamics, propulsion, landing gear, stability and control, flight dynamics and the interaction of the aircraft with the environment, such as wind gusts and turbulence. All these subsystems contribute to the computation of the aircraft's state in every iteration, which results from the solution of the equations of motion and the integration of the state rates, using an appropriate integration algorithm. Simulations were carried out for each phase of the DELAER RX-3's mission. Starting with cruise, which is the main and longer part of the mission, the first step was to validate the model's accuracy, by comparing the control inputs needed for the aircraft to fly in equilibrium and the rest trim conditions, with the corresponding values which resulted from other tools. The matching was very satisfying, meaning that the model is accurate and appropriate for testing the aircraft's behavior in the different parts of the mission. Additionally, the aircraft's longitudinal and lateral stability was tested, by applying small, sharp deflections on the control surfaces. The elevon's deflection as elevator resulted to a convergent phugoid with a 45 s period, with the aircraft finally returning to its trim state. As for the lateral stability, the elevon's deflection as aileron led to a slowly divergent spiral mode, with a roll angle doubling time of 30 s, which was deemed long enough to categorize the phenomenon as acceptable. Regarding the take-off, a number of useful information can be extracted from the simulation, such as the time and runway length needed until the aircraft leaves the ground, and then the trim conditions for a specific climb rate. As for the payload drop phase, the most important test was the effect of the changes the aircraft undergoes, after releasing the payload, on stability, since a relocation of the CG more aft, closer to the AC, occurs. From the simulation, it seems that the aircraft remains longitudinally stable after the drop. The last part of the mission includes descent and landing. Once more, various data for the aircraft's behavior can be extracted, such as the rate of descent for given trim inputs, the appropriate attitude for landing, the time and the distance from the brake application until the aircraft immobilization. A notable detail is that the model takes into account the ground effect when the aircraft approaches the ground. Finally, simulations

including the effect of the wind were conducted, testing the aircraft's response to different direction gusts as well as turbulence, which is important since the mission may include hazardous weather conditions. Recommendation of further upgrades to the simulator include the transformation to a closed-loop model, with the implementation of an autopilot system.

As for the second part of the thesis, a detailed literature review about the LEV phenomenon was presented. Several active and passive techniques to eliminate the resulting nonlinear characteristics were mentioned. Moreover, dedicated CFD simulations, with four different turbulence models, namely the Reynolds Stress Model, the Shear Stress Transport model, the Spalart-Allmaras with Rotation/Curvature Correction model and the Transition Shear Stress Transport model (γ - Re_θ), were conducted over a BWB configuration. This configuration has been investigated experimentally, in a closed-circuit, low-speed wind tunnel facility, at the LFMT. The CFD post-processing showed that the Transition SST (γ - Re_θ) turbulence model predicts the vortical flow with higher accuracy. Hence, this model was used to analyze the leading-edge vortices over the prototype geometry of the DELAER RX-3. Initially, a grid sensitivity study was conducted, in order to determine the optimal mesh density for the CFD analysis, which led to a mesh of approximately 16 million nodes. Finally, the results of the simulations on the RX-3 showed a loss of lift and an increase in pitching moment after the angle of attack of 10°, matching the pitch break theory, and indicating the existence of the Leading-Edge Vortices, which become stronger with increasing angle of attack. Further study of the phenomenon showed that the vortical structure over the aircraft has the biggest effect at the kink region, where the main body blends with the wing, and validated the assumption of the vortex breakdown. At 14° angle of attack the vortical flow separates and then is reattached on the wing, forming separation bubbles. Finally, at 16°, new separation bubbles are formed near the leading edge, with the previous ones moving further back and growing in size. This leads to the vortex breakdown phenomenon, with full separation of the flow at the aft part of the wing, resulting to loss of lift, and consequently wing stalling. The vortex breakdown is also validated by the decrease in the peak values of the streamwise and normal velocity components. Suggestions for future study include further research concerning the wide number of passive and active techniques that a designer can implement to eliminate the drawbacks of the LEV phenomenon and improve the aerodynamic efficiency and performance characteristics of a non-slender BWB configuration.

The synergy of the two parts of this thesis is obvious, since the final step was the utilization of the Flight Simulator, in order to test the performance of the curves which resulted from the Transition SST simulations, and the consequences of the LEVs on the aircraft's stability, during take-off and climb. Slight differences were observed for the normal take-off and climb conditions, where the angle of attack is always lower than 10°. As for the LEVs regime, when a higher elevon deflection was applied during climb, the UAV's angle of attack surpassed 10°, leading to the pitch break phenomenon, with a sudden nose-up moment, a loss of lift, and the finally aircraft stalling and crushing to the ground.

REFERENCES

- [1] DELAER RX-3 [Online]. Available at: <https://lfmt.gr/delaer-rx3/> (Accessed: 1 March 2020).
- [2] HCUAV RX-1 [Online]. Available at: <https://lfmt.gr/hcuav> (Accessed: 1 March 2020).
- [3] Panagiotou, P., Kaparos, P., Salpingidou, C. and Yakinthos, K. "Aerodynamic design of a MALE UAV." *Aerospace Science and Technology* Vol 50 (2016): pp. 127-138.
- [4] Unmanned Aerial Vehicle. *Dictionary of Military and Associated Terms* (2005). Available at: <https://www.thefreedictionary.com/unmanned+aerial+vehicle> (Accessed: 2 March 2020).
- [5] Wallace, A. "State government gears up for autonomous RPAS mapping". *Spatial Source*. January 23, 2017.
- [6] Tice, B. P. "Unmanned Aerial Vehicles – The Force Multiplier of the 1990s." *Airpower Journal* (1991).
- [7] Defense.gov. "Autumn Drone" [Online]. Available at: <https://www.defense.gov/observe/photo-gallery/igphoto/2002195961/> (Accessed: 2 March 2020).
- [8] Vertical Technologies. "DeltaQuad Pro #VIEW VTOL Fixed Wing Surveillance UAV" [Online]. Available at: <https://www.deltaquad.com/vtol-drones/view/> (Accessed: 2 March 2020).
- [9] Franke, U. E. "Civilian Drones: Fixing an Image Problem?" *ISN Blog*. International Relations and Security Network, January 26, 2015.
- [10] Unmanned Aerial Vehicle (UAV) Market by Vertical, Class, System, Industry (Defense & Security, Agriculture, Construction & Mining, Media & Entertainment), Type, Mode of Operation, Range, Point of Sale, MTOW and Region - Global Forecast to 2025 [Online]. Available at: <https://www.marketsandmarkets.com/Market-Reports/unmanned-aerial-vehicles-uav-market-662.html> (Accessed: 1 March 2020).
- [11] Panagiotou, Pericles. "Aerodynamic Efficiency and Performance Enhancement of Fixed-Wing Unmanned Aerial Vehicles using Novel Configurations and Techniques." PhD Thesis. Aristotle University of Thessaloniki, Thessaloniki, Greece. 2018.
- [12] John, Anderson D. *Fundamentals of Aerodynamics*. McGraw-Hill Higher Education, New York (2016).
- [13] Liebeck, R.H. "Design of the Blended Wing Body Subsonic Transport." *Journal of Aircraft* Vol 41 No. 1 (2004): pp. 10–25.
- [14] John, Anderson D. *Aircraft Performance and Design*. WCB/McGraw–Hill, Boston (1999).
- [15] Panagiotou, P., Fotiadis-Karras, S. and Yakinthos, K. "Conceptual design of a Blended Wing Body MALE UAV." *Aerospace Science and Technology* Vol 73 (2018): pp. 32-47.
- [16] Panagiotou, P. and Yakinthos, K. "Parametric aerodynamic study of Blended-Wing-Body platforms at low subsonic speeds for UAV applications."

- [17] Qin, N., Vavalle, A., Le Moigne, A., Laban, M., Hackett, K., and Weinerfelt, P., "Aerodynamic considerations of blended wing body aircraft," *Progress in Aerospace Sciences*, vol. 40, Aug. 2004, pp. 321–343.
- [18] Page, R. L. "Brief History of Flight Simulation." (n.d.).
- [19] Banks, C. "A discussion of methods of real-time airplane flight simulation." The Pennsylvania State University (n.d.).
- [20] Panagiotou, P., Tsormpatzoglou, P., Bliamis, C. and Yakinthos, K. "Experimental investigation of two Blended-Wing-Body models with varying sweep angles at low-subsonic conditions."
- [21] Jo, Y.H., Chang, K., Sheen, D.J. and Park, S. "Numerical simulation of aerodynamic characteristics of a BWB UCAV configuration with transition models." *Int'l J. of Aeronautical & Space Sci.* Vol 16 (2015): pp. 8-18.
- [22] Durham W. *Aircraft Flight Dynamics and Control*. Aerospace Series, Virginia Polytechnic Institute and State University, USA (2013).
- [23] SP-367 Introduction to the Aerodynamics of Flight. [online] Available at: <https://history.nasa.gov/SP-367/f165.htm> (Accessed: 11 March 2020).
- [24] Beard, R. W., McLain, T. W. *Small Unmanned Aircraft: Theory and Practice*. Princeton University Press, USA (2012).
- [25] Nelson, R. C. *Flight stability and automatic control*. McGraw-Hill, New York (1989).
- [26] Difference Between. *Difference Between Static Stability and Dynamic Stability* (2012). [Online]. Available at: <https://www.differencebetween.com/difference-between-static-stability-and-vs-dynamic-stability/> (Accessed: 15 March 2020).
- [27] Tonti, J., Matteis, G. D. and Rizzi A. "Development of a Flight Dynamics Model of a Flying Wing Configuration." *Sapienza Universita Di Roma*, Rome, Italy (2014).
- [28] Baarspul M. "A review of flight simulation techniques." *Progress in Aerospace Sciences* Vol. 27 (1990): pp. 1-120.
- [29] Haitao, W., Xinmin, D., Jianping, X., Jiaolong, L. and Jian, W. "Modeling and simulation of a time-varying inertia aircraft in aerial refueling." *Chinese Journal of Aeronautics* Vol. 29 No. 2 (2016): pp. 335-345.
- [30] Grauer, J. A. and Morelli, E. A. "A Generic Nonlinear Aerodynamic Model for Aircraft." *AIAA Atmospheric Flight Mechanics Conference*. AIAA 2014-0542. National Harbor, MD, United States, January 13-17, 2014.
- [31] Roskam, J., *Airplane Design*. DARcorporation, Lawrence (2004).
- [32] Halloran, M. and O'Meara, S. *Wing in Ground Effect Craft Review*. DSTO Aeronautical and Maritime Research Laboratory, Australia (1999).
- [33] Raymer, D. P., *Aircraft Design: A Conceptual Approach*. American Institute of Aeronautics and Astronautics, Reston, VA (1992).
- [34] Bryc, W. *The Normal Distribution: Characterizations with Applications*. Springer-Verlag (1995).

- [35] Hoblit, F.M. *Gust Loads on Aircraft: Concepts and Applications*. American institute of Aeronautics and Astronautics, Washington, DC (1988).
- [36] Pope, Stephen B. *Turbulent Flows*. Cambridge University Press (2000).
- [37] Kolmogorov, Andrey N. "The Local Structure of Turbulence in Incompressible Viscous Fluids at Very Large Reynolds Numbers." *Proceedings of the Royal Society A — Mathematical, Physical and Engineering Sciences* (1991): pp. 9-13.
- [38] Kolmogorov, Andrey N. "Dissipation of energy in the locally isotropic turbulence." *Proceedings of the Royal Society A — Mathematical, Physical and Engineering Sciences* (1991): pp. 15-17.
- [39] Moukalled, F., Mangan, L. and Darwish, M. *The Finite Volume Method in Computational Fluid Dynamics*. Springer International Publishing, Switzerland (2016).
- [40] Launder, B. E. and Spalding, D. B. "The Numerical Computation of Turbulent Flows." *Computer Methods in Applied Mechanics and Engineering* Vol. 3 (1974): pp. 269-289.
- [41] David, Wilcox C. "Reassessment of the Scale Determining Equation for Advanced Turbulence Models." *AIAA Journal* Vol. 26 No. 11 (1988): pp. 1299-1310.
- [42] Menter, F.R. "Multiscale Model for Turbulent Flows." *24th Fluid Dynamics Conference*. AIAA 93-2906. Orlando, Florida, July 6-9, 1993.
- [43] Menter, F. R. "Two-Equation Eddy-Viscosity Turbulence Models for Engineering Applications." *AIAA Journal* Vol. 32 No. 8 (1994): pp. 1598-1605.
- [44] ANSYS®, Release 18.2, ANSYS Inc., 2017.
- [45] Spalart, P.R. and Allmaras S.R. "A One-Equation Turbulence Model for Aerodynamic Flows". *30th Aerospace Sciences Meeting & Exhibit*. AIAA 92-0439. Reno, Nevada, January 6-9, 1992.
- [46] Spalart, P.R. and Shur M. "On the Sensitization of Turbulence Models to Rotation and Curvature". *Aerospace Science and Technology*. No. 5 (1997): pp. 297–302.
- [47] Shur, Michael L., Strelets, Michael K., Travin, Andrey K. and Spalart P.R. "Turbulence Modeling in Rotating and Curved Channels: Assessing the Spalart-Shur Correction." *AIAA Journal* Vol. 38 No.5 (2000): pp. 784-792.
- [48] Smirnov, Pavel E. and Menter, Florian R. "Sensitization of the SST Turbulence Model to Rotation and Curvature by Applying the Spalart-Shur Correction Term." *Proceedings of ASME Turbo Expo 2008: Power for Land, Sea and Air*. GT2008-50480. Berlin, Germany, June 9-13, 2008.
- [49] Gursul, I., Gordnier, R. and Visbal, M. "Unsteady Aerodynamics of Nonslender Delta Wings." *Progress in Aerospace Sciences*. Vol. 41 (2005): pp. 515-557.
- [50] Schütte, A., Hummel, D. and Hitzel, S.M. "Flow Physics Analyses of a Generic Unmanned Combat Aerial Vehicle Configuration." *Journal of Aircraft* Vol. 49 No. 6 (2012): pp. 1638-1651.
- [51] Zhao, W., Kwak, D. and Rinoie, D. "Studies on Improvement of Nonlinear Pitching Moment Characteristics of Cranked-Arrow Wing." *28th International Congress of the Aeronautical Sciences*. Brisbane, Australia, September 23-28, 2012.

- [52] Carter, M., Vicroy, D. and Patel, D. "Blended-Wing-Body Transonic Aerodynamics: Summary of Ground Tests and Sample Results (Invited)." *47th AIAA Aerospace Sciences Meeting Including The New Horizons Forum and Aerospace Exposition*. Orlando, Florida, January 5-8, 2009.
- [53] Vallespin, D., Ronch, A.D., Badcock K.J. and Boelens, O. "Vortical Flow Prediction/Validation for an Unmanned Combat Air Vehicle Model." *Journal of Aircraft*. Vol. 48 No. 6 (2011): pp. 1948- 1959.
- [54] Cummings, R.M. and Schütte, A. "Integrated Computational/Experimental Approach to Unmanned Combat Air Vehicle Stability and Control Estimation." *Journal of Aircraft*. Vol. 49 No. 6 (2012): pp. 1542-1557.
- [55] Schütte, A., Boelens, O.J., Oehlke, M., Jirásek, A. and Loeser, T. "Prediction of the Flow Around the X-31 Aircraft Using Three Different CFD Methods." *Aerospace Science and Technology*. Vol. 20 (2012): pp. 21-37.
- [56] Agrawal, S., Barnett, R.M. and Robinson, B.A. "Numerical Investigation of Vortex Breakdown on a Delta Wing." *AIAA Journal*. Vol. 30 No. 3 (1992): pp. 584-591.
- [57] Whitford, Ray. "Four Decades of Transonic Fighter Design." *Journal of Aircraft* Vol. 28 No. 12 (1991): pp. 805-811.
- [58] Shim, H. and O Park, S. "Passive Control of Pitch - Break of a BWB UCAV Model Using Vortex Generator." *Journal of Mechanical Science and Technology* Vol. 29 No. 3 (2015): pp. 1103-1109.
- [59] Park, S., Chang, K. and Sheen, D.J. "CFD of Blended Wing Body UCAV with Vortex Generator." *30th Congress of the International Council of the Aeronautical Sciences*. DCC Daejeon, Korea, September 25-30, 2016.
- [60] Shim, H. and O Park, S. "Passive control of pitch-break of a BWB UCAV model using vortex generator." *Journal of Mechanical Science and Technology*. Vol 29 (2015): pp. 1103-1109.
- [61] Verhaagen, N.G. "Effects of Leading-Edge Radius on Aerodynamic Characteristics of 50° Delta Wings." *48th AIAA Aerospace Sciences Meeting Including the New Horizons Forum and Aerospace Exposition*. AIAA 2010-0323. Orlando, Florida, January 4-7, 2010.
- [62] Verhaagen, N.G. "Flow over 50° Delta Wings with Different Leading-Edge Radii." *49th AIAA Aerospace Sciences Meeting Including the New Horizons Forum and Aerospace Exposition*. AIAA 2011-991. Orlando, Florida, 4-7 January, 2011.
- [63] Ghoreyshi, M., Ryszka, K., Cummings, R.M. and Lofthouse, A.J. "Vortical flow prediction of a diamond wing with rounded leading edges." *Aerospace Science and Technology*. Vol 57 (2016): pp. 103-117.
- [64] Schütte Andreas "Numerical investigations of the vortical flow on swept wings with round leading edges." *34th AIAA Applied Aerodynamics Conference*. AIAA 2016-4172. Washington, D.C., June 13-17, 2016.

- [65] Lee G.B., Tai Y.C., Jiang F., Grosjean C., Liu C. and Ho C.M. "Leading-Edge Vortices Control on a Delta Wing by Micromachined Sensors and Actuators." *Journal of American Institute Aeronautics and Astronautics*, (1999).
- [66] Vicroy, Dan D. "Blended-Wing-Body Low-Speed Flight Dynamics: Summary of Ground Tests and Sample Results (Invited)." *47th AIAA Aerospace Sciences Meeting Including the New Horizons Forum and Aerospace Exposition*. AIAA 2009-933. Orlando, Florida, January 5-8, 2009.
- [67] Ghee, T.A. "A deployable serrated flap for Air Vehicle Control of a Representative UCAV Configuration." *1st Flow Control Conference*. AIAA 2002-3276. St. Louis, Missouri, June 24-26, 2002.
- [68] Toyoda, K., Kwak, D., Noguchi, M. and Rinoie, K. "Aerodynamic Interference Caused by the Inboard Leading-Edge Flap on the Outboard Area of the Cranked Arrow Wing." *Procedia Engineering*. Vol. 99 (2015): pp. 1642-1646.
- [69] Gursul I., Wang Z. and Vardaki E. "Review of flow control mechanisms of leading-edge vortices." *Progress in Aerospace Sciences*. Vol. 43 (2007): pp. 246–270.
- [70] MATLAB. 9.4.0.813654 (R2018a). The MathWorks Inc., Natick, Massachusetts (2018).
- [71] FlightGear. Available at: <http://www.flightgear.org>
- [72] Community, B. O. *Blender - a 3D modelling and rendering package*. Stichting Blender Foundation, Amsterdam (2018). Available at: <https://www.blender.org/>

